universität wien

MASTERARBEIT / MASTER'S THESIS

Titel der Masterarbeit / Title of the Master's Thesis

Development of an equipment to measure high temperature elastic properties by resonant ultrasound spectroscopy and feasibility study of ceramics and thermoelectric alloys

verfasst von / submitted by

Alexander Wünschek, BSc

angestrebter akademischer Grad / in partial fulfilment of the requirements for the degree of

Master of Science (MSc)

Wien, 2016 / Vienna 2016

Studienkennzahl lt. Studienblatt / degree programme code as it appears on the student record sheet:	A 066 876
Studienrichtung lt. Studienblatt / degree programme as it appears on the student record sheet:	Masterstudium Physik
Betreut von / Supervisor:	Univ.-Prof. Mag. Dr. Herwig Peterlik

Acknowledgments

I would like to thank my advisor Prof. Herwig Peterlik for his continuous support and patience. His knowledge and guidance assisted me through all stages of my research and gave me valuable insight into scientific work. Besides my advisor, I would like to express my sincere gratitude to Stephan Puchegger, who supported me at all times, especially during the most challenging part of this work, the development of our new measuring device. Stephan gave me the freedom I needed and simultaneously provided essential knowledge and ideas to the project.

I also want to thank the whole scientific group Dynamic of Condensed Matter for their kindness and assistance. It was one of the greatest experiences of my university education to be part of this harmonic group.

Last but not least I want to thank my family with all my heart for everything they have done for me. Without their support and patience this masters thesis would not have been possible. My deepest gratitude goes to my sister Barbara and her husband David. Our long and prospering discussions about physics helped me to stay focused during challenging periods of my studies.

Abstract

Resonant ultrasound spectroscopy (RUS) is a widely used technique in order to determine elastic constants of various materials. Major advantages of this method are the determination of the complete elastic tensor from just one spectrum of measured eigenfrequencies and the performance of experiments at high temperatures. The calculation of the samples eigenfrequencies and a subsequent comparison with measured frequencies provide the possibility to extract elastic constants from the RUS spectrum. Today, due to computers with high computational capacity, various shapes and symmetries of a sample can be evaluated. Since elastic constants are needed for the calculation of the eigenfrequencies, RUS is a powerful method provided that the elastic constants are already known to a certain degree. However, for a material with completely unknown elastic properties, a different method needs to be used in advance. The development of a new measuring device together with a furnace for high temperature measurements was one of the goals of this master thesis. Additionally, the elastic constants, i.e. Young's modulus, shear modulus and Poisson's ratio of various samples were determined as a function of temperature.

Zusammenfassung

Mit resonanter Ultraschallspektroskopie (RUS) werden die elastischen Konstanten verschiedener Materialien ermittelt. Ein wesentlicher Vorteil dieser Methode liegt darin, dass der komplette Elastizitätstensor mit einer einzigen Messung bestimmt werden kann. Grundprinzip der RUS ist die Messung von den Eigenfrequenzen des zu untersuchenden Materials und ein anschließender Vergleich mit den berechneten Eigenfrequenzen. Daraus lassen sich die elastischen Konstanten des Materials bestimmen. Da für die Berechnung der Frequenzen unter anderem elastische Konstanten benötigt werden, eignet sich diese Methode nicht für Proben mit komplett unbekannten elastischen Eigenschaften. Ferner war der hohe Rechenaufwand lange Zeit ein limitierender Faktor für die Anwendbarkeit von RUS. Im Zuge dieser Masterarbeit wurde eine neue Messapparatur für Hochtemperatur RUS entwickelt und gebaut. Mit diesem Messgerät wurde die Temperaturabhängigkeit des Elastizitätsmoduls, des Schubmoduls und der Poissonzahl von verschiedenen Keramiken und thermoelektrischen Legierungen bestimmt.

Contents

1 Resonant Ultrasound Spectroscopy **11**

1.1 History . . . 12
1.2 Theory . . . 13
1.2.1 The elasticity tensor . . . 13
1.2.2 Elastic waves in solids . . . 20
1.2.3 Pulse echo and continuous wave methods . . . 21
1.2.4 Resonant ultrasound spectroscopy . . . 23
1.2.5 Computation . . . 25
1.3 Applications . . . 29

2 Samples **31**

2.1 Ceramics . . . 31
2.1.1 Si_3N_4 . . . 32
2.1.2 Al_2O_3 . . . 33
2.1.3 ZrO_2 . . . 35
2.2 HfNiSn, TiNiSn, ZrNiSn . . . 35
2.3 Vycor 7930 . . . 37

3 Development and construction **39**

3.1 RUS device . . . 40
3.2 Signal transfer to sample . . . 46
3.3 Cooling . . . 47
3.4 Furnace . . . 48
3.4.1 Tuning . . . 53

4 Measurement **57**

4.1 Low temperature . . . 57
4.2 High temperature . . . 59

5 Software **61**
5.1 Elastotron 61
5.1.1 Eurotherm controller 65
5.2 Frequency analysis program 67

6 Results **69**
6.1 Si_3N_4 69
6.2 Al_2O_3 76
6.3 ZrO_2 82
6.4 HfNiSn 89
6.5 TiNiSn 97
6.6 ZrNiSn 105
6.7 Vycor 7930 113
6.8 Discussion 114

7 Conclusion **117**

Appendices **119**

1 Resonant Ultrasound Spectroscopy

1.1 History 12
1.2 Theory 13
1.2.1 The elasticity tensor 13
1.2.2 Elastic waves in solids 20
1.2.3 Pulse echo and continuous wave methods 21
1.2.4 Resonant ultrasound spectroscopy 23
1.2.5 Computation 25
1.3 Applications 29

Elastic properties of materials are one of the most fundamental characteristics of solid matter, along with the atomic structure. While the minimum of the free energy with respect to the atom positions determines the atomic structure, the curvature of the free energy in the vicinity of this minimum determines the elastic constants. This means that elastic constants are derivatives of the free energy and therefore have a strong connection to thermodynamic properties of a certain material. Parameters like specific heat or Debye temperature are just two of many thermodynamic properties which can be linked to elastic constants. Information on relaxation mechanisms, coupling with electrons or anharmonicity can be obtained by the damping of elastic waves in a material. Furthermore, elastic properties are valuable probes of phase transitions, for example super conductivity. This emphasizes the enormous importance of elastic constants. A variety of experimental techniques have been developed over the years to determine elastic constants of different types of material. The applicability of a certain technique depends on

factors such as the composition, structural characteristic and size of the sample as well as required measurement accuracy. The most common techniques can be distinguished by the major parameters that are evaluated. Pulse-echo or continuous wave methods rely on the measurement of speed of sound in a sample in order to determine elastic constants, whereas in resonant ultrasound spectroscopy (RUS) or resonant beam technique (RBT) a measurement of resonant frequencies leads to elastic constants. In general, speed of sound measurements are a convenient tool to determine elastic properties of condensed matter, because as long as the measured variable couples to the wavelength of sound waves a good characterization of the solids elasticity is possible. However, these techniques have a couple of drawbacks, for example a relatively large sample size is needed and multiple independent measurements are required to determine the complete elastic tensor. Especially if the sample has a low symmetry, a large number of measurements in different crystallographic directions is required for a complete analysis. RBT and RUS take a different approach by measuring resonant frequencies, which are determined by elastic constants, dimensions of the sample and specific density. RBT is a widely used technique [3], [4] that is not limited by high temperature environments [5] and can be adapted to anisotropic materials [6]. RUS, compared to time of flight methods, requires a smaller sample size, has a higher accuracy and most essentially the complete set of elastic constants can be obtained by one spectrum of a single measurement, resulting in a less time consuming experimental effort. A crucial part of RUS is the calculation of the samples eigenfrequencies with input parameters such as elastic constants, sample dimensions and mass (this calculation is also known as the forward problem). Afterwards a nonlinear inversion algorithm is applied, in order to determine the elastic constants from the measured eigenfrequencies (more on that in chapter 1.2.5). The computational requirements for this process were a major concern up until the mid 1990s but are no longer an obstacle due to the increasing power of desktop computers. To summarize, RUS is a valuable tool for analyzing elastic properties of condensed matter and offers significant advantages compared to earlier methods.

1.1 History

Investigations on elastic properties started in the 17th century, when Galileo and other Philosophers studied the properties of bended beams [1]. The basic physics were introduced by Hooke in 1660, when he developed his famous theory,

the Hooke's Law. The required mathematics were further developed by Euler, Lagrange, Poisson and others. Over many decades a lot of effort was put into this topic, resulting in a theory summarized by Augustus Love in 1927 [7]. This theory indicated that elastic properties could be obtained by measuring the velocity of sound waves propagating inside a material. Due to the complexity of the necessary calculations, solutions could only be obtained for isotropic, spherical, non crystalline samples. Major advances came from the geophysics community, since the solutions were used for seismic data, in order to obtain more information on natural resources or Earth's inner structure [1]. In the late 1960s the potential sample shapes were expanded, when the solution for a rectangular parallelepiped was found [8]. During the 1980s, Albert Migliori used former developments to adapt and improve the technique [9], which he denoted resonant ultrasound spectroscopy for the first time.

1.2 Theory

In this section, stress, strain and how these quantities are connected to the elasticity tensor will be discussed. Furthermore the propagation of ultrasonic waves in solids and different experimental applications are explained. The advantages of RUS and its computational background will close the chapter.

1.2.1 The elasticity tensor

The literature on which this chapter is based on can be found in [10]. In condensed matter, stress can be characterized as an inner force. To describe how this force acts, the solid is divided into small volume elements with dimensions dx, dy, dz. On an arbitrary surface ΔA acts a force ΔF, which has a normal component and two tangential components (see figure 1.1). The stress linked to the normal component is called normal stress, the stress linked to the tangential components is called shear stress. On each surface of the volume element $dxdydz$ normal and shear forces cause a deformation. If the volume is small enough, forces acting on opposite surfaces are equal, leaving 9 total force components (this is visualized in figure 1.2). This state can be described by the so called stress tensor

$$\sigma = \begin{pmatrix} \sigma_{xx} & \sigma_{xy} & \sigma_{xz} \\ \sigma_{yx} & \sigma_{yy} & \sigma_{yz} \\ \sigma_{zx} & \sigma_{zy} & \sigma_{zz} \end{pmatrix} \tag{1.1}$$

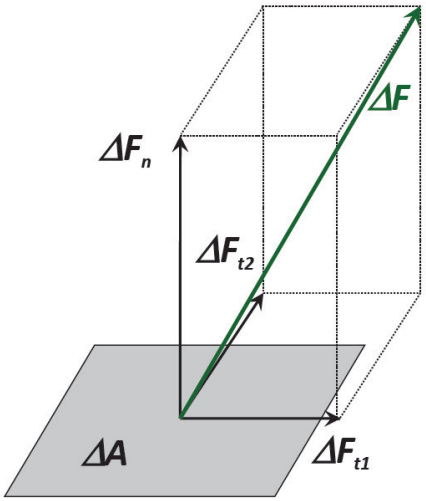


Figure 1.1: Normal and shear forces acting on a surface [10]

whereas the components σ_{xx}, σ_{yy}, σ_{zz} are representing normal stress and σ_{xy}, σ_{yx}, σ_{xz}, σ_{zx}, σ_{yz}, σ_{zy} represent shear stress. This strain tensor is a symmetric tensor of

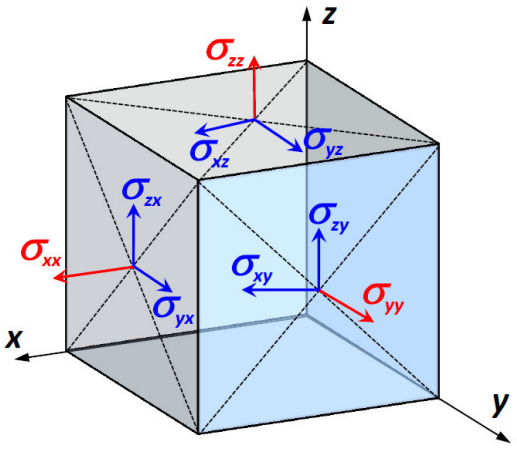


Figure 1.2: Normal Stress (red vectors) and shear stress (blue vectors) acting on a small volume element $dxdydz$ [10]

second order. In the state of equilibrium, neither torque nor translation is acting on the volume element, which leads to the condition that forces acting on opposite surfaces have to be equal with an opposite sign (see figure 1.3) and σ_{ij}=σ_{ji}. These assumptions lead us to 6 independent strain components (3 normal and 3 shear components). The deformations caused by forces are different, depending on where the forces are applied. For example, a force acting on just one side of a cube will result in a different deformation compared to a force which acts on all 6 faces in an

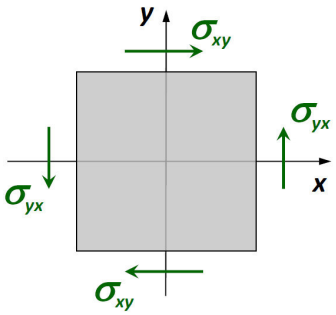


Figure 1.3: To cancel out torque, forces acting on opposite surfaces have to have an opposite sign. The sum of the forces in x direction and y direction is equal to zero [10]

equal amount. The elemental deformations are shown in figure 1.4. After having

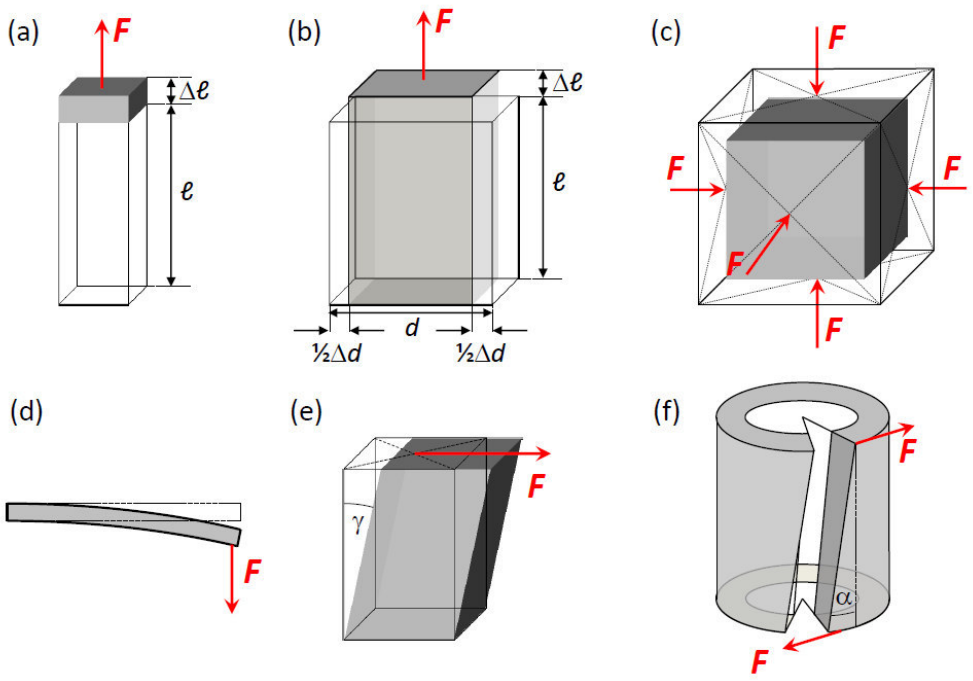


Figure 1.4: Elemental deformations: (a) elongation, (b) transverse deformation, (c) compression, (d) bending, (e) shear, (f) torsion [10]

defined the stress tensor, we will now take a closer look on how to describe strain. In general, a deformation results in a new set of unit vectors. The orthogonal unit vectors $\hat{x}$, $\hat{y}$, $\hat{z}$ become $\hat{x}'$, $\hat{y}'$, $\hat{z}'$ after deformation. As shown in [10], the

corresponding coordinate transformation is

$$\begin{aligned} \hat{x}' &= (1+\epsilon_{xx})\hat{x} + \epsilon_{xy}\hat{y} + \epsilon_{xz}\hat{z} \\ \hat{y}' &= \epsilon_{yx}\hat{x} + (1+\epsilon_{yy})\hat{y} + \epsilon_{yz}\hat{z} \\ \hat{z}' &= \epsilon_{zx}\hat{x} + \epsilon_{zy}\hat{y} + (1+\epsilon_{zz})\hat{z} \end{aligned} \tag{1.2}$$

The dimensionless coefficients ϵ_{ij} are describing the deformation, and since we are withing the range of Hooke's law (small deformations) it is regarded that $\epsilon_{ij} \ll 1$. Due to

$$\hat{x}' \cdot \hat{x}' = 1 + 2\epsilon_{xx} + \epsilon_{xx}^2 + \epsilon_{xy}^2 + \epsilon_{xz}^2 \tag{1.3}$$

the length of the new unit vectors is not equal to 1. Since we can ignore higher orders (because $\epsilon_{ij} \ll 1$) the relative changes of the length of the unit vectors $\hat{x}$, $\hat{y}$, $\hat{z}$ are simply ϵ_{xx}, ϵ_{yy} and ϵ_{zz}. The deformation does not only change coordinates but atom positions as well. Let the position of an arbitrary atom in the solid be described with

$$\vec{r} = x\hat{x} + y\hat{y} + z\hat{z} \tag{1.4}$$

the position after the deformation is

$$\vec{r'} = x\hat{x}' + y\hat{y}' + z\hat{z}' \tag{1.5}$$

This allows us to define a displacement vector to describe the deformation

$$\vec{R} = \vec{r} - \vec{r'} = x(\hat{x}' - \hat{x}) + y(\hat{y}' - \hat{y}) + z(\hat{z}' - \hat{z}) \tag{1.6}$$

Using the coordinate transformations from Equation 1.2 we can rewrite $\vec{R}$ to

$$\vec{R} = (x\epsilon_{xx} + y\epsilon_{yx} + z\epsilon_{zx})\hat{x} + (x\epsilon_{xy} + y\epsilon_{yy} + z\epsilon_{zy})\hat{y} + (x\epsilon_{xz} + y\epsilon_{yz} + z\epsilon_{zz})\hat{z} \tag{1.7}$$

In general, the deformation vector $\vec{R}$ can be written as

$$\vec{R}(\vec{r}) = u(\vec{r})\hat{x} + v(\vec{r})\hat{x} + w(\vec{r})\hat{x} \tag{1.8}$$

Expanding this into a Taylor series around $\vec{r} = 0$ and comparing the terms to Equation 1.7, it can be shown that

$$x\epsilon_{xx} \simeq x\frac{\partial u}{\partial x} \qquad y\epsilon_{yx} \simeq y\frac{\partial u}{\partial y} \qquad z\epsilon_{zx} \simeq z\frac{\partial u}{\partial z} \tag{1.9}$$

Usually, the so called strain coefficients e_{ij} are used instead of the coefficients ϵ_{ij}. The precise way to get from ϵ to e can be found in [10]. For the purpose of this work, it is sufficient to know that ϵ and e are related in the following way

$$e_{xx} \equiv \frac{1}{2}\hat{x}' \cdot \hat{x}' - \frac{1}{2} = \epsilon_{xx} = \frac{\partial u}{\partial x} \tag{1.10}$$

$$e_{yy} \equiv \frac{1}{2}\hat{y}' \cdot \hat{y}' - \frac{1}{2} = \epsilon_{yy} = \frac{\partial v}{\partial y} \tag{1.11}$$

$$e_{zz} \equiv \frac{1}{2}\hat{z}' \cdot \hat{z}' - \frac{1}{2} = \epsilon_{zz} = \frac{\partial w}{\partial z} \tag{1.12}$$

As mentioned before, the strain coefficients which satisfy the condition $i = j$ can be interpreted as the relative change of the unit vectors length. The strain coefficients which satisfy $i \neq j$ are representing the change in the angle between unit vectors. As shown in [10] the strain coefficients are

$$e_{xy} \equiv \frac{1}{2}\hat{x}' \cdot \hat{y}' = \frac{1}{2}(\epsilon_{yx} + \epsilon_{xy}) = \frac{1}{2}\left(\frac{\partial u}{\partial y} + \frac{\partial v}{\partial x}\right) \tag{1.13}$$

$$e_{yz} \equiv \frac{1}{2}\hat{y}' \cdot \hat{z}' = \frac{1}{2}(\epsilon_{zy} + \epsilon_{yz}) = \frac{1}{2}\left(\frac{\partial v}{\partial z} + \frac{\partial w}{\partial y}\right) \tag{1.14}$$

$$e_{zx} \equiv \frac{1}{2}\hat{z}' \cdot \hat{x}' = \frac{1}{2}(\epsilon_{zx} + \epsilon_{xz}) = \frac{1}{2}\left(\frac{\partial u}{\partial z} + \frac{\partial w}{\partial x}\right) \tag{1.15}$$

The e_{ij} are the components of the so called strain tensor

$$e = \begin{pmatrix} e_{xx} & e_{xy} & e_{xz} \\ e_{yx} & e_{yy} & e_{yz} \\ e_{zx} & e_{zy} & e_{zz} \end{pmatrix} \tag{1.16}$$

which is, just like the stress tensor, a symmetric second order tensor. It fully describes the deformation. The strain coefficients are dimensionless and are the partial derivatives of the components u, v, w of the displacement vector $\vec{R}$ with respect to the coordinates x, y, z.

As long as the deformations are small, Hooke's law is applicable (this state is called linear-elastic or Hookean). It puts the aforementioned strain and stress into the following relation:

$$\boxed{\sigma_{ij} = C_{ijkl} e_{kl}} \tag{1.17}$$

The proportionality factor C_{ijkl} is the elasticity tensor, its components the elastic constants. It is a 4th-order-tensor which therefore has 81 independent components and has the dimension of force per surface or energy per volume. Due to the symmetries of strain ($e_{ij} = e_{ji}$) and stress ($\sigma_{ij} = \sigma_{ji}$) it is understandable that $C_{ijkl} = C_{jikl} = C_{ijlk}$ which reduces the number of independent components to 36. Because the elastic energy is a quadratic function of deformation, the number of independent components is further reduced to 21. Any additional decrease of components depends on the samples symmetry. For instance, only the lowest crystallographic symmetry, triclinic, has 21 elastic constants. On the other end of the scale, an isotropic material has only 2 constants. An overview of which crystal system has how many elastic constants is shown in the following table

Crystal system	Point groups	Elastic constants
Triclinic	all	21
Monoclinic	all	13
Orthorhombic	all	9
Tetragonal	C_4, C_{4h}, S_4	7
Tetragonal	C_{4v}, D_{4v}, D_{4h}, D_{2d}	6
Rhombohedral	C_3, S_6	7
Rhombohedral	C_{3v}, D_3, D_{3d}	6
Hexagonal	all	5
Cubic	all	3

Table 1.1: Number of elastic constants for different crystallographic symmetries. The point groups are in Schoenflies notation. For further reading see [10].

For technical applications, a number of important quantities are well established. Since the determination of 3 of those quantities was part of this master thesis, we shall have a brief look on them:

- **Young's modulus E:** correlation between stress and the relative change in length (in direction of the stress).

$$\sigma = E\frac{\Delta l}{l}$$

- **Shear modulus G:** proportionality factor between shear stress and shear

angle γ (see sketch (e) in figure 1.4).

$$\sigma = G\gamma$$

- **Poisson's ratio:** stress does not only alter the length but also the width of a material. The ratio between transverse deformation and the associated change in length is described by ν.

$$\nu = -\frac{\Delta d/d}{\Delta l/l}$$

The Poisson's ratio is also determined by **E** and **G**

$$\nu = \frac{E}{2G} - 1$$

- **Bulk modulus K (or B):** correlation between uniform stress (for example through hydrostatic pressure p) and the corresponding change in volume.

$$p = -\sigma = -B\frac{\Delta V}{V}$$

Lets now discuss how the elasticity tensor looks like. As shown in [10] for a cubic material (which has 3 independent elastic constants) the elasticity tensor can be reduced to

$$\hat{C} = \begin{pmatrix} C_{11} & C_{12} & C_{12} & 0 & 0 & 0 \\ C_{12} & C_{11} & C_{12} & 0 & 0 & 0 \\ C_{12} & C_{12} & C_{11} & 0 & 0 & 0 \\ 0 & 0 & 0 & C_{44} & 0 & 0 \\ 0 & 0 & 0 & 0 & C_{44} & 0 \\ 0 & 0 & 0 & 0 & 0 & C_{44} \end{pmatrix} \tag{1.18}$$

For an isotropic material, the following relation

$$2C_{44} = C_{11} - C_{12} \tag{1.19}$$

reduces the number elastic constants to 2: C_{11} (Young's modulus) and C_{44} (shear modulus). Another way to express elastic constants is through the so called stiffness

matrix. For an isotropic material, it is defined as

$$c_{isotropic} = \begin{pmatrix} (2\mu+\lambda) & \lambda & \lambda & 0 & 0 & 0 \\ \lambda & (2\mu+\lambda) & \lambda & 0 & 0 & 0 \\ \lambda & \lambda & (2\mu+\lambda) & 0 & 0 & 0 \\ 0 & 0 & 0 & \mu & 0 & 0 \\ 0 & 0 & 0 & 0 & \mu & 0 \\ 0 & 0 & 0 & 0 & 0 & \mu \end{pmatrix} \tag{1.20}$$

The quantities λ and μ are called first and second *Lamé constants*. Whereas μ is simply the shear modulus G, λ is defined as

$$\lambda = \frac{\nu E}{(1+\nu)(1-2\nu)} \tag{1.21}$$

1.2.2 Elastic waves in solids

Since the concept of the elasticity tensor is now clear, we should take a closer look on how this quantity can be connected to elastic waves in solids. Let us consider an isotropic material with density ρ and divide it into small volumes $dxdydz$. If a force acts on 2 opposite sides x and $x + \Delta x$ (see figure 1.5) the resulting force can be written as

$$\Delta F_x = (\sigma_{xx}(x+\Delta x) - \sigma_{xx}(x))\Delta y \Delta z = \frac{\partial \sigma_{xx}}{\sigma x}\Delta x \Delta y \Delta z \tag{1.22}$$

The force moves the volume element $dxdydz$ along the x-axis. According to

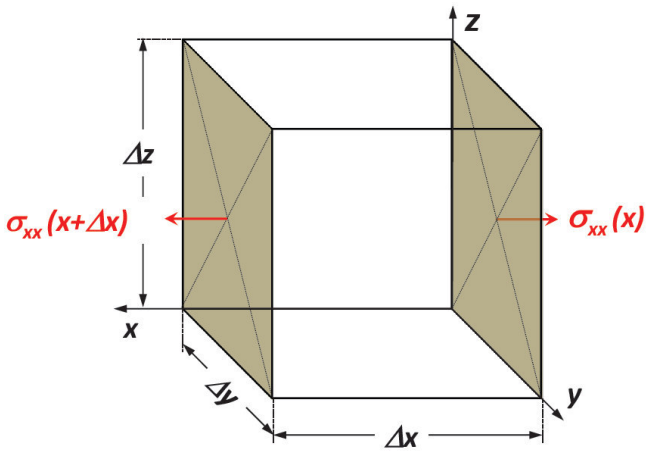


Figure 1.5: A force acting on two opposite faces of the volume element $dxdydz$ [10]

Newton's second law, this acceleration multiplied by mass must be equal to the force. If we write the mass as $\rho \cdot \Delta x \Delta y \Delta z$ we get the following differential equation

$$\rho \frac{\partial^2 u_x}{\partial t^2} = \frac{\partial \sigma_{xx}}{\partial x} \tag{1.23}$$

whereas u_x is the shift along the x-axis. We can now use Hooke's law for the 1-dimensional case

$$\sigma_{xx} = C_{xxxx} e_{xx} = C_{xxxx} \frac{\partial u_x}{\partial x} \tag{1.24}$$

to get the simple wave equation

$$\rho \frac{\partial^2 u_x}{\partial t^2} = C_{xxxx} \frac{\partial^2 u_x}{\partial x^2} \tag{1.25}$$

If our material is not isotropic, we must take all the other stress components into account and how they act on all of the cubes faces. Newton's second law becomes

$$\frac{\partial \sigma_{ij}}{\partial x_j} = \rho \frac{\partial^2 u_i}{\partial t^2} \tag{1.26}$$

Our simple wave equation becomes significantly more complex and leads to a system of coupled differential equations

$$\boxed{C_{ijkl} \frac{\partial^2 u_k}{\partial x_j \partial x_l} = \rho \frac{\partial^2 u_i}{\partial t^2}} \tag{1.27}$$

In general, the solutions of Equation 1.27 are difficult to obtain. A common approach is to assume plane wave solutions and then design the experiments in a way that the simplifying conditions are met. This is the case for pulse echo and continuous wave methods.

1.2.3 Pulse echo and continuous wave methods

With these time of flight methods one can determine elastic constants from velocity and attenuation measurements of a sound wave propagating in a solid [11]. The experimental setup is quite simple [2]: the sample to be studied is placed between two piezoelectric transducers, usually oriented perpendicularly to a major crystallographic axis. An electromagnetic pulse generates ultrasonic vibrations at the transmitting transducer which then travel back and forth across the sample. The echoes excite the receiving transducer as the pulse reverberates in the sample.

After a correction of transducer effects, the wave velocity can be determined from the sample thickness and the time of flight. The decay of the amplitude can be used to determine the attenuation. On the contrary, continuous wave methods

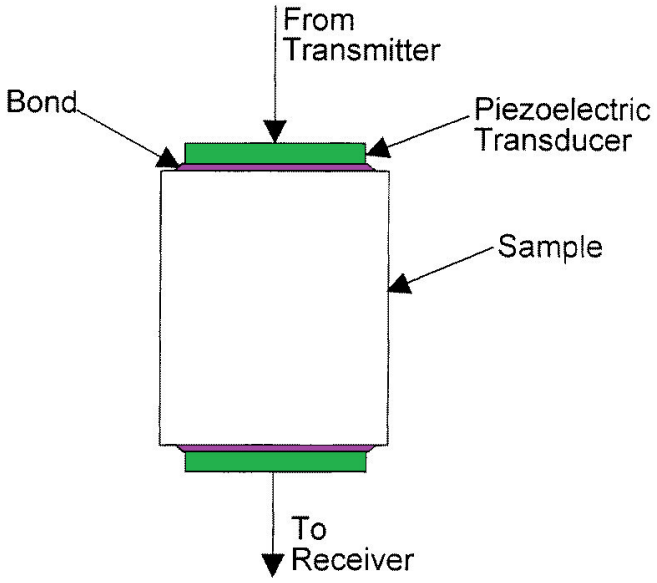


Figure 1.6: General setup for a pulse echo measurement [2]

use a continuous signal outgoing from the transducer and at certain frequencies (which are corresponding to the sample length being a multiple of a half wavelength of sound) a resonant response can be measured, from which wave velocity and attenuation can be determined. The experimental arrangement is similar to the one shown in figure 1.6. These methods can offer a quick and precise way to measure elastic constants. The higher the samples symmetry, the lesser the number of measurements needed. However, there are a couple of drawbacks:

- In order to ensure plane wave propagation, a relatively large sample size is needed. Also, the transducer diameter has to be larger than the ultrasonic wavelength. This means for frequencies around 10 MHz a diameter of 1 cm is required. To avoid reflections on the sides of the sample, the sample must be larger than the transducer.

- Due to diffraction effects, the measurement accuracy of velocity as well as attenuation is limited. Planar waves can only be assumed close to the transducer.

- The bonding agent (which is also required to satisfy the condition of plane waves) between transducer and sample can reduce the detected signal. Non

parallel surfaces caused by the bonding agent can lead to destructive interference.

- To obtain a complete set of elastic constants, the number of independent measurements required can be rather high. For samples with low symmetry, different measurements along different crystallographic axis are needed. For example, orthorhombic symmetry requires nine measurements along six different directions to determine the complete set of elastic constants, which is not only a time consuming task but also a source of errors.

In contrast, resonant ultrasound spectroscopy offers a different approach and has none of the mentioned drawbacks.

1.2.4 Resonant ultrasound spectroscopy

This chapter is based on [2]. Upon excitation, materials show a resonant response at discrete frequencies, the so called normal modes (or eigenmodes). RUS takes advantage of this fact. It therefore does not require plane wave propagation, but relies on the measurement of eigenmodes. Without regard to the assumption of plane waves, a more advantageous experimental setup can be realized: a sample, often a parallelepiped or sphere, is held between two piezoelectric transducers and is excited at one point by one of the transducers. The frequency of this driving transducer passes through a range corresponding to a large number of vibrational eigenmodes of the sample. The resonant response of the sample is detected by the opposite transducer. If the outgoing frequency from the first transducer matches one of the samples eigenfrequencies, a large response can be observed. The eigenfrequenices correspond to the samples elastic constants, shape and orientation. As a result, with a single measurement of a sufficient number of frequencies, one can obtain information on all of these quantities. If shape, density and crystallographic orientation are known, the elastic constants can be calculated from the RUS spectrum. To achieve this at a high accuracy a number of criteria have to be fulfilled, which are discussed in [12] and we shall now take a brief look at the key points of this work. The sample shape for example must be known precisely and no external forces should act on the sample. Furthermore, transducers used to excite and detect the sample eigenfrequencies often have resonant responses as well. This means that the detected signal is a combination of the sample response and the transducer response, which leads to either higher or lower resonant frequencies compared to the true sample eigenfrequencies. By bonding the transducer to a

cylinder of diamond, which has an exceptionally high sound velocity, all resonant frequencies of the transducer-diamond assembly are higher than 4 MHz, which is above most eigenfrequencies of samples with a size $\sim$ 1 mm. As shown in [13], bonding the transducer to ferromagnetic films is an alternative method.

The calculation of eigenfrequencies is a fundamental part of RUS. Since sample shapes used for theoretical calculations are assumed to be geometrically perfect, but even a well prepared sample never is, an error function has to be defined that implies the deviation between real sample and theory. This is a complex task and a simple formula is not available until today but with good sample preparation the accuracy of RUS can be exceptionally high. The theoretical solutions also require traction-free boundary conditions, which is not feasible due to the necessary contact between sample and transducer. To approximate traction-free boundary conditions as good as possible, it is crucial to keep the forces acting on the sample as small as possible, which can be achieved by a vertical sample-transducer arrangement (see section 3.1). To sum up, RUS has a number of advantages compared to the methods described in section 1.2.3:

- **Smaller sample size** is preferred, because sample dimensions of approximately 1 mm result in eigenfrequencies below 4 MHz, which is an appropriate range for measurements. Compared to pulse echo or continuous wave methods, the minimum sample size that is required for RUS is reduced by 1 order of magnitude. This becomes advantageous when measuring novel materials in single crystal form, which are usually not available in larger quantities.
- **Diffraction effects** are a minor concern because there is no plane wave propagation approximated. As a result, the inherent accuracy is very high.
- **No bond** between sample and transducer is required and merely contact force applies, which can be kept at a minimum. This becomes essential when experiments are performed in high temperature environments, which can have negative effects on the bonding agent. For example unwanted strains could apply to the sample by a temperature induced change in the bonding agent, or it could fail to transfer oscillations to the sample.
- **One spectrum** is sufficient to determine all elastic constants of the sample and it is not necessary to measure along multiple crystallographic axes. In terms of experimental effort, low symmetry materials are as convenient to measure as high symmetry materials.

Having so many crucial advantages to conventional methods, the obvious question is why this technique was not used earlier. There is a very complex theoretical background which requires computational power on a high level that was not reached by computers before the mid 1990s. A RUS spectrum contains a large amount of information and the extraction of that information requires the computation of the samples eigenfrequencies and a subsequent comparison of measured and calculated values. Input parameters such as sample shape, mass and elastic constants are used to calculate the frequencies and are changed in an iterative process until a good agreement between calculated and measured frequencies is achieved. Computing eigenfrequencies of a specific sample involves finding the eigenvalues of large matrices, which is less complex if the sample has a high symmetry, but is still a time consuming task. Today, conventional PCs have sufficient computational power to solve such problems in a short amount of time. The mathematical methods have been developed by Holland [14], Demarest [8], Ohno [15] [16], Visscher [17], and Migliori [12]. A brief summary of these efforts will be discussed in the next chapter.

1.2.5 Computation

This chapter summarizes the essential parts of [2]. The direct way to calculate eigenmodes would be to solve Equation 1.27. However, an exact solution is only available for simple, high symmetry materials, and therefore an approximation is required for more complex situations. Solutions of Equation 1.27 (with traction-free boundary conditions), the displacements $u_i(x_k)$, are solutions for which the elastic Lagrangian is an extremum. This convenient fact leads to the general system that is used to calculate eigenvalues. Firstly, the displacements are expanded in a set of basis functions. In the next step, the Lagrangian is derived (with respect to the expansion coefficients) and set to zero. The result is a generalized eigenvalue problem, with kinetic and potential energy represented by large matrices. Conveniently, the eigenvalues give the square of the resonant frequencies, whereas the eigenvectors give the displacements. These results are then used to modify the input parameters. In an iterative process, the eigenvalue/eigenvector calculation is repeated until computed and measured frequencies match. As explained before, the starting point for the calculation is the 3D elastic body Lagrangian

$$L = \frac{1}{2}\int_V (\rho\omega^2 u_i(r)u_i(r) - C_{iji'j'}\partial_j u_i(r)\partial_{j'}u_{i'}(r))dV \tag{1.28}$$

with an $e^{i\omega t}$ time dependence. The subscripts are summed over $i, j, i', j' = 1, 2, 3$. The displacements in Equation 1.28 are now expanded in a basis

$$u_i(r) = a_{i\alpha}\Phi_\alpha(r) \tag{1.29}$$

where $a_{i\alpha}$ are the expansion coefficients and $\Phi_\alpha(r)$ are the basis functions. The $\Phi_\alpha(r)$ are chosen according to the samples shape. For a large variety of shapes, an expansion in powers (in form of x^l, y^m, z^n where l, m, n are integers) is used. For parallelepipeds on the other hand, Legendre polynomials seem to be a good choice for $\Phi_\alpha(r)$. The displacement $u(\mathbf{r})$ has 3 Cartesian components, all of which are expanded according to Equation 1.29. Using this expansion for the Lagrangian, the result is

$$L = \frac{1}{2}\Big(a_{i\alpha}a_{i'\alpha'}\rho\omega^2 \int_V \delta_{ii'}\Phi_\alpha(r)\Phi_{\alpha'}(r)dV - a_{i\alpha}a_{i'\alpha'} \int_V C_{iji'j'}\Phi_{\alpha,j}(r)\Phi_{\alpha',j'}(r)dV\Big). \tag{1.30}$$

If you take the integrals as elements of matrices $\mathbf{E}$ and $\mathbf{\Gamma}$, and the expansion coefficients as vectors $a_{i\alpha}$, the equation can be written as

$$L = \frac{1}{2}((\rho\omega^2)a^T\mathbf{E}a - a^T\mathbf{\Gamma}a) \tag{1.31}$$

To satisfy the condition of L being an extremum, all derivatives of L, with respect to all expansion coefficients, must be set to zero. This leads to a generalized eigenvalue problem

$$\mathbf{\Gamma}a = (\rho\omega^2)\mathbf{E}a. \tag{1.32}$$

In this eigenvalue problem, $\rho\omega^2$ are the eigenvalues λ, and the eigenvectors a are the expansion coefficients. This means, to get the resonant frequencies, one has to calculate the matrices $\mathbf{E}$ and $\mathbf{\Gamma}$, and then find the corresponding eigenvalues. Depending on which expansion type is used (Legendre polynomials for a sample shaped like a parallelepiped with faces perpendicular to x,y,z directions, or a power series for spheres and cylinders) there are standard FORTRAN routines to calculate these matrices. However, the problem with this calculation is, that the matrices usually reach the size of 858×858. Which makes the calculation time consuming. After calculating such a matrix, one will recognize the fact that a lot of matrix elements are equal to zero. The question is now if we can use this fact to our advantage. As shown in [14], [8] the matrix can be factorized in smaller matrices, if the matrix and the sample have mutual symmetries. We will now take a brief

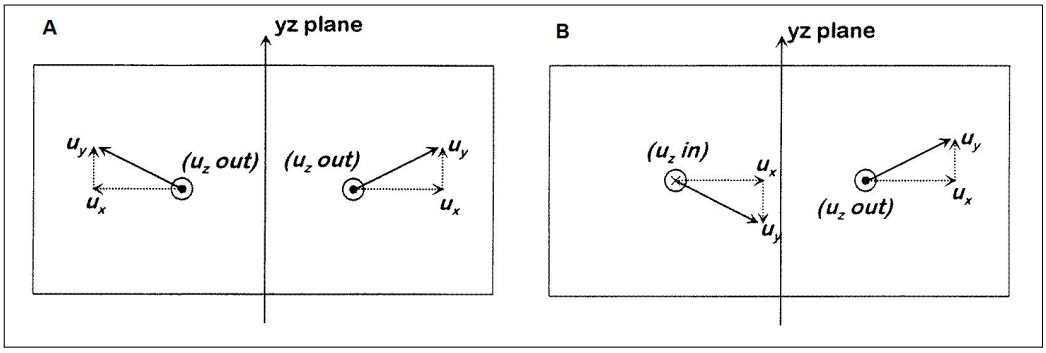


Figure 1.7: Symmetric (A) and anti symmetric (B) displacement function for a yz mirror plane [2]

look on the work from Ohno [15] to see how the matrices can be split. Since the time to solve the problem is proportional to the size of the matrix, it is much faster to solve a couple of smaller matrices than a single large one. We take an arbitrary symmetry element, a yz mirror plane (see figure 1.7). The displacement $u(r)$ can now be divided into a symmetric and antisymmetric part. For the symmetric function, the reflection will change the sign of the x component of the displacement, u_x . The components u_y and u_z will remain the same. The antisymmetric function has an opposite effect. Which means that the u_x component will not change it's sign, but the u_y and u_z component do. The Lagrangian, being the kinetic and the potential energy, must not change under such a transformation. In other words, the symmetric modes u_x have odd parity in x, u_y and u_z are even in x. The anti symmetric modes u_x have even parity in x, u_y and u_z are odd with respect to x. We can now rewrite the displacement

$$u(r) = u^s(r) + u^a(r) \tag{1.33}$$

This new notation seems to be just some additional work, but it has a dramatic effect on the elastic constants matrix because the order of elements is now changed. This means, that the zeros are no longer randomly distributed over the whole matrix. The matrix is now factorized into 4 blocks due to the fact that symmetric terms of the expansion of $u(r)$ are only coupling with other symmetric terms. The same stands for the antisymmetric terms. All elements representing a symmetric-antisymmetric couping are equal to zero. In the end, the matrix has 4 blocks: the left upper quarter (representing symmetric terms), the right bottom quarter (representing antisymmetric terms) and the remaining two quarters, all zeros. The computation time is now greatly reduced, with the help of just one mirror plane.

Further symmetry elements have similar effects. For a second mirror plane (xz) each part of the previous split can be factored again. This results in

$$u(r) = u^{ss}(r) + u^{sa}(r) + u^{as}(r) + u^{aa}(r) \tag{1.34}$$

The first superscript now refers to the parity with respect to the first symmetry operation. The second superscript represents the parity with respect to the second symmetry operation. The matrix is now factorized into 16 blocks, all of them zero, except the 4 blocks along the matrix diagonal. Three mirror planes, perpendicular to the x,y,z axes, will result in a matrix with 64 blocks, 8 of them non-zero, along the diagonal. Mirror planes are especially useful for making the problem less complicated, because only one coordinate changes. The parities of the x,y,z coordinates with respect to the three mentioned mirror planes are shown in figure 1.8. Other symmetry operation can also help, but it is more difficult to exploit. If a power series $(x^\lambda, y^\mu, z^\nu)$ is used for the expansion functions (instead

	Symmetric			Antisymmetric		
	yz	xz	xy	yz	xz	xy
u_x	odd	even	even	even	odd	odd
u_y	even	odd	even	odd	even	odd
u_z	even	even	odd	odd	odd	even

Figure 1.8: Parity of the x,y,z coordinate of the displacement function, with respect to 3 mirror planes perpendicular to x, y, z [2]

of Legendre polynomials) the matrix can be factorized in the same way. The important criteria is the parity of the basis functions with respect to the symmetry operations. Which means that in this regard, the choice of basis functions make no difference whatsoever. To show the time saving potential, the computation time for calculating the eigenvalues of a rectangular parallelepiped with hexagonal symmetry is shown in figure 1.9. According to [2], the computer which was used to achieve these times was a Hewlett–Packard 735 workstation. A machine which was first introduced by HP in 1992. It goes without saying that a modern, state of the art desktop computer will achieve much faster times. But as an example, it is sufficient to use these times. It is shown, that just one mirror planes already reduces the computation time by 60%. If all 3 mirror planes come into play, the

No of mirror planes	No of matrices	Computation time (min:s)
0	1	11:10
1	2	4:27
2	4	1:53
3	8	0:35

Figure 1.9: Computational times for the eigenvalue problem for a hexagonal crystal, using an increasing number of mirror planes [2]

times drop to one-twentieth of the original time. One last marginal note: depending on the basis functions, it might be necessary to factorize the matrix $\mathbf{E}$ as well. The above mentioned techniques to factorize $\mathbf{\Gamma}$ also apply to $\mathbf{E}$.

Calculating the resonant frequencies (as discussed above) is only one part of the computation process in RUS. The second part is to determine sample parameters from the measured frequencies, such as elastic constants, sample dimensions or orientation. The so called inverse problem deals with this subject. The procedure is to calculate certain sample parameters from the measured frequencies, in order to improve the calculation of the frequencies. To measure how well the calculated and measured frequencies match, a function like this is used

$$\chi = \sum_n w_n \frac{(f_n - g_n)^2}{g_n^2} \tag{1.35}$$

where f_n are the calculated frequencies, g_n the measured frequencies and w_n is a weighting factor. The function χ shows a minimum, if the calculated and measured frequencies are closest. These 'correct' frequencies can then be extracted from χ and are used for calculating a new set of elastic constants, or other sample parameters. With this new set the resonant frequencies are calculated again, using the aforementioned techniques. By repeating this procedure in an iterative process, the error becomes smaller and the fit between calculation and measurement improves.

1.3 Applications

In recent years, thin film materials have been the subject of intensive studies. RUS measurements have been extended in order to analyze samples such as thin films on

a substrate. Noteworthy are for instance the works of Gladden [18] and Pestka et al. [19]. Knowledge of mechanical properties at high temperatures are of fundamental importance for materials which are used in such extreme environments. There are many examples for RUS being a reliable method even at high temperatures, see ref. [20], [21], [22]. Geophysically important minerals were the subject of RUS experiments, in order to study the thermal equation of state, the structure, and the composition in the Earth's interior. The temperature variation of elastic constants of such a mineral, single-crystal forsterite (Mg_2SiO_4) was measured up to 400 °C by Sumino et al. [23] and up to 927 °C by Suzuki et al. [24]. The setup where sample and transducer are in direct contact, limits the upper operating temperature. A buffer-rod RUS setup (similar to the setup for this masters thesis) was used to measure elastic constants of single crystals up to 1552 °C [25]. Furthermore, elastic constants are a sensitive probe for changes in the atomic environment, due to fact that they are a measure of the curvature of the bonding energy near its minimum. Subtle changes, such as various temperature induced phase transitions, can be observed in RUS measurements due to its high precision, as shown in [26] and [27].

2 Samples

2.1 Ceramics 31
2.1.1 Si_3N_4 32
2.1.2 Al_2O_3 33
2.1.3 ZrO_2 35
2.2 HfNiSn, TiNiSn, ZrNiSn 35
2.3 Vycor 7930 37

2.1 Ceramics

Ceramics are non-metallic inorganic materials which are electric insulators and, at room temperature, have a thermal conductivity much lower than metals. There are some exceptions, for example diamond, which has a high thermal conductivity because the phonon part of thermal conductivity surpasses the electron part, but in general metals are superior heat conductors. The atomic structure can be crystalline or amorphous, depending on the manufacturing process. Physical and chemical properties are mainly attributable to the covalent and ionic bond type. Typically, ceramics have a high chemical resistance, melting temperature and compressive strength, which gives them a wide range of technical applications. They are usually brittle at low temperatures and show only small inelastic deformation even near to the melting temperature. There are single atom ceramics (for example diamond or graphite) but also oxides and non-oxides. The majority are combinations of metals (or semi conductors) and non-metals, mostly oxides, but also borides, nitrides or carbides (this is visualized in figure 2.1). Single atom ceramics are predominantly made of the 4 valence electron elements carbon, silicon and germanium. In the family of non-oxide ceramics, Si_3N_4 has a special significance due to its low linear

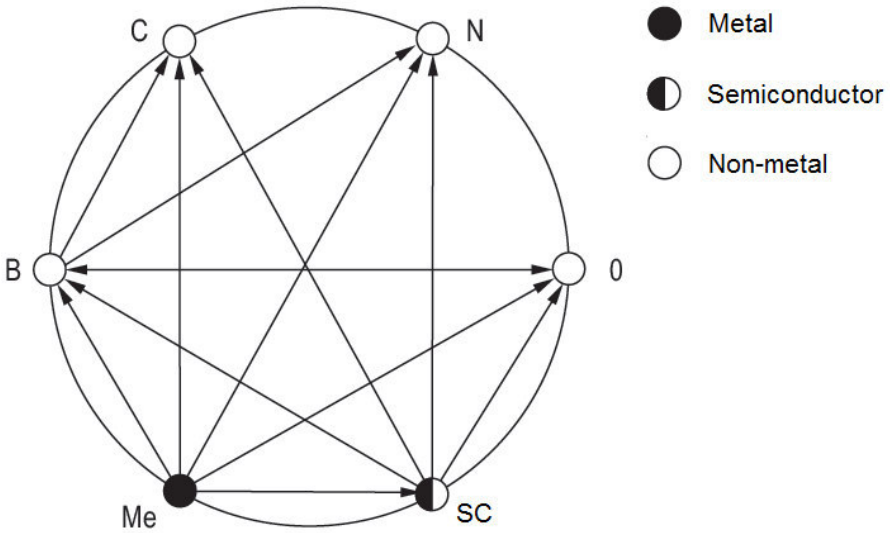


Figure 2.1: Possible combinations of metals, semiconductors and non-metals in order to manufacture ceramic materials [35].

thermal expansion coefficient, high strength and applicability up to 1400 °C. This makes it suitable for extreme environmental conditions, where the material is exposed to high temperature and high mechanical stress. We shall now take a brief look on the different types of ceramics that were analyzed for this masters thesis.

2.1.1 Si_3N_4

Structure: This chapter summarizes the essential parts of [28]. X-ray diffractometry of silicon nitride during the 1950s (see [29]) showed that there are two crystal modifications, trigonal α and hexagonal β, where the c-axis dimension of the unit cell of the α phase is approximately twice that of the β phase. A third phase with cubic spinel structure can be synthesized at temperatures above 2000 K and at pressures above 15 GPa [30]. The α and β structures can vary in bond length, depending on the manufacturing process. Si_3N_4 does not melt but dissociates into silicon and nitrogen at 1880 °C.

Production: There are three forms of Si_3N_4: reaction bonded, dense and amorphous. Reaction bonded silicon nitride (RBSN) was developed in the 1950s, by nitridation of silicon powder at 1300-1400 °C, it is porous (25%-35%) and has a strength of 200-300 MPa. Reproducibility of product quality is difficult to ensure, because factors such as temperature, time, impurities in the silicon powder and

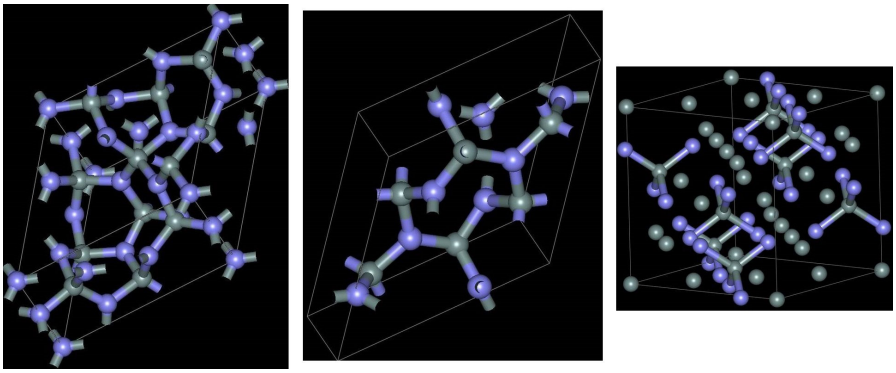


Figure 2.2: Different crystallographic structures of Si_3N_4: trigonal α (left), hexagonal β (center), cubic γ (right). Blue atoms represent nitrogen, gray atoms represent silicon [31].

contamination of the gaseous atmosphere have a significant influence on the micro structure, the pore fraction and the α:β ratio of the final product. Producing dense Si_3N_4 requires additives because hot pressing Si_3N_4 powder simply leads to a porous material with properties similar to RBSN. Additives such as BeO, Mg_3N_2, Al_2O_3 and MgO turned out to be most effective, resulting in densification of Si_3N_4 powder at pressures above 23 MPa and 1850 °C. Materials with a room-temperature strength of 600 MPa and good creep resistance were produced that way. Amorphous Si_3N_4 is commonly produced via CVD at either atmospheric pressure or between 10^{-4} and 10^{-2} bar. Among the most important properties are low permeability towards water, oxygen and sodium (due to the rigid covalent structure), high electrical resistance ($10^{12}\Omega$m) and good chemical resistance.

Applications: The main driving force for the development of Si_3N_4 ceramics during the 1960s were ceramic gas turbines and reciprocating engines running at temperatures too high for metallic parts. The automobile industry was therefore a main contender for Si_3N_4 research and development. High strength, creep, thermal shock and oxidation resistance are the main advantages of ceramic parts until today. Other applications include bearings (due to low friction, high stiffness and low density) and cutting tools for metal working. Amorphous Si_3N_4 is widely used as passivation layer or barrier to alkali or moisture diffusion.

2.1.2 Al_2O_3

Structure: The natural form of Al_2O_3, corundum, is the crystalline polymorphic α phase. It has trigonal symmetry, whereas the oxygen atoms form a distorted

hexagonal closed-packed structure with aluminum atoms filling two thirds of the octahedral interstices.

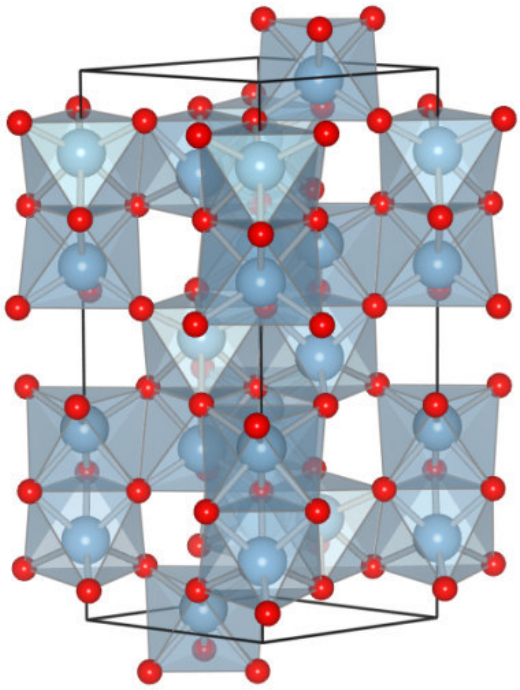


Figure 2.3: Crystal structure of corundum. Red atoms represent oxygen, blue atoms represent aluminum [32].

Production: The Bayer process is the industrial principal on which Al_2O_3 is produced. Base material is aluminum ore, bauxite, which is a mixture of aluminum hydroxides $Al(OH)_3$, γ-AlO(OH), α-AlO(OH) and other components such as silica and iron oxides. $Al(OH)_3$ is extracted from the bauxite using sodium hydroxide, and subsequently calcined to Al_2O_3.

Applications: Due to its hardness (15-19 GPa), compressive strength (2000-4000 MPa) and melting temperature of 2072 °C Al_2O_3 is used as refractory material and abrasive. It is a less expensive alternative to industrial diamond. Al_2O_3 is also an additive for paint, a filler for sunscreens and an ingredient of many different glasses.

2.1.3 ZrO_2

Structure: There are 3 different stable phases of ZrO_2 depending on temperature: monoclinic (T<1170 °C), tetragonal (1170-2370 °C) and cubic (T>2370 °C).

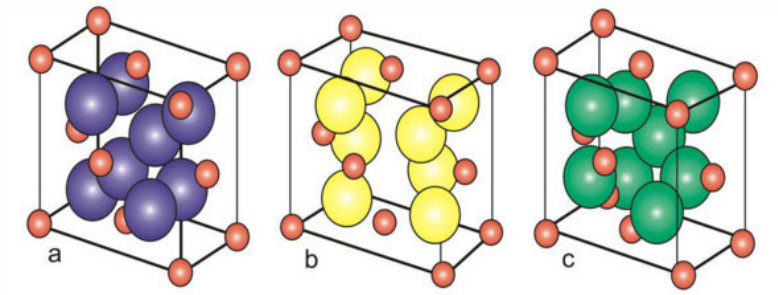


Figure 2.4: ZrO_2 structures. Monoclinic (a), tetragonal (b) and cubic (c). Red atoms represent oxygen [33].

Production: The base material for producing high purity ZrO_2 is $ZrSiO_4$. There are different procedures to extract ZrO_2 powder, including thermal decomposition, precipitation, hydrothermal treatments or melting and rapid quenching. Purity, particle size and size distribution, shape and degree of agglomeration can be controlled by using different manufacturing processes, depending on the specific requirements for the ceramic material [33].

Applications: ZrO_2 is predominantly used for the production of ceramics with a wide range of utilization, including refractory material, insulation parts, abrasives and enamels. Some thermal barrier coatings are made of ZrO_2 due to its low thermal conductivity (cubic phase: 1.7 $Wm^{-1}K^{-1}$). When cooling from high temperatures, the cubic to tetragonal to monoclinic phase transformations induce large stresses, causing the material to crack. The high temperature phases can be stabilized by doping with MgO or Y_2O_3. Single crystals of ZrO_2 are used as a diamond simulant in jewelery.

2.2 HfNiSn, TiNiSn, ZrNiSn

Thermoelectric materials are characterized by showing a strong thermoelectric effect, which is either the conversion of a temperature difference to an electric potential (Seebeck effect) or vice versa (Peltier effect). Due to increasing demand for energy conversion between heat and electricity, thermoelectric materials attracted attention

over the last decade. Some intermetallic compounds, which are called Half-Heusler alloys, show semi conducting behavior and also a large Seebeck coefficient (which is a measure of the magnitude of the induced thermoelectric voltage in response to a temperature difference across the material), which makes them a prime candidate e.g. for energy recovery in cars.

Structure: Heusler alloys can be described by the formula X_2YZ, whereas a Half-Heusler alloy by XYZ. The components X,Y and Z can be selected from different elemental groups: X=Ti, Zr, Hf, V, Mn, Nb; Y=Fe, Co, Ni, Pt; Z=Sn, Sb [34]. The crystal structure is C1b, which is a L21 structure, but one fcc sub lattice remains unoccupied, see figure 2.5).

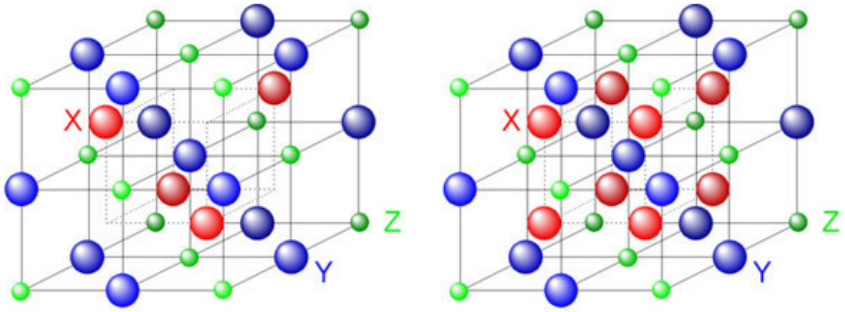


Figure 2.5: Left: Half-Heusler alloy. Right: (full) Heusler alloy.

Production: The Half-Heusler alloy samples studied during this masters thesis were produced by arc melting of stoichiometric amounts of the alloy's components in argon atmosphere. A detailed description of the sample preparation process can be found in ref. [44].

Applications: Thermoelectric Half-Heusler alloys are used as an energy recovery system for waste heat in internal combustion engines. Converting heat loss into usable electric energy is also a practical way to improve the efficiency of generators. This has a high applicability, due to the fact that the majority of electricity is generated by heat energy. Another important application is Peltier-cooling, which, in comparison to vapor-compression refrigeration systems, does not require a refrigerant.

2.3 Vycor 7930

Structure: Vycor 7930 is composed of 96% SiO_2, 3% B_2O_3 and 1% Na_2O, ZrO_2/Al_2O_3 [57]. It is an open-cell porous glass with a porosity of approximately 0.3 and a large internal surface area of 150-250 m^2g^{-1}. The pore distribution is narrow and the pores radius can vary between 10 and 300 Å [47]. The structure has long wave length characteristics similar to a spinodally decomposed binary system with micron-sized inhomogeneities [48].

Production: Alkali-borosilicate glass is melted, quenched and subsequently annealed at a certain temperature, depended on the materials requirements. During annealing, spinodal decomposition occurs and leads to an acid soluble B_2O_3 phase and an acid insoluble SiO_2 phase. The B_2O_3 phase is then leached out by dilute acid solutions. In the final step, the leached Vycor is washed and dried [48].

Applications: Due to its selective permeability, Vycor glass is often used for filtration or separation of specific compounds, for example in high-performance liquid chromatography but it is also applicable for gas chromatography due to the large variety in porous size. There are potential applications in any sealed device that requires exclusion of foreign contaminants, for example transistors or micro relays [57].

3 Development and construction

3.1 RUS device 40
3.2 Signal transfer to sample 46
3.3 Cooling 47
3.4 Furnace 48
3.4.1 Tuning 53

All technical drawings can be found in the appendix.

One of the main goals of this master thesis was to develop a RUS device which features a vertical sample/piezoelectric transducer (in the following referred as piezos) arrangement and to construct a suitable furnace for high temperature measurements up to 900 °C (see figure 3.1). The new arrangement was a refinement of the former, horizontal sample-piezo setup which had a significant drawback when high temperature measurements were performed. Thermal expansions led to an increase in sample size, and during the subsequent cool down phase, when the sample size decreased, the contact between sample and buffer-rods became loose and the sample occasionally dropped down onto the heater. To prevent this from happening, a vertical sample mounting in which the furnace was located above the sample and lowered onto it was the chosen solution (further details on the furnace will be discussed later in this chapter). In order to avoid damage to the piezoelectric transducers, they had to be located outside of the furnace. As a consequence, the sample could not be put directly between the piezos but had to be placed between two long, thin alumina buffer rods (one was straight, one was bent in the shape of a crook), which separated the transducers attached at the other ends of the buffer rods from the harsh high-temperature environment. It was necessary for the buffer-rods to have sufficient contact to the sample to ensure a strong signal

transfer and on the other hand a weak enough contact to not interfere with the traction free boundary condition. The contact force of the upper buffer rod was fine adjusted using a beam balance: two linear guides (figure 3.4) were bought and arranged vertically. The piezo with the bent buffer rod attached to it was mounted to the carriage of one of the linear guides and the carriage of the second linear guide held a counter weight. The two opposing carriages were connected to each other with a thin nylon cord. This arrangement guaranteed a smooth adjustment of the load acting on the sample. To summarize, the new RUS device had to fulfill a number of criteria:

- Vertical fixation of the sample by two alumina buffer-rods with enough contact force acting on the sample to transfer a signal and simultaneously approximate traction free boundary conditions.
- Horizontal and vertical variability of both piezoelectric transducers to ensure a wide range of sample sizes and geometries.
- Vibrational and thermal isolation of both transducers.
- To be able to operate inside a vacuum chamber, the maximum hight of the complete arrangement was limited to 40 cm.

On the basis of these requirements, Solid Works was used as a software to design the necessary parts. Almost all parts were made of aluminum, only the parts shown in appendix figures A4 and A7 were made of plastic.

3.1 RUS device

In the following description, the capital letters A to H refer to the parts in figure 3.2.

A

The base for the whole arrangement was a 120 x 60 mm plate (appendix figure A1)

B

To plate A, the u-shaped part B (appendix figure A2) was mounted (using 2 M4 screws on the bottom of B). This was a guidance for the piezo mounting parts C and D. The mountings were fixed with a M5 screw. A horizontal distance between

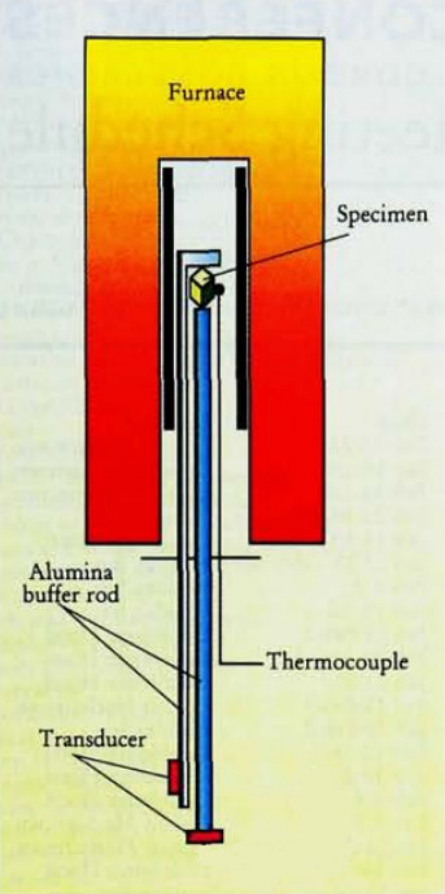


Figure 3.1: Schematic visualization of the planned RUS unit [1]

the mountings up to 5 cm was guaranteed. This was sufficient for a large variety of sample sizes.

C

This part (appendix figure A3) was used to hold the mounting part for piezo number 1 (E) in place, made it move only vertically and held the temperature sensor in place. With a M5 screw, the whole part was mounted onto B. On the front side, a small plate with a slot for the temperature sensor was mounted to C.

D

On all 4 sides of D (appendix figure A5) a different part was mounted. The front side was connected to B, the back side was connected to H. On the left and right side, the two linear guides (bought from NSK Ltd., item number PU09TR, see figure 3.4) were mounted vertically.

E

E was inserted to the vertical slot in part C. The protrusion on the back side of the part fitted precisely into the long slot on C and therefore prevented left/right rotation of E. Also on the back side was a M4 screw hole, to fix the position of E vertically. On the front side, a 10 mm cylindrical slot held one of the piezoelectric transducers in place.

F

The second piezo was held by F (appendix figure A6) and fastened by a M4 bolt. The part was mounted to the carriage of the NSK linear guide. With the linear guide mounted on D, the vertical movement of F was established.

G

The piezo mounted to F needed a counter weight in order to guarantee a soft sample fixation. This counter weight, part G, was bolted to the second NSK linear guide, on the opposite side of D.

H

The mounting part F (which were holding one piezo) and the counter weight had to be connected to each other. The connection was accomplished by a nylon cord. The cord ran over two bearings (Hepco Motion standard bearing, type SJ13, see figure 3.5), to enable a stable connection. These bearings were bolted to H. And H was bolted to D.

The 3D Solid Works file of the complete arrangement is shown in figure 3.3.

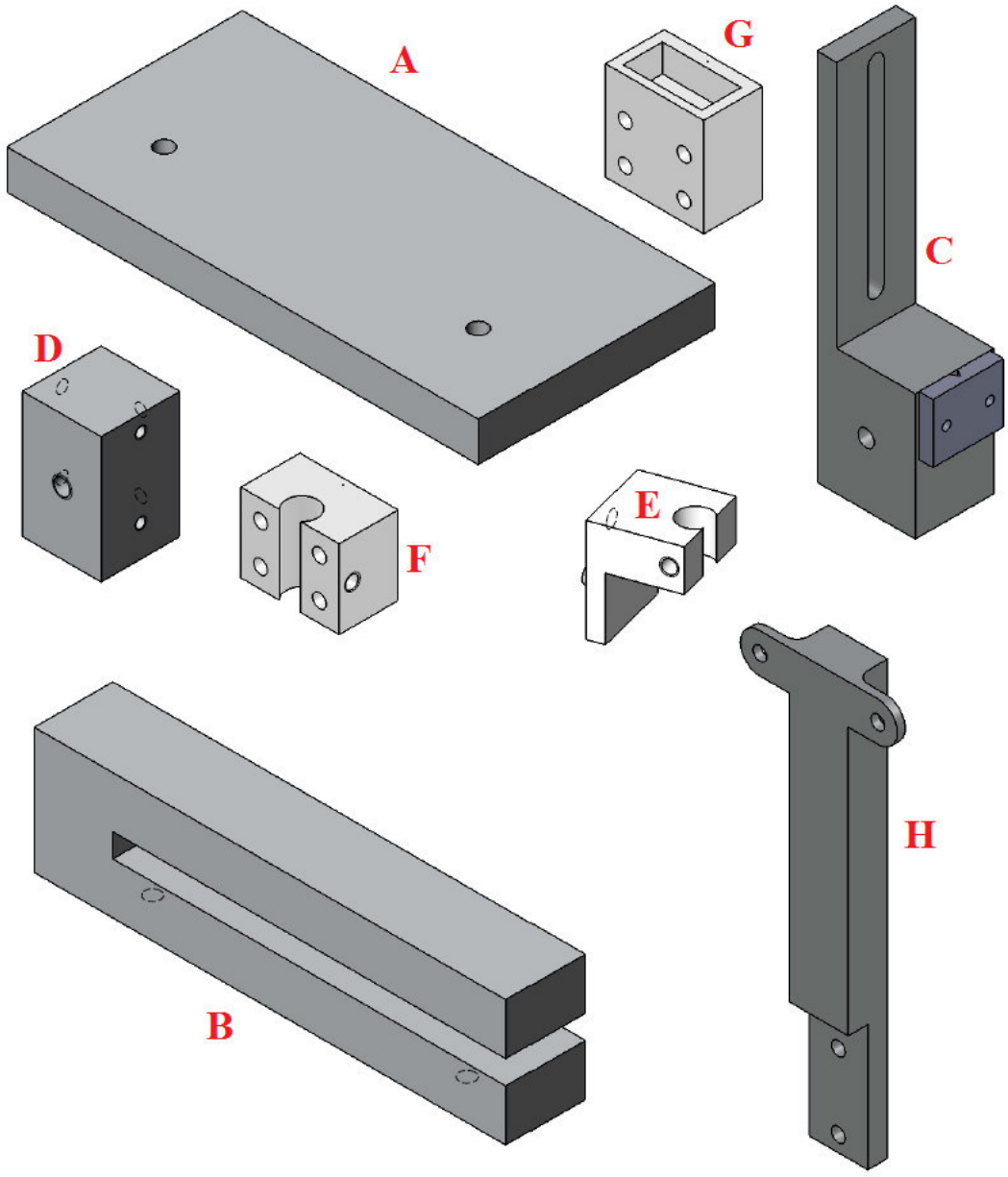


Figure 3.2: Constructed parts for the RUS unit

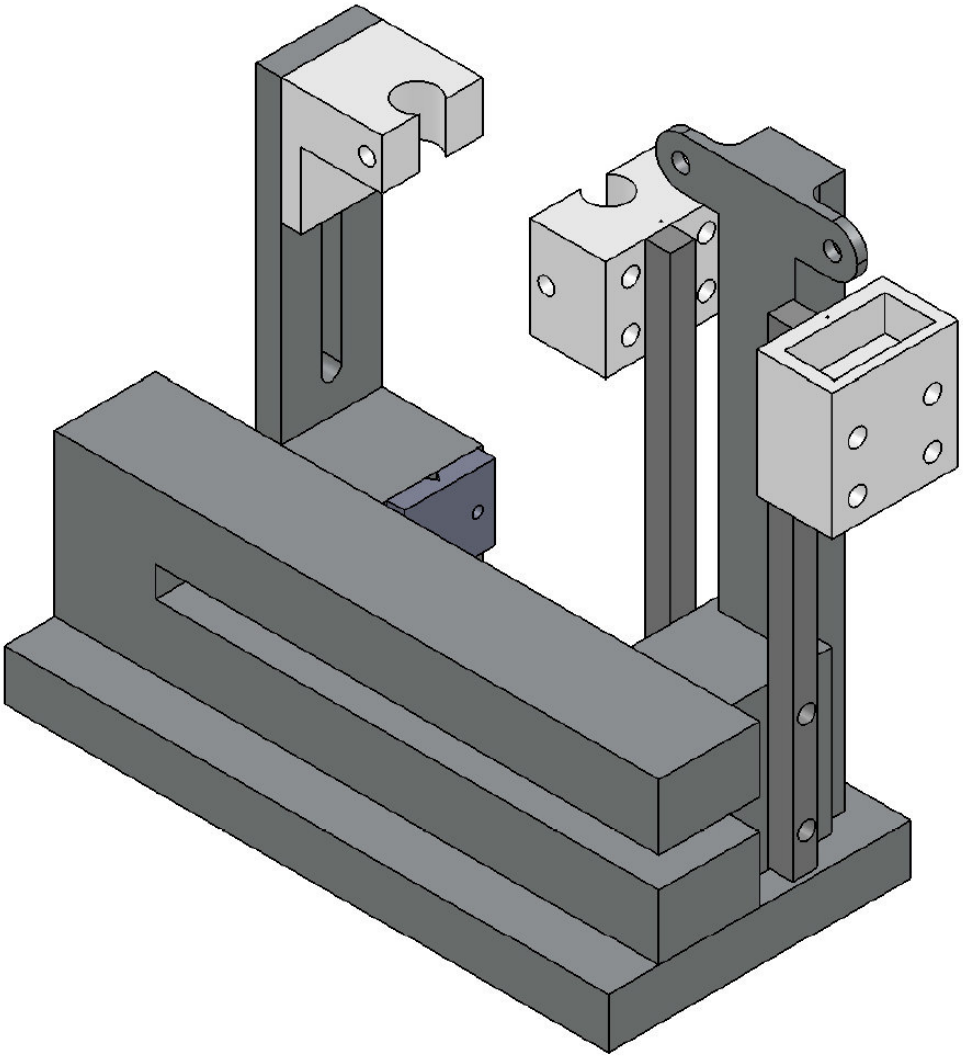


Figure 3.3: Complete arrangement of the constructed parts for the RUS unit

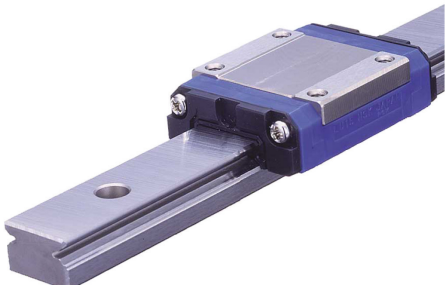


Figure 3.4: NSK Linear Guide Miniature PU series, PU09TR [49]



Figure 3.5: Hepco Motion standard bearing, type SJ13 [50]

3.2 Signal transfer to sample

As mentioned before, there were two piezos in use, which were located outside of the furnace to separate them from the high temperature environment. Two ceramic buffer-rods were adjusted to the correct length and connected to the piezos, to ensure a signal transfer to and from the sample. The straight rod was a 130 mm long and 3 mm wide full cylinder that was cut from a 300 mm rod with an electrical water cooled saw with a diamond blade.

For the construction of the bent rod, two parallel cuts were made lengthwise a hollow ceramic cylinder with 40 mm in diameter and a wall thickness of 3 mm. One end of the cylinder was closed, cutting till the very end resulted in a rod which was shaped like a crook. To address the issue of connecting a round piezo to a square rod, a little aluminum clamp was constructed (figure 3.6). The buffer rods were connected to the piezos with commercially available superglue. Mounted vertically, the rods held the sample in place, transfered the vibrations to and from the sample and brought a distance of 80 mm between the furnace and the piezos. In combination with a cooling plate, this distance was sufficient to guarantee no heat damage. The link between the signal producing oscillator and the piezos was

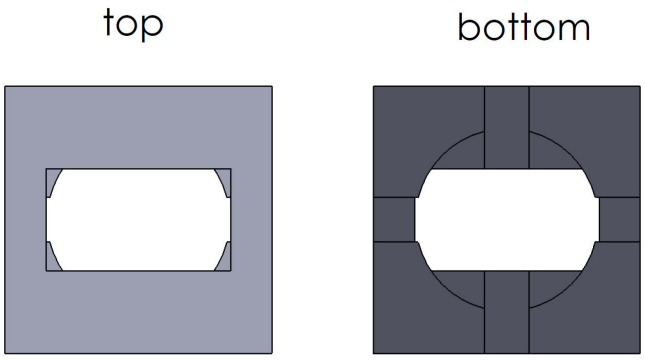


Figure 3.6: A clamp designed to stabilize the connection between piezo and ceramic rod. At the top, the square ceramic rod was inserted. At the bottom, the round piezo was inserted.

established with SMA connectors. The arrangement of the two piezos, as described in section 3.1, would have been influenced by the SMA cable going straight down, touching the ground plate. Therefore, right angled SMA adapters were used (see figure 3.7).



Figure 3.7: Adapter, SMA Jack to SMA Plug, Right Angle [51]

3.3 Cooling

The cooling was achieved with a water cooled aluminum plate which was located between the furnace and the RUS device (see figure 3.9). The requirement for the off-the-shelf cooling plate was to have the same xy dimensions as the base plate of the furnace, therefore extensions had to be constructed for the left/right side of the undersized cooling plate (see appendix figure A11). For the correct height of the plate (mounted directly below the furnace) 4 pedestals (see appendix figure A12) were constructed and connected to the side extensions (see figure 3.10). These pedestals also fastened the cooling plate to the ground plate of the whole construction using 4 parts shown in appendix figure A14. To make sure that the buffer rods passed through the cooling plate, a small slot was carved into the plate. The slot was surrounded by a cylindrical block of Superwool 607 that fitted into the hole on the bottom of the furnace to further improve heat insulation. The water supply for the plate was achieved by Swagelok connectors (see figure 3.8) and rubber tubes. The water supply system was designed to also operate inside a vacuum chamber.

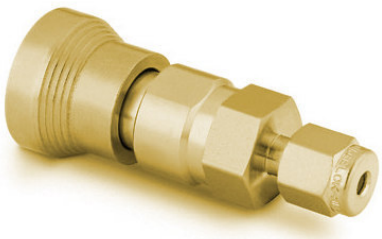


Figure 3.8: Swagelok connectors (female part) to connect or disconnect the water supply.



Figure 3.9: Cooling plate in its original form.

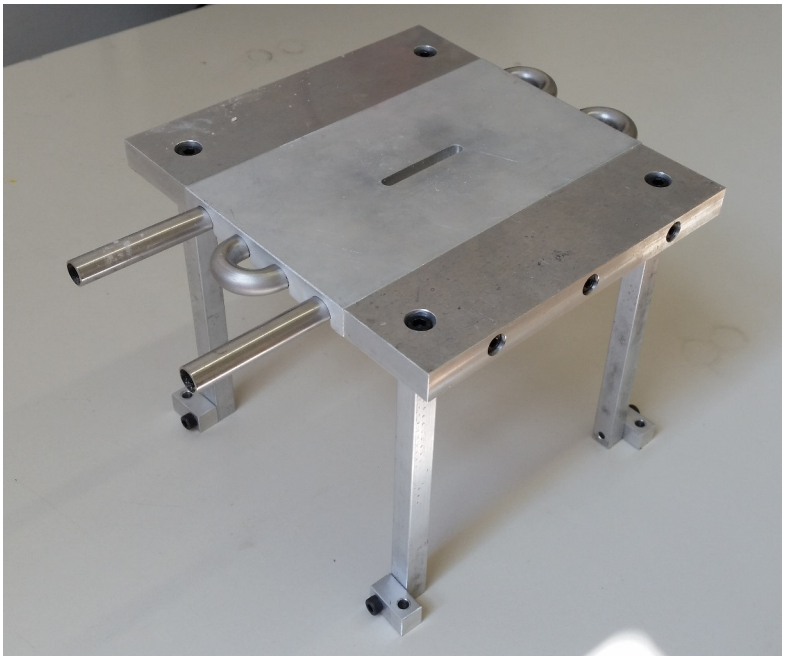


Figure 3.10: Adapted cooling plate.

3.4 Furnace

The heating was accomplished by using 4 ceramic heating units (300 W each), mounted inside the side walls of a cubic hull, which was constructed from 3 mm thick aluminum plates and screwed together with small 'L' shaped parts on the edges of the cube. On the bottom of the furnace, a 50 mm hole was cut in the

plate, in order to be able to lower the furnace onto the RUS device and thereby placing the sample inside the furnace. On the top of the cube, an iron tube (closed on one end, open on the other, $\varnothing = 45$ mm) was mounted to the cover panel (not directly but with ceramic spacers in between, to improve heat insulation, see figure 3.11), facing inwards. This tube was surrounded by the heating units, to ensure a more homogeneous heat distribution in the furnace. The 4 heating units where



Figure 3.11: Abbatron Inc., ceramic spacer with length = 1 inch, $\varnothing = 1/2$ inch, thread #8-32 UNC [52]

mounted to the side walls using clamps provided by the manufacturer (see figure 3.12). The free space between clamps and side wall, as well as the top and bottom interior of the furnace was completely filled with heat insulation material Superwool 607. The electrical wire from the heaters were guided to the outside of the furnace and connected to terminal blocks made of ceramic (see figure 3.13), which were mounted to the outside wall from where additional wiring led to the power supply.

The inside of the furnace is shown in figure 3.14. One can see the iron cylinder that ensures a more homogeneous heat distribution. Figure 3.15 shows the furnace without the cover panel: the arrangement of the heating units can be seen as well as the 50 mm hole for inserting the sample into the furnace. The complete arrangement of parts had to move vertically in order to place the sample inside the furnace. This was accomplished by mounting the whole furnace to the height adjustable carriage of a linear guide from RK Rose+Krieger Inc. (model E18, see figure 3.16). To add extra stability, and to make the separation of the furnace from the carriage easier, two double 'L' shaped parts were constructed and mounted to the outside wall of the furnace. Those two parts had a purpose similar to a hook (see appendix figure A13). It was mandatory for the linear guide to not exceed a maximum height in order to fit into the vacuum chamber and simultaneously be strong enough to withstand the angular momentum caused by the furnace. The vertical height of the carriage/furnace was adjusted by a hand wheel which could be attached to one side of the linear guide. The complete structure (furnace and linear guide) was mounted at the correct height to a block of aluminum, which was then fastened to the ground plate of the whole system. After mounting cooling



Figure 3.12: One of the 4 clamps (manufacturer RS Pro) in which the ceramic heaters were placed [53].



Figure 3.13: RS Pro terminal block, made of ceramic [54]

plate and RUS device into the correct position on the baseplate, the setup for high temperature measurements was complete. The entire arrangement can be seen in figure 3.17.



Figure 3.14: Inside view of the furnace.



Figure 3.15: Top view of the furnace.



Figure 3.16: Linear guide by RK Rose+Krieger Inc., model E18 [55]

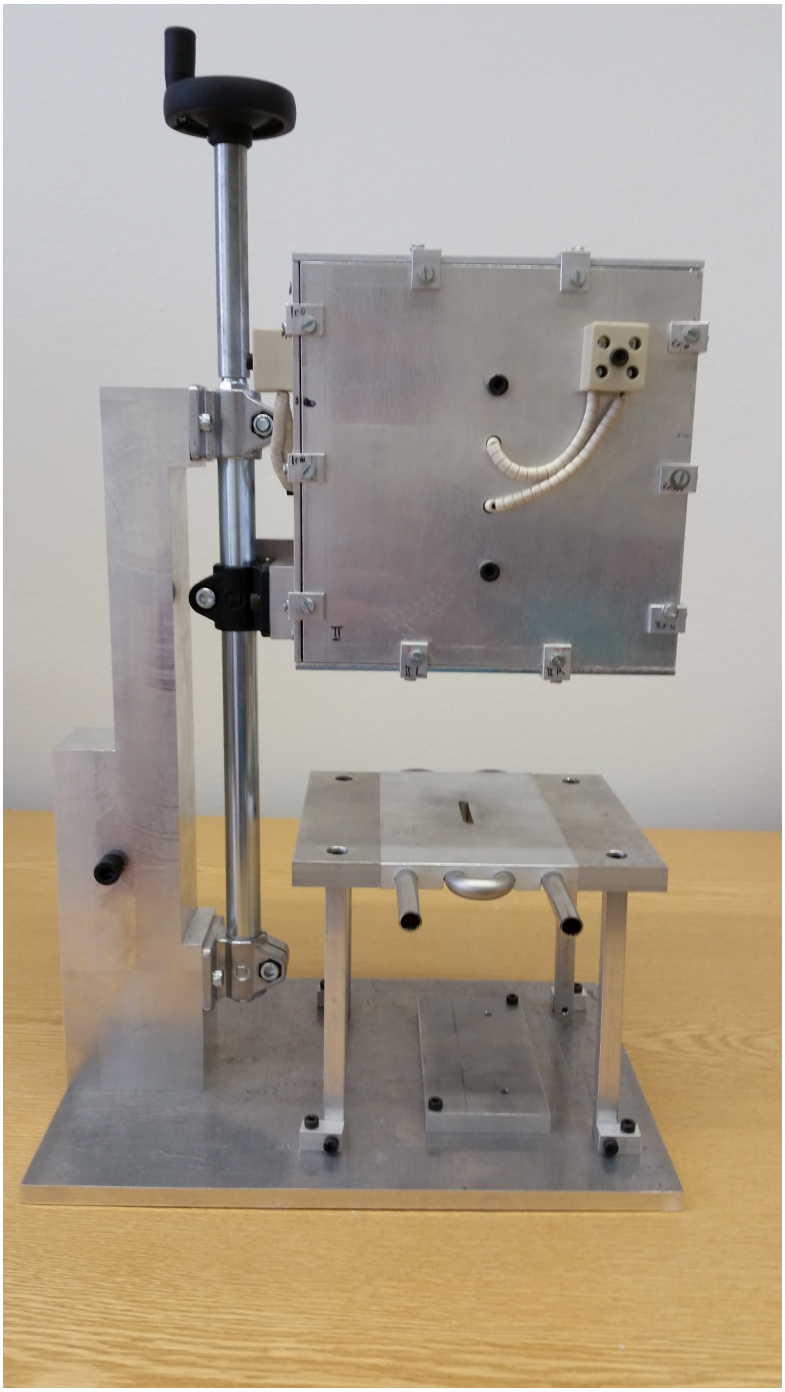


Figure 3.17: The complete setup (without cooling tubes). The cubic furnace is mounted to the E18 linear guide, a hand wheel on the top adjusts the vertical position of the furnace.

3.4.1 Tuning

For heat regulation a proportional-integral-derivative (PID) controller was used (see figure 3.18), which minimizes the difference (the so called error value) between a certain setpoint and a measured variable $x(t)$ over time by adjusting the variable to a new value according to equation 3.1.



Figure 3.18: The Eurotherm 2416 controller.

$$x(t) = K_p e(t) + K_i \int_0^t e(\tau)d\tau + K_d \frac{d}{dt} e(t) \tag{3.1}$$

In this case, $x(t)$ represents the output power of the furnace, K_p, K_i, K_d are the proportional, integral and derivative coefficients and $e(t)$ is the error value. The proportional term produces an output value which is proportional to the current error value. If the value is too high, the system becomes unstable and it is more likely to overshoot the given setpoint. If the value is too small, the controller does not react fast enough to changes in the error value, making is less responsive. The integral term is proportional to the magnitude and duration of the error. It is the sum of the error over time and gives the accumulated offset that should have been corrected previously, which means this term responds to errors from the past and therefore can cause the present value to overshoot. Last but not least, the derivative term puts the output power in proportion to the derivative of the error value over time and improves temporal stability of the controlled system. Since choosing the correct PID parameters is not trivial, the controller is equipped with a software to determine these parameters in a process called tuning. During tuning, the controller matches the characteristics of the controller to that of the process

being controlled (in this case temperature) in order to obtain good control. Good control means:

- Stable 'straight-line' control of the temperature at setpoint without fluctuation
- Neither overshoot nor undershoot of the temperature compared to the temperature setpoint
- Quick response to deviations from the setpoint caused by external disturbances, thereby restoring the temperature rapidly to the setpoint value.

Using the auto-tune function of the controller, the PID parameters for a set of temperatures were determined one by one. The experimental setup for the tuning had to be equal to a proper measurement. Basically, a certain setpoint was given (for example, 200 °C) and then the auto-tune program was launched, which operated by switching the output on and off to induce an oscillation in the measured value. From the amplitude and period of the oscillation, it calculated the tuning parameter values. The first cycle was not complete until the measured value had reached the required setpoint and after two cycles of oscillation the tuning for the selected temperature was complete. This procedure was then repeated for a set of temperatures. A graphical illustration of a typical tuning cycle can be seen in figure 3.19. The calculated PID parameters for the furnace can be seen in table 3.1. The PID parameters were added to the Elastotron software (see

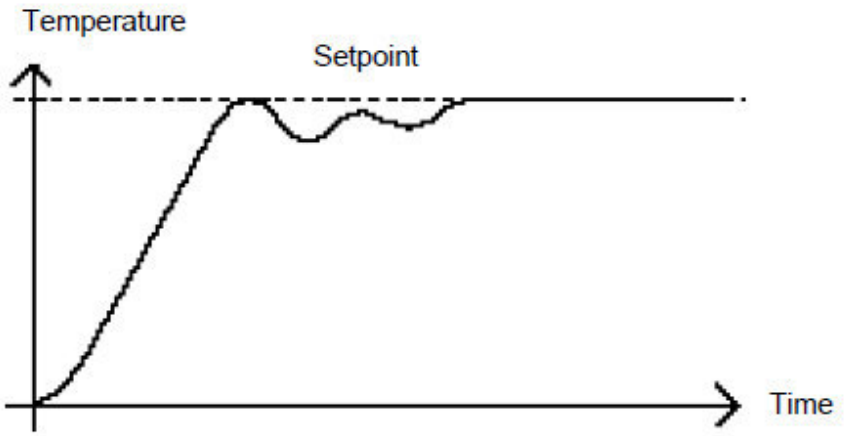


Figure 3.19: Temperature vs time curve in a tuning cycle using the auto-tune function of the controller.

chapter 5) in such a way, that the appropriate parameter was applied as soon as the corresponding temperature was reached. To check if the parameters worked

T[°C]	Pb	ti	td
0-100	86	3486	581
100-150	82	2299	383
150-200	79	1112	185
200-250	74	922	153
250-300	70	733	122
300-350	68	604	100
350-400	66	476	79
400-450	64	428	71
450-500	63	380	63
500-550	61	334	55
550-600	60	284	47
600-650	56	243	40
650-800	44	121	20
800-850	41	111	18
850-900	38	101	16

Table 3.1: PID parameters for several temperatures. Non-bold parameters were calculated with linear interpolation.

properly, a test run was executed which had a similar setup to a high temperature measurement, including a ceramic sample. With the Elastotron software the furnace was programmed to reach a variety of ascending temperatures, with the additional task of holding each temperature setpoint for a specific period of time. The test run revealed very slow heating and a long response time below 250 °C. After additional test runs and manual fine tuning, a suitable set of PID parameters was found (see table 3.2).

T[°C]	Pb	ti	td
0-100	20	1000	350
100-200	60	1112	250
200-400	68	604	100
400-500	65	428	71
500-600	61	334	55
600-700	56	243	40
700-800	44	121	20
800-900	38	101	16

Table 3.2: The final PID parameters for the heating unit.

4 Measurement

4.1 Low temperature 57
4.2 High temperature 59

The measurements were divided into two parts. In the first stage of the experiment, elastic constants were determined at room temperature and afterwards, the setup was changed to measure the samples at temperatures up to 900 °C. The preceding room temperature measurement is a necessity, even if one is only interested in high temperature results, due to the the complexity of data analysis. At high temperatures, the resonant response signal recorded by the receiving piezoelectric transducer has a lower intensity (this is a direct consequence of the buffer rods) and there is a frequency shift towards lower or higher frequencies, depending on the material. It is therefore more challenging to allocate resonant peaks in the measured spectrum. If one can resort to results of a preceding room temperature measurement, helpful information is gained on where the resonant peaks (in the high temperature spectrum) can be expected.

4.1 Low temperature

The experimental setup was different to the high temperature measurement. To ensure optimal results, the sample was placed directly between two piezoelectric transducers (direct-contact setup) because the aluminum oxide buffer rods which task was two keep a distance between the furnace and the transducers were not necessary at this point. The piezoelectric transducers were connected to a network analyzer (see figure 4.1). The frequency of the input signal sent to the transmitting piezo was increased continuously starting at 100-300 kHz and ending at 1.5-2.0 MHz (depending on the sample). The resonant response picked up by the receiving piezo was transformed into an electric signal, sent back to the network analyzer,

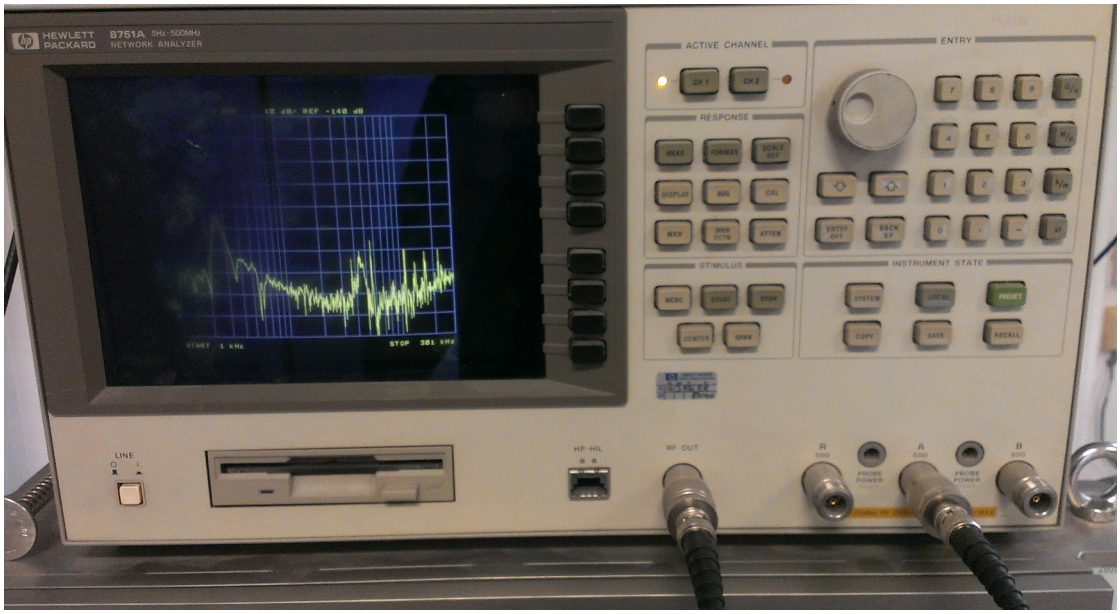


Figure 4.1: Hewlett and Packard 8751A network analyzer

which plotted dB versus frequency. With the controlling software Elastotron 2000 (version 8.04) measurement parameters such as start/end frequency, number of measurements (to increase precision) or strength of the source signal could be adjusted (a more detailed description of this software can be found in chapter 5). At first, one scan was executed using a wide frequency range (1 kHz to 3 MHz) and a low signal strength (-5 to 0 dB) to get a quick overview on where the resonant peaks were located. This initial measurement took less than a minute. Using the information on the resonant frequencies in the recorded spectrum, the frequency interval for the second scan could be restricted to that specific range. The second measurement also featured a higher signal strength of 15 dB and an increased number of scans for the purpose of higher precision. To extract the resonant frequencies from the recorded spectrum, peaks were tagged with a marker provided by the Elastotron software and saved as a text file. The analysis of the frequencies was achieved with a different program (see chapter 5.2). A variety of samples was measured, including 3 ceramics (Si_3N_4, Al_2O_3, ZrO_2), a porous silica glass (Vycor 7930) and 3 thermoelectric alloys (TiNiSn, ZrNiSn, HfNiSn). The specifications of the different samples can be seen in the following table:

Material	Shape	Mass [g]	Diameter [mm]	Height [mm]
Si_3N_4	sphere	3.437 ± 0.001	12.69 ± 0.01	-
Al_2O_3	sphere	4.194 ± 0.001	12.70 ± 0.01	-
ZrO_2	sphere	4.210 ± 0.001	11.50 ± 0.01	-
Vycor 7930	cylinder	0.0047 ± 0.001	2.04 ± 0.01	1.01 ± 0.01
HfNiSn	cylinder	3.4399 ± 0.0001	9.97 ± 0.01	4.75 ± 0.01
ZrNiSn	cylinder	0.2238 ± 0.0001	5.91 ± 0.01	1.08 ± 0.01
TiNiSn	cylinder	0.2218 ± 0.0001	5.95 ± 0.01	1.16 ± 0.01

4.2 High temperature

For high temperature measurements, the newly constructed setup (RUS device, furnace, cooling) was used. As mentioned before, in this setup the sample was put between two buffer rods (buffer-rod setup) and not directly between the piezoelectric transducers (see figure 4.2), resulting in a resonant response signal with lower intensity. The consequence was that the identification of resonant frequency peaks was more challenging compared to room temperature measurements. After the sample was carefully placed between the buffer rods, a couple of test runs were executed to adjust the correct amount of force applied to the sample. If the contact between sample and rod was too weak, the measured spectrum contained no visible RUS peaks, only background noise. As soon as the spectrum contained recognizable RUS peaks, the furnace was lowered onto the sample and the measurement, which was also controlled with the Elastotron software, could start. For the ceramic samples (Si_3N_4, Al_2O_3, ZrO_2) a spectrum was recorded every 100 °C, starting at 100 °C and ending at 900 °C, for the thermoelectric samples (HfNiSn, TiNiSn, ZrNiSn), a spectrum was recorded every 50 °C, starting at 50 °C and ending at 550 °C. At each temperature set point, before the RUS measurement was initiated, the corresponding temperature was held for 10 min, to ensure thermal equilibrium within the volume of the sample.



Figure 4.2: A TiNiSn sample placed between two aluminum oxide rods.

5 Software

5.1 Elastotron 61
5.1.1 Eurotherm controller 65
5.2 Frequency analysis program 67

5.1 Elastotron

As briefly described in chapter 4, the Elastotron 2000 (version 8.04) software was used to control the network analyzer and the heater. A screen shot of the softwares interface can be seen in figure 5.1. Prior to the measurement, the source power (i.e. the signal strength of the outgoing signal) was adjusted using the sliding bar in the top left corner (figure 5.2). Going further to the right side of the screen shot, the start and stop frequencies was defined as well as the number of measurements and the number of measuring points per run. (figure 5.5).

On the top right corner, the zoom buttons were used to zoom into the spectrum to ensure a more precise peak marking. A typical frequency spectrum looks like figure 5.7. Thin, spiky peaks which represent resonant frequencies from different eigenmodes were marked using a software marker provided by the Elastotron program (vertical lines in figure 5.8). For an accurate determination of elastic constants, at least 10 peaks had to be selected. The values of the frequencies which correspond to the resonant peaks are listed in the lower left window (figure 5.4). These frequencies were exported to a text file for the subsequent data analysis. Sometimes, due to defects in the material or imperfections in the samples dimension, there is not one sharp peak recorded, but 2 very close to each other (within a couple of Hz). Since it is not possible to say which one of these peaks represent the correct resonant frequency, a comparison with the respective calculated frequency was necessary. An example of such a 'double peak' can be seen in figure 5.3.

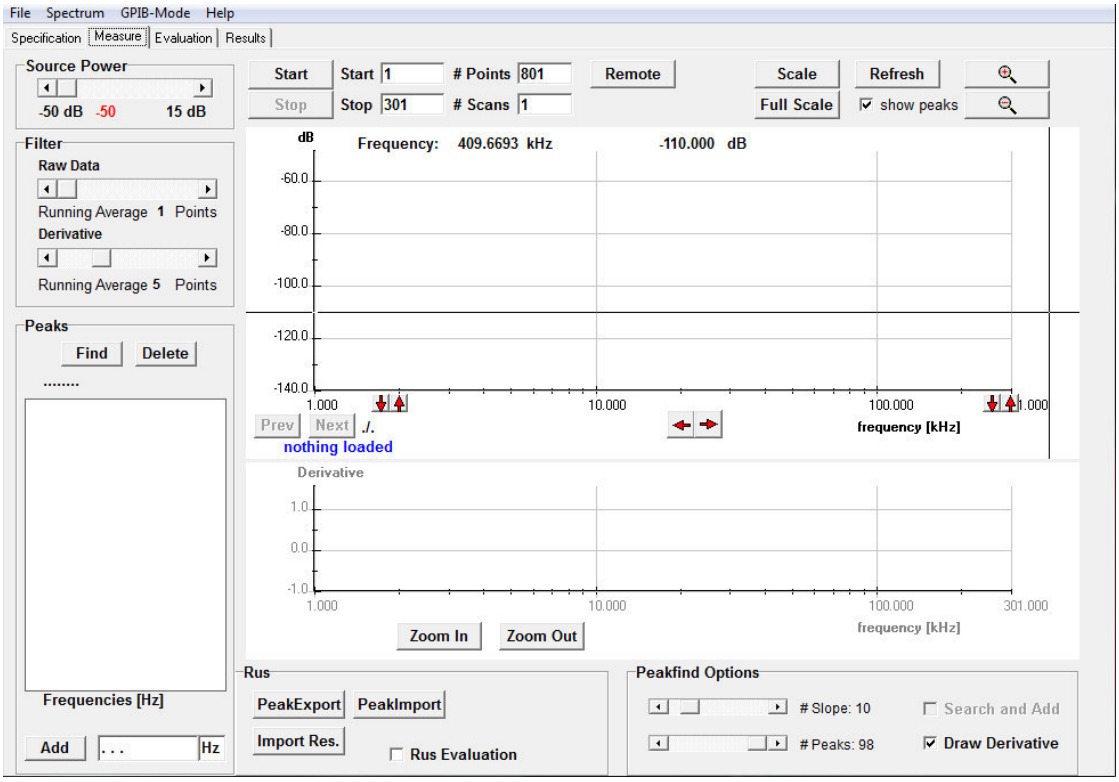


Figure 5.1: Elastotron software

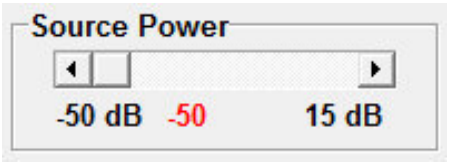


Figure 5.2: Signal strength adjustment. Ranging from -50 to 15 dB.

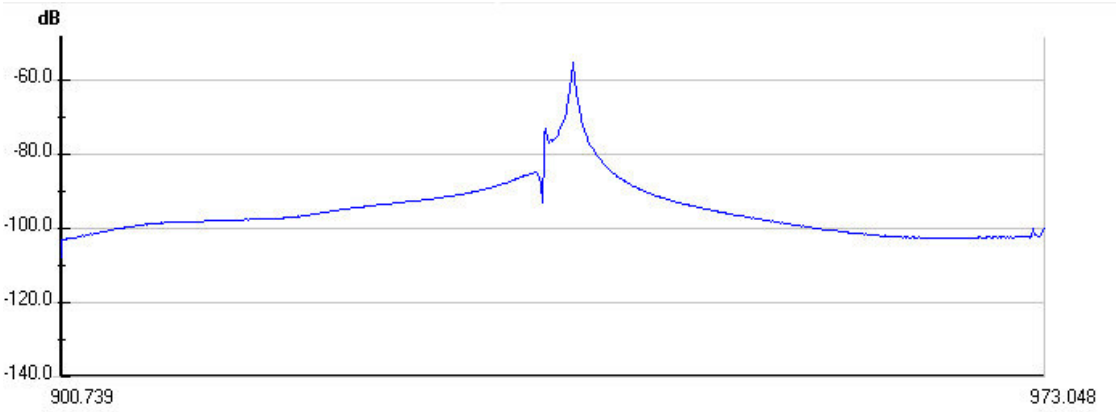


Figure 5.3: 'Double' peak which makes it unclear which frequency should be chosen.

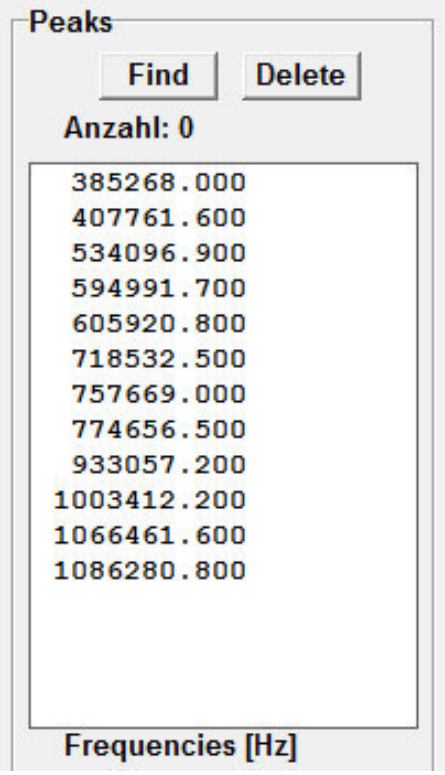


Figure 5.4: Resonant frequencies corresponding to peaks that were marked in the spectrum.

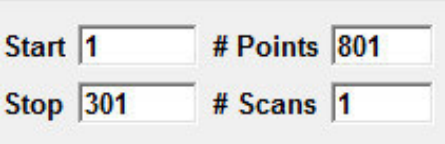


Figure 5.5: The frequency interval in which the measurement takes place can be adjusted, the unit is kHz. In this example, 1 scan is performed with 801 scanning points.

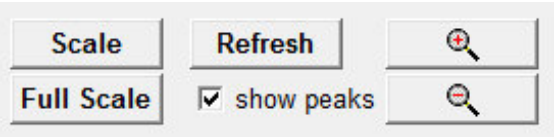


Figure 5.6: Zoom buttons to mark peaks more precisely.

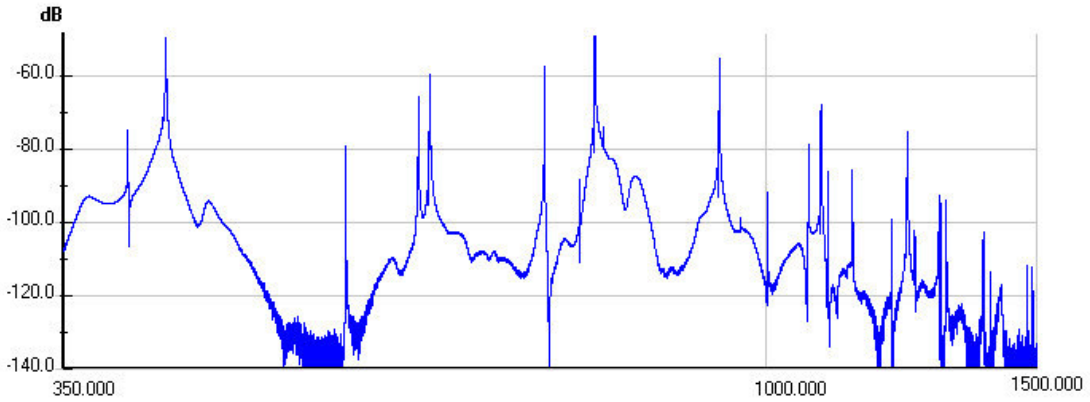


Figure 5.7: RUS spectrum. Intensity [dB] versus frequency [kHz].

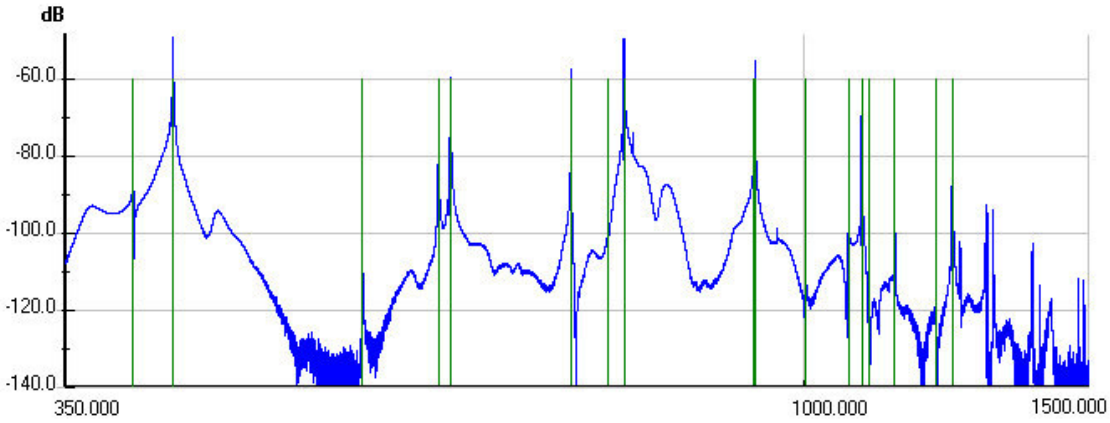


Figure 5.8: The same RUS spectrum as before, this time with marked peaks.

5.1.1 Eurotherm controller

The Eurotherm 2416 PID controller was also operated via the Elastotron software. Therefore, the high temperature measurements could be executed in an automated process. Figure 5.9 shows a screen shot of this software. To ensure that the controller worked as required, correct PID parameters had to be implemented. Afterwards, the measurement settings were adjusted in the spreadsheet on the right hand side:

- **Rate [°C/min]:** determined the heating rate. Usually the true value was much lower at the beginning, and got closer to the selected value at higher temperatures. The constructed furnace was reacting rather slowly to any changes of the temperature set point, but only below 200 °C.
- **Temp [°C]:** selected the next temperature set point.
- **Hold [min]:** determined how long the selected temperature was held before the RUS measurement was started. The samples heat conductivity was the deciding factor for this value. For small ceramic samples we used 10 minutes. For metallic samples, it can be lower.
- **Tolerance [°C/min]:** This value determined the allowed temperature fluctuations within the time interval set with *Hold*.
- **Start/End [Hz]:** start and end frequency for the RUS measurement.
- **# Scans:** gave the number of scans inside the selected frequency interval.

The Log window showed the temperature set point (SP) and the current temperature (OP). The Display window showed temperature vs time.

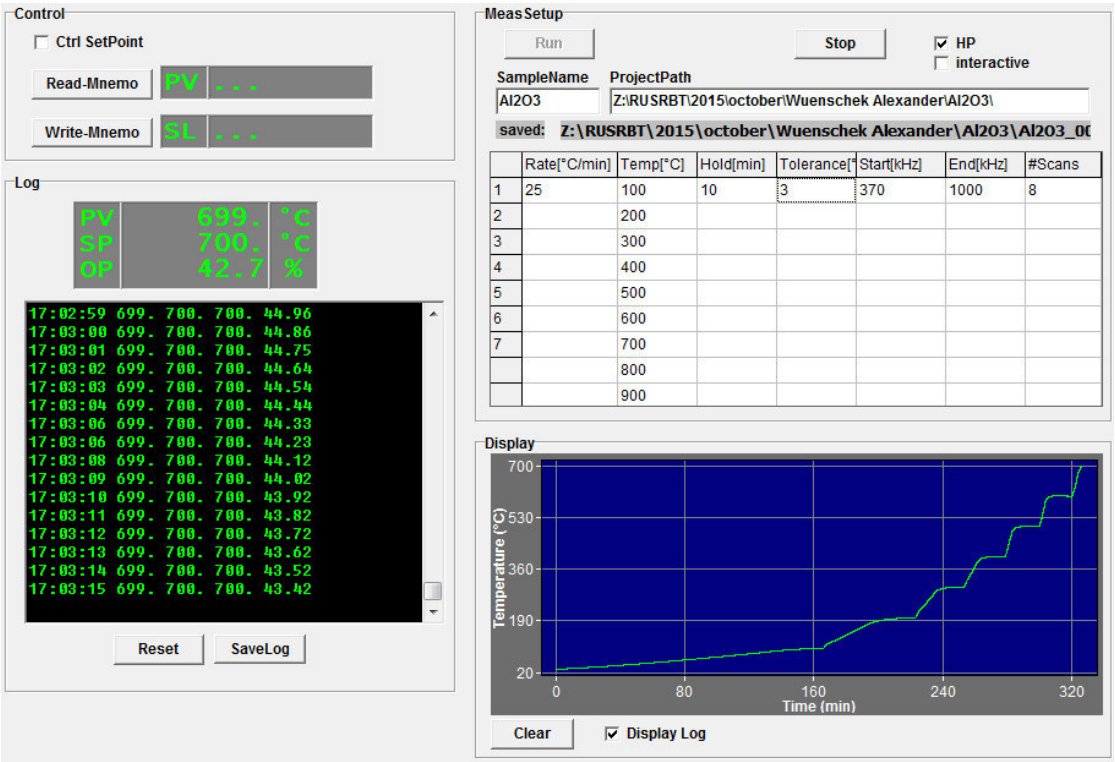


Figure 5.9: Elastotron software to operate the Eurotherm controller.

5.2 Frequency analysis program

The calculation of resonant frequencies and the subsequent fit with the measured frequencies was achieved with a different program (it will be referred to as RUS program). The program ran on a Unix system and was executed via the terminal. Step 1 was calculating the sample's resonant frequencies using the input parameters mass, x, y, z dimensions, shape, Young's modulus (E) and Poisson's ratio (ν), the last two parameters (E and ν) had to be guessed by trial and error. The input values were written into a XML (Extensible Markup Language: a widely used format to encode e.g. textual data documents) file which was the input file for the RUS program. If the calculated frequencies were higher than the measured ones, E and/or ν had to be lowered and vice versa. Step 2 was to adjust the frequencies in the input file in order to be able to execute a data fit:

- Due to the samples symmetry, some resonant frequencies appeared multiple times in the calculation. To ensure a successful fit, multiples of a specific calculated frequency and the corresponding measured frequency had to be equal. This can be seen in figure 5.10. For example, the first calculated frequency that matched a measured one, was calculated 5 times. This means, the first measured frequency, in this case 305834.5 Hz, had to be used 5 times as well.

- Certain frequencies were calculated but could not be measured, because it is unlikely to detect all resonant frequencies in one measurement. These frequencies had to be listed in the input file, otherwise the fit would have been unsuccessful. But since such a value had no measured counterpart, the frequency was given a weight of zero in the fit.

- In contrast, there were frequencies measured which were not calculated. Those frequencies were most likely resonant responses from the piezoelectric transducers, or from the buffer rods and were simply deleted from the input file.

The adapted XML file was implemented into the RUS program which fitted measured and calculated frequencies by minimized an error function in an iterative process (for details see chapter 1.2.5) and afterwards determined E, ν and G from the fitted frequencies.

```
<rus>
    <fit algorithm="neldermead">
        <iterations value="100"/>
        <fitdimen value="false"/>
    </fit>
  <material>
  <elasticity symmetry="isotropic">
      <Ex value="270" constraint="false"/>
      <NUxy value="0.31" constraint="false"/>
  </elasticity>
  <sample id="VX7A42" shape="spheriod_xyz">
    <computation type="singlesum" symmetry="orthorombic" x="14" y="14" z="14" R="10"/>
    <description>1337</description>
    <xdimen value="11.500" sigma="0.001"/>
    <ydimen value="11.500" sigma="0.001"/>
    <zdimen value="11.500" sigma="0.001"/>
    <mass value="4.210" sigma="0.0001"/>
     <measured>
<eigenfrequency value=" 305834.500" sigma="1" weight="1" times="5"/>
<eigenfrequency value=" 323992.500" sigma="1" weight="1" times="5"/>
<eigenfrequency value=" 427315.300" sigma="1" weight="0" times="3"/>
<eigenfrequency value=" 472198.600" sigma="1" weight="1" times="7"/>
<eigenfrequency value=" 481385.200" sigma="1" weight="1" times="7"/>
<eigenfrequency value=" 614563.000" sigma="1" weight="1" times="5"/>
<eigenfrequency value=" 616474.900" sigma="1" weight="1" times="9"/>
<eigenfrequency value=" 622044.500" sigma="1" weight="1" times="9"/>
<eigenfrequency value=" 626000.000" sigma="1" weight="0" times="1"/>
<eigenfrequency value=" 703175.300" sigma="1" weight="1" times="3"/>
<eigenfrequency value=" 742718.800" sigma="1" weight="1" times="11"/>
<eigenfrequency value=" 765249.100" sigma="1" weight="1" times="11"/>
<eigenfrequency value=" 811000.000" sigma="1" weight="0" times="7"/>
<eigenfrequency value=" 865178.900" sigma="1" weight="1" times="13"/>
<eigenfrequency value=" 872000.000" sigma="1" weight="0" times="5"/>
<eigenfrequency value=" 873000.000" sigma="1" weight="0" times="3"/>
<eigenfrequency value=" 903882.400" sigma="1" weight="1" times="13"/>
<eigenfrequency value=" 984951.800" sigma="1" weight="1" times="15"/>
```

Figure 5.10: The input XML file for the RUS program. In section *sample* the input parameters (E, ν, mass and xyz dimensions) can be entered. In section *eigenfrequencies* the measured frequencies are listed.

6 Results

6.1 Si_3N_4 69
6.2 Al_2O_3 76
6.3 ZrO_2 82
6.4 HfNiSn 89
6.5 TiNiSn 97
6.6 ZrNiSn 105
6.7 Vycor 7930 113
6.8 Discussion 114

This section contains RUS spectra for all samples, spreadsheets of all resonant frequencies that were extracted from the spectra and shows the temperature dependence of the Young's modulus, the shear modulus and the Poisson's ratio.

6.1 Si_3N_4

The following RUS spectra were recorded:

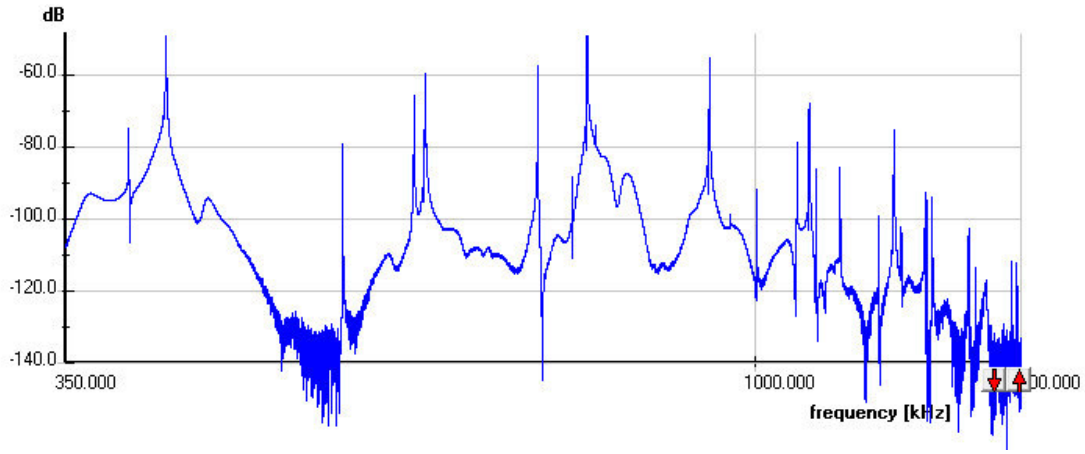


Figure 6.1: Si_3N_4 sample measured at 25 °C. Frequency interval 350-1500 kHz.

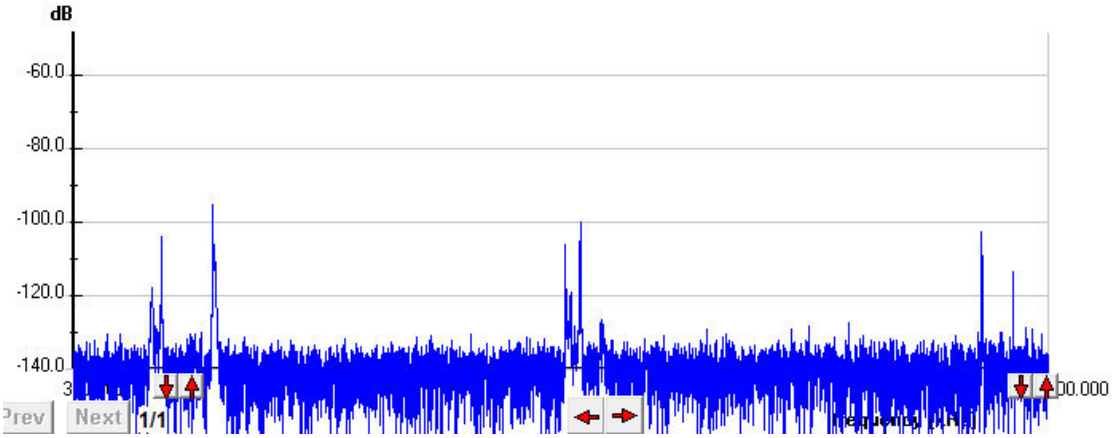


Figure 6.2: Si_3N_4 sample measured at 100 °C. Frequency interval 350-1000 kHz.

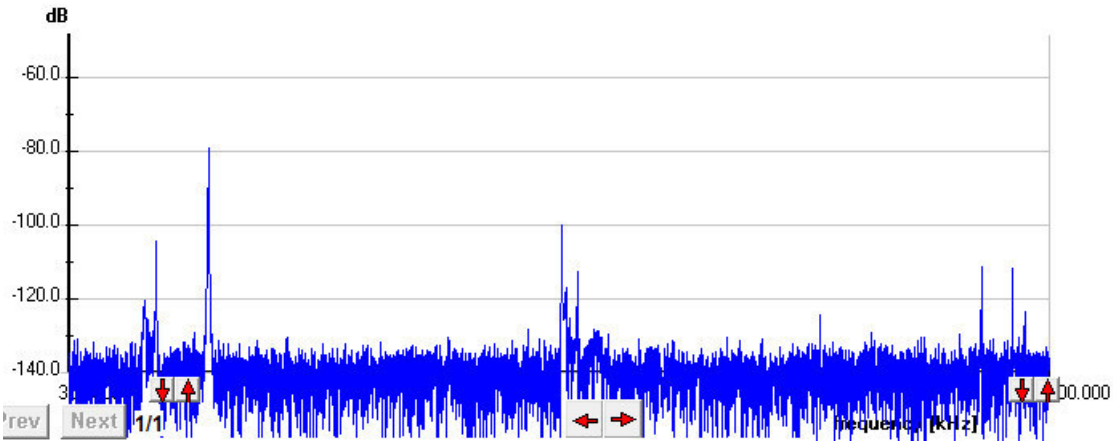


Figure 6.3: Si_3N_4 sample measured at 200 °C. Frequency interval 350-1000 kHz.

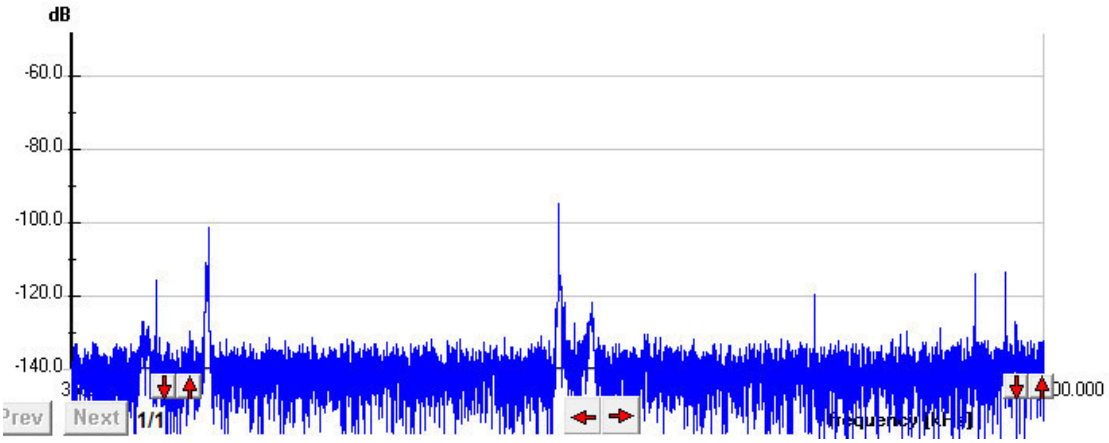


Figure 6.4: Si_3N_4 sample measured at 300 °C. Frequency interval 350-1000 kHz.

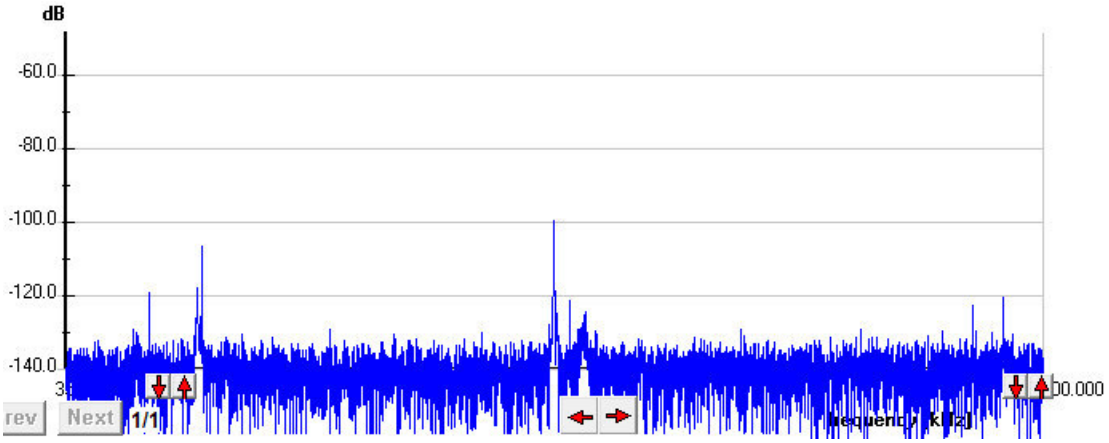


Figure 6.5: Si_3N_4 sample measured at 400 °C. Frequency interval 350-1000 kHz.

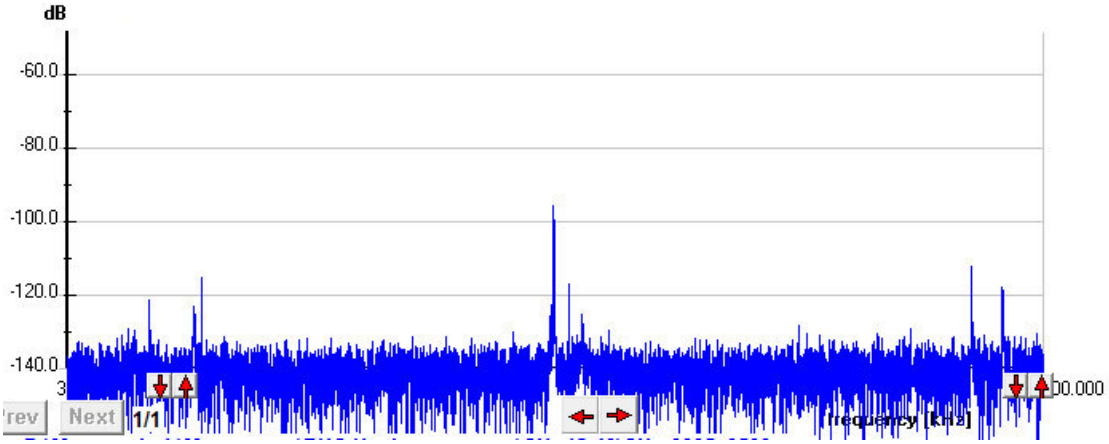


Figure 6.6: Si_3N_4 sample measured at 500 °C. Frequency interval 350-1000 kHz.

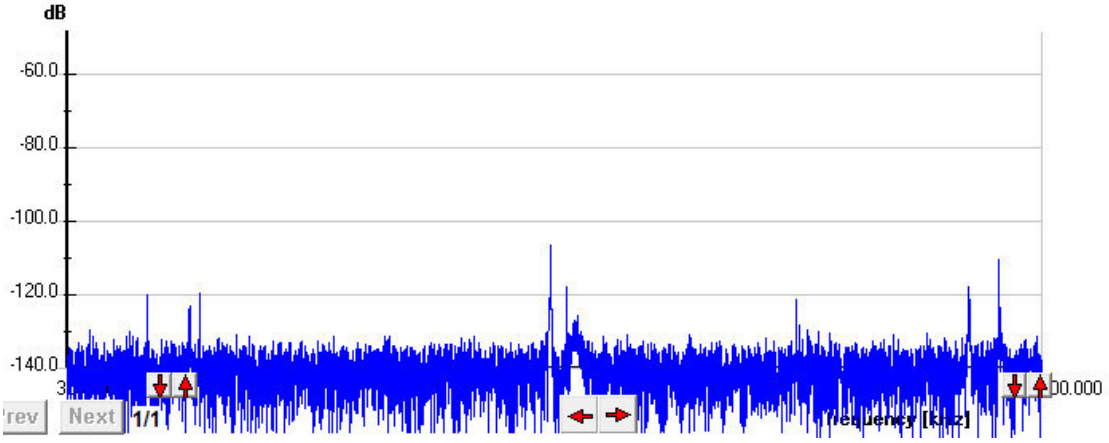


Figure 6.7: Si_3N_4 sample measured at 600 °C. Frequency interval 350-1000 kHz.

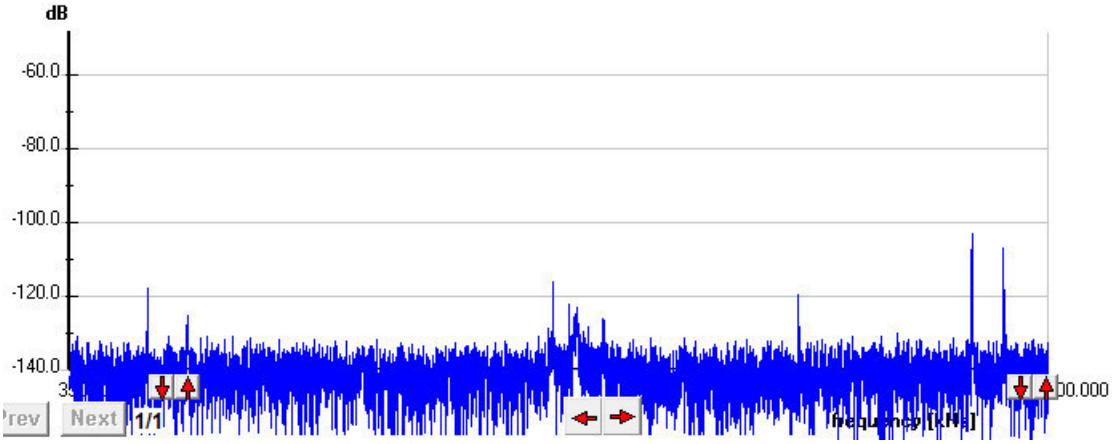


Figure 6.8: Si_3N_4 sample measured at 700 °C. Frequency interval 350-1000 kHz.

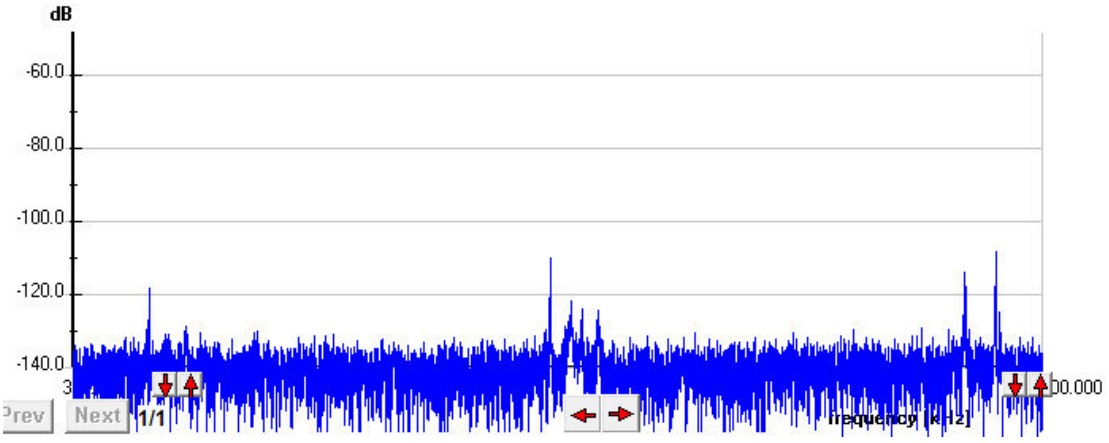


Figure 6.9: Si_3N_4 sample measured at 800 °C. Frequency interval 350-1000 kHz.

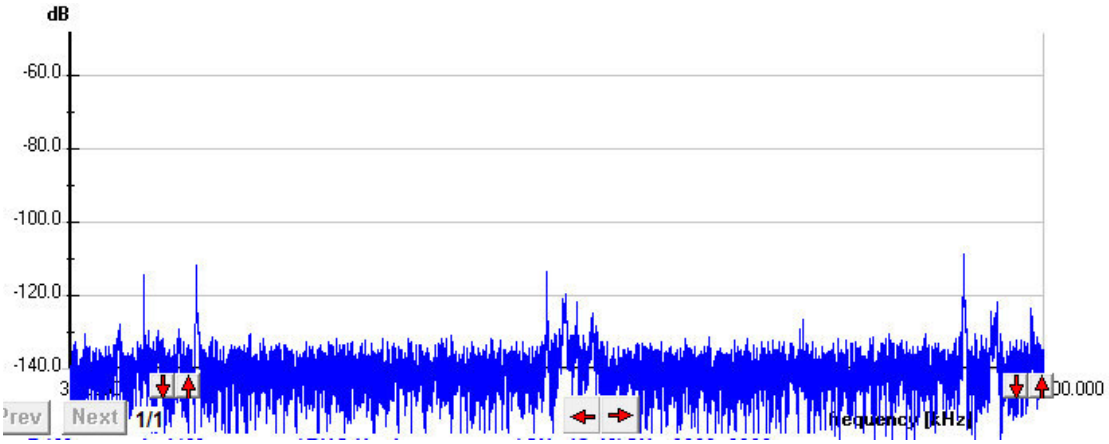


Figure 6.10: Si_3N_4 sample measured at 900 °C. Frequency interval 350-1000 kHz.

Table 6.1: Resonant frequencies in [Hz] for the Si_3N_4 sample.

25 °C	100 °C	200 °C	300 °C	400 °C	500 °C	600 °C	700 °C	800 °C	900 °C
385312	384552	384081	383447	382918	382290	381534	380789	379902	378911
407746	406702	406219	405582	405013	404351	403554	402699	401835	400776
533825	593960	593213	592254	591412	590535	589295	588124	586762	585198
533963	603944	603219	602248	601492	600503	599338	598057	596760	595088
594911	772936	781814	780655	779702	768516	767025	765385	763695	771137
604013	931142	929978	928499	927327	925802	923991	922003	919904	917475
605405	962582	961463	959997	958558	957045	955134	953071	950928	950642
718263									987224
774617									
933155									
1002624									
1003176									
1066110									
1066407									

Table 6.2: Si_3N_4: E, G and ν from 25 to 900 °C

T [°C]	E [GPa]	± [GPa]	ν	±	G [GPa]	± [GPa]
25	307.34	0.01	0.271	0.001	120.87	0.01
100	307.71	0.01	0.277	0.001	120.46	0.01
200	306.88	0.01	0.276	0.001	120.16	0.01
300	305.85	0.01	0.276	0.001	119.79	0.01
400	305.20	0.01	0.277	0.001	119.46	0.01
500	304.25	0.01	0.277	0.001	119.07	0.01
600	303.13	0.01	0.277	0.001	118.59	0.01
700	301.80	0.01	0.277	0.001	118.09	0.01
800	300.46	0.01	0.277	0.001	117.56	0.01
900	297.46	0.01	0.268	0.001	117.22	0.01

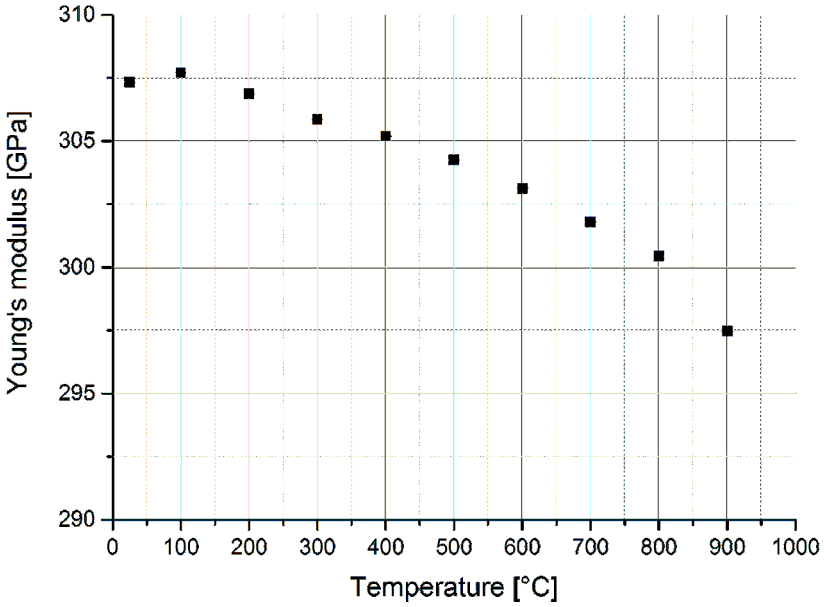


Figure 6.11: Young's modulus vs temperature for Si_3N_4.

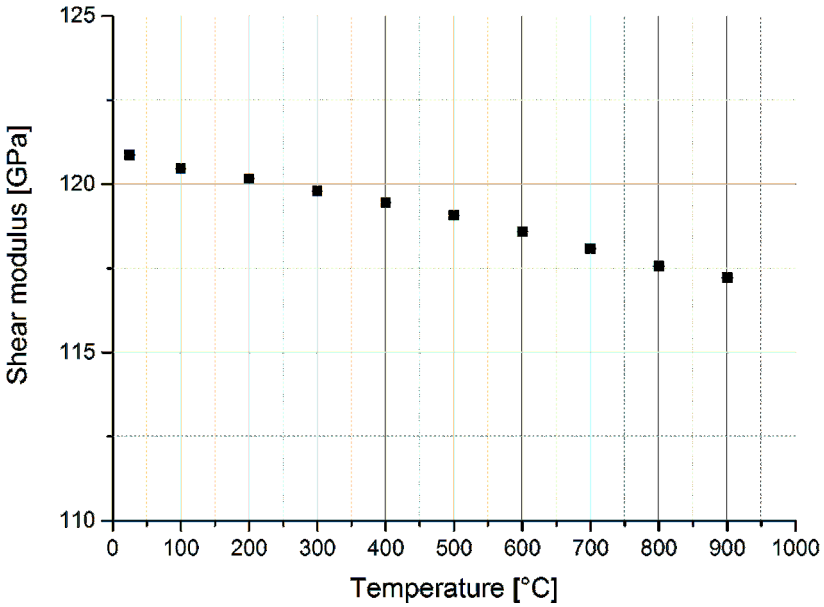


Figure 6.12: Shear modulus vs temperature for Si_3N_4.

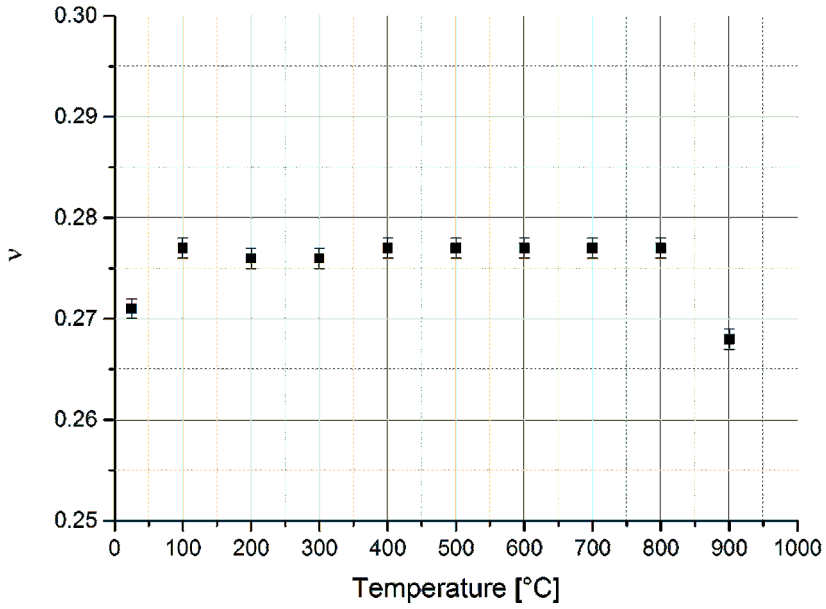


Figure 6.13: Poisson's ratio vs temperature for Si_3N_4.

6.2 Al_2O_3

The following RUS spectra were recorded:

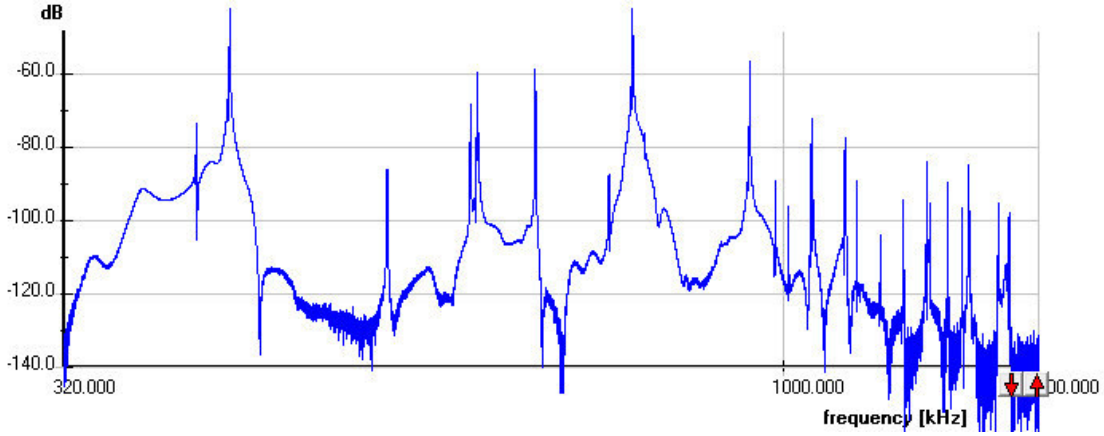


Figure 6.14: Al_2O_3 sample measured at 25 °C. Frequency interval 370-1000 kHz.

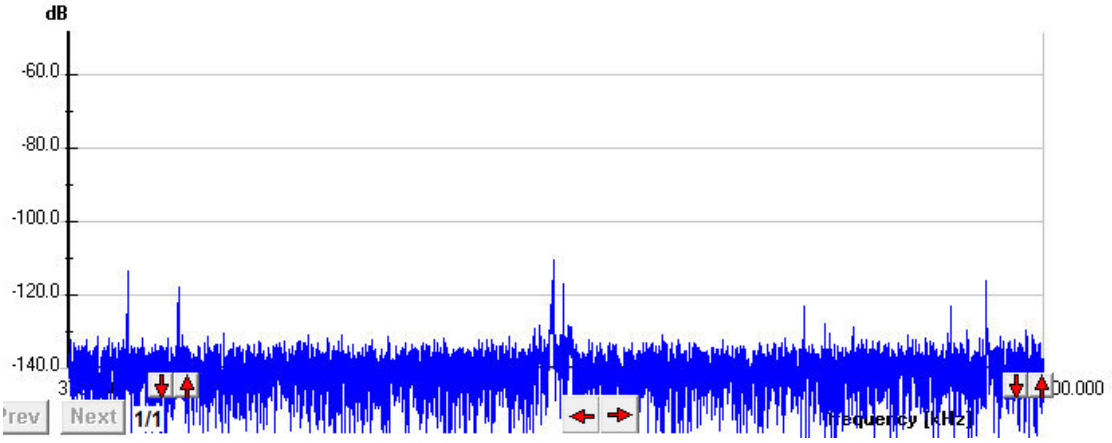


Figure 6.15: Al_2O_3 sample measured at 100 °C. Frequency interval 370-1000 kHz.

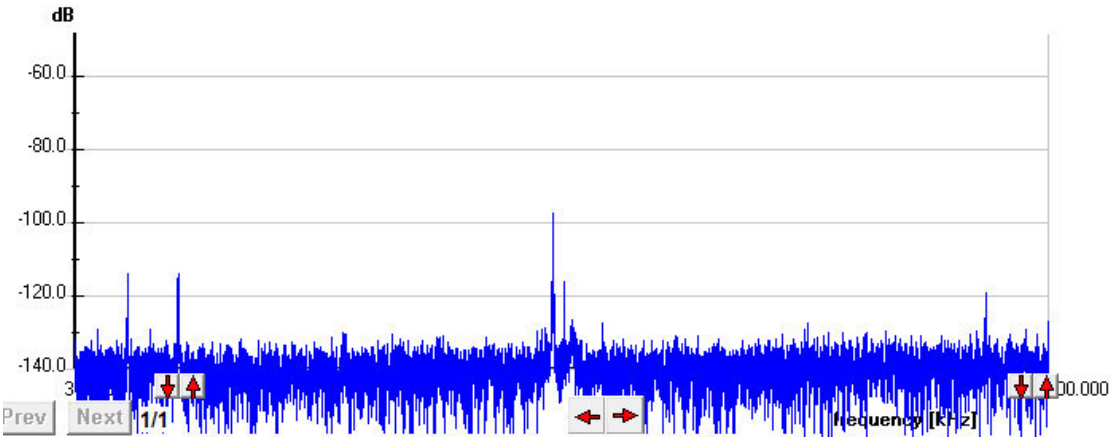


Figure 6.16: Al_2O_3 sample measured at 200 °C. Frequency interval 370-1000 kHz.

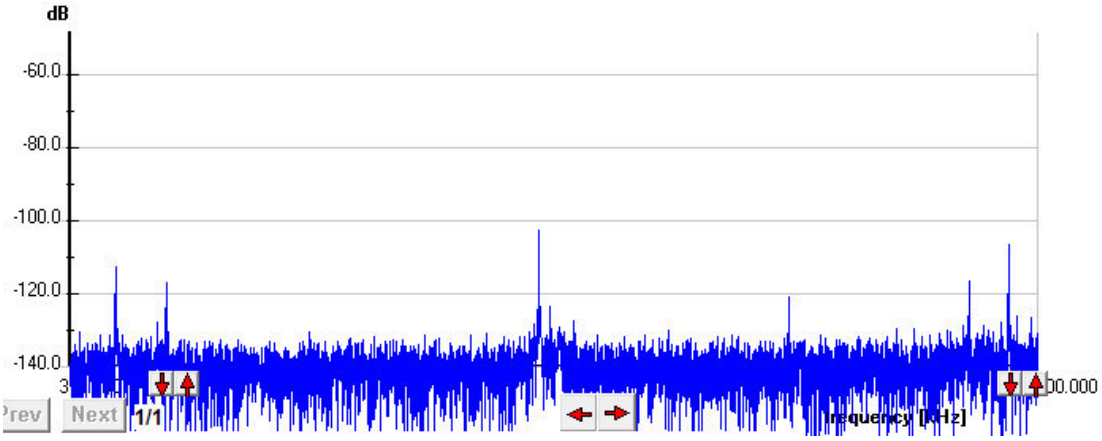


Figure 6.17: Al_2O_3 sample measured at 300 °C. Frequency interval 370-1000 kHz.

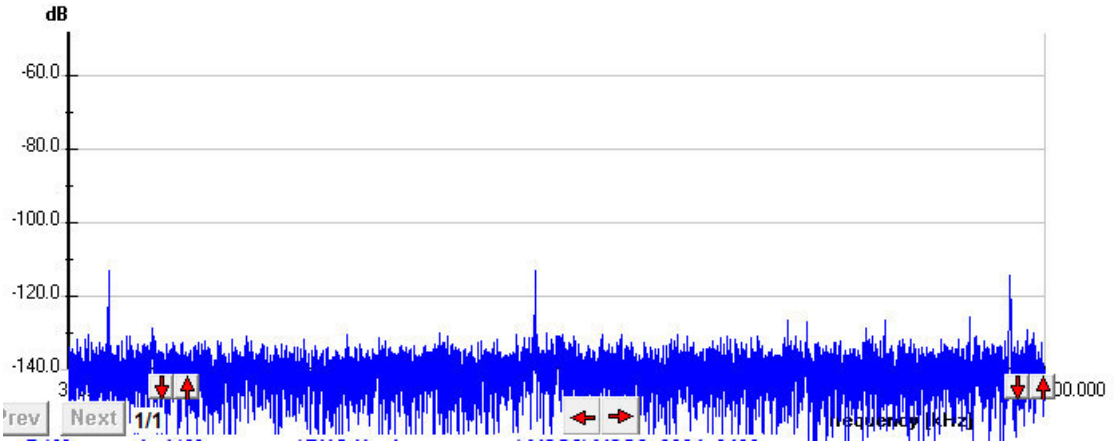


Figure 6.18: Al_2O_3 sample measured at 400 °C. Frequency interval 370-1000 kHz.

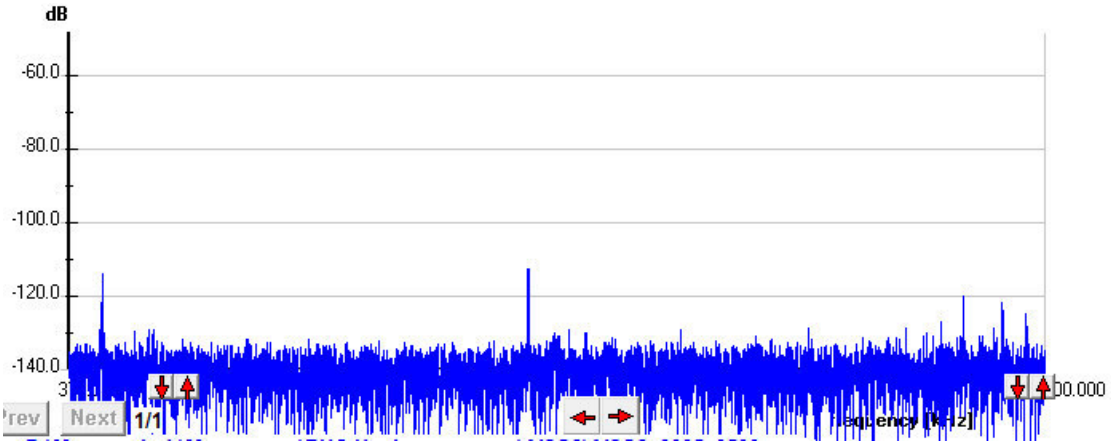


Figure 6.19: Al_2O_3 sample measured at 500 °C. Frequency interval 370-1000 kHz.

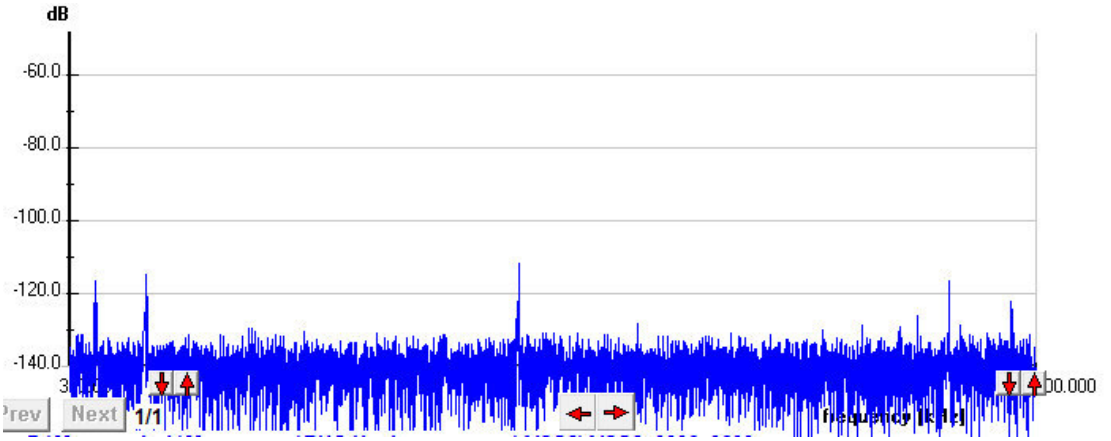


Figure 6.20: Al_2O_3 sample measured at 600 °C. Frequency interval 370-1000 kHz.

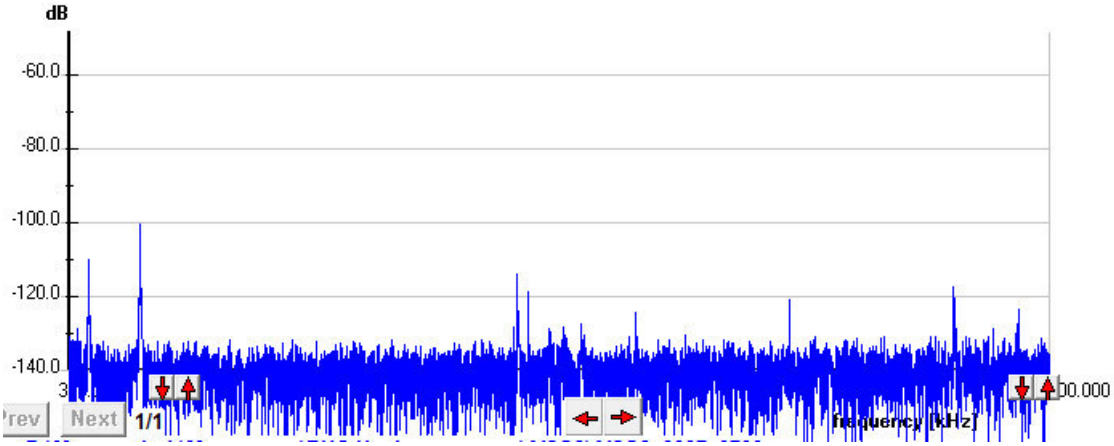


Figure 6.21: Al_2O_3 sample measured at 700 °C. Frequency interval 370-1000 kHz.

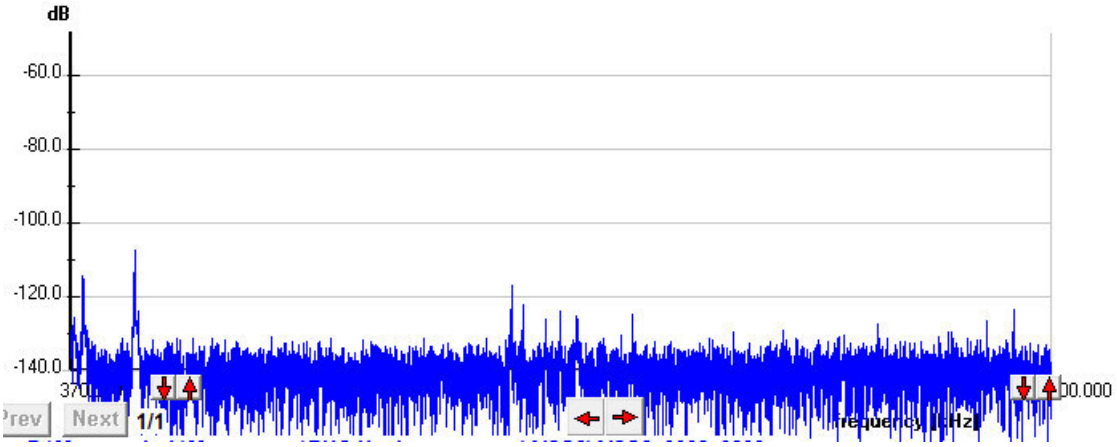


Figure 6.22: Al_2O_3 sample measured at 800 °C. Frequency interval 370-1000 kHz.

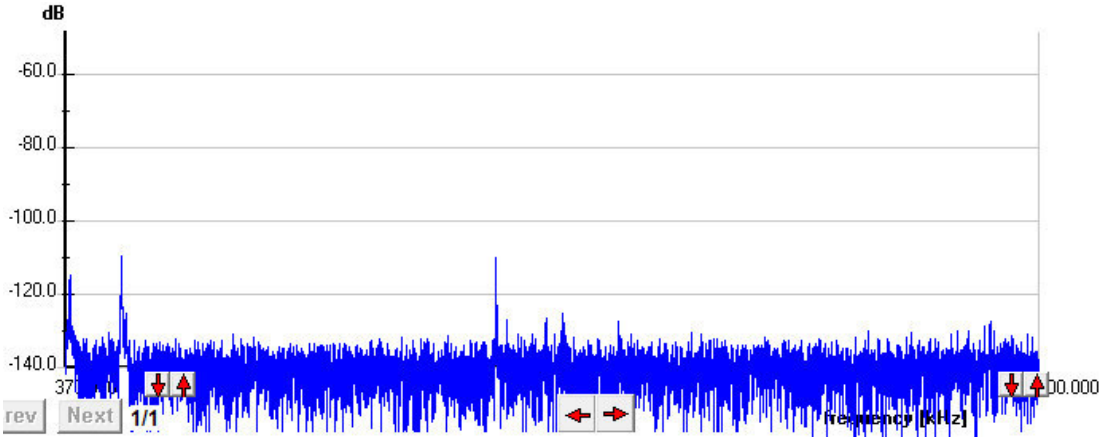


Figure 6.23: Al_2O_3 sample measured at 900 °C. Frequency interval 370-1000 kHz.

Table 6.3: Resonant frequencies in [Hz] for the Al_2O_3 sample.

25 °C	100 °C	200 °C	300 °C	400 °C	500 °C	600 °C	700 °C	800 °C	900 °C
394813	392835	390470	387891	385281	382687	379951	377308	374514	371548
415912	413758	411317	408677	402877	403193	400380	397527	394647	391632
533574	606352	602705	598802	594827	590672	587108	582904	578593	574231
533721	613069	609473	599271	595252	616144	663769	589400	585106	580844
534550	783799	938154	605629	769213	886221	885076	657517	598964	701640
609559	800050	977574	621258	784166	920114	913832	767780	607677	935697
616353	910294	988562	774249	926265	957737	975020	907627	762079	951711
675513	943809	999759	932347	964305	981237		944134	838735	
758875	983140		970765	964606			969420	936981	
787901								962774	
948825									
988216									
1009263									

Table 6.4: Al_2O_3: E, G and ν from 25 to 900 °C

T [°C]	E [GPa]	± [GPa]	ν	±	G [GPa]	± [GPa]
25	378.43	0.01	0.207	0.001	156.71	0.01
100	376.91	0.01	0.222	0.001	153.53	0.01
200	365.98	0.01	0.201	0.001	152.31	0.01
300	361.70	0.01	0.203	0.001	150.32	0.01
400	358.64	0.01	0.216	0.001	147.37	0.01
500	350.98	0.01	0.199	0.001	146.30	0.01
600	346.93	0.01	0.196	0.001	145.02	0.01
700	341.54	0.01	0.202	0.001	142.00	0.01
800	335.49	0.01	0.203	0.001	139.40	0.01
900	330.34	0.01	0.196	0.001	138.02	0.01

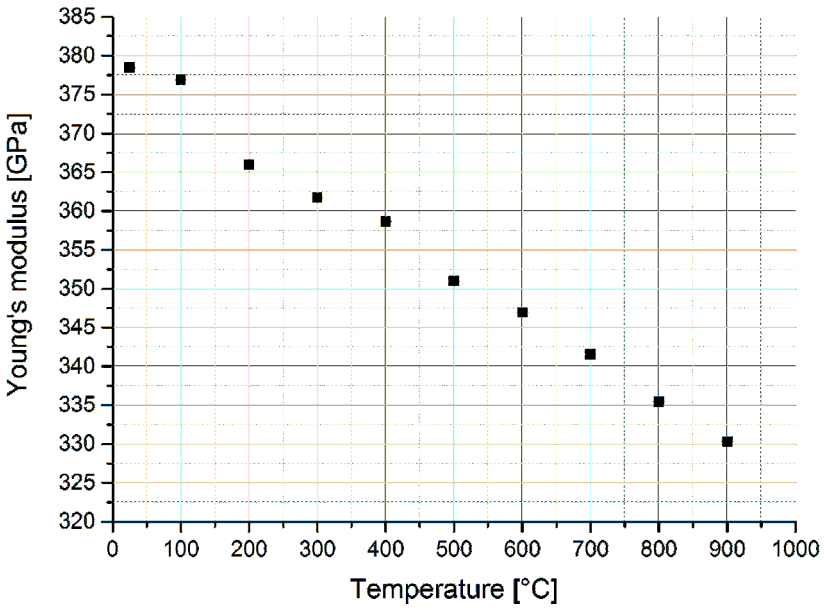


Figure 6.24: Young's modulus vs temperature for Al_2O_3.

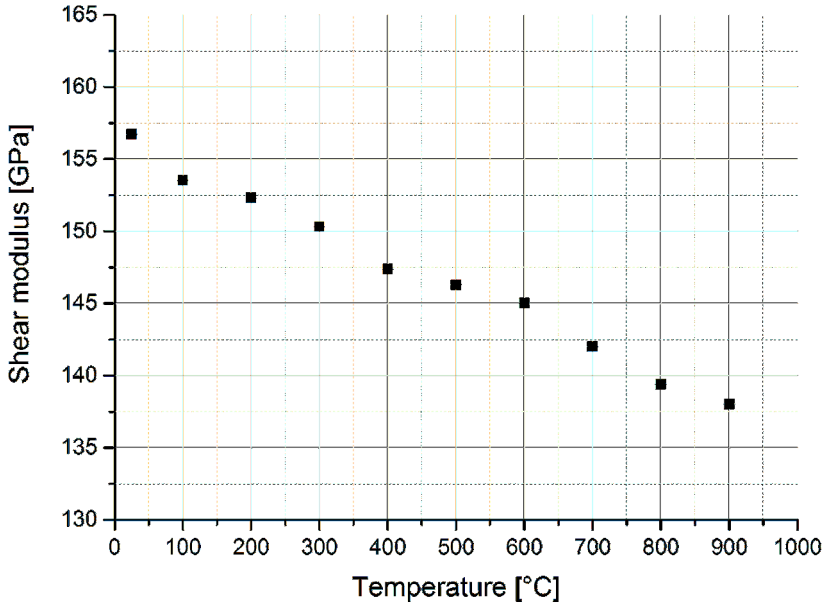


Figure 6.25: Shear modulus vs temperature for Al_2O_3.

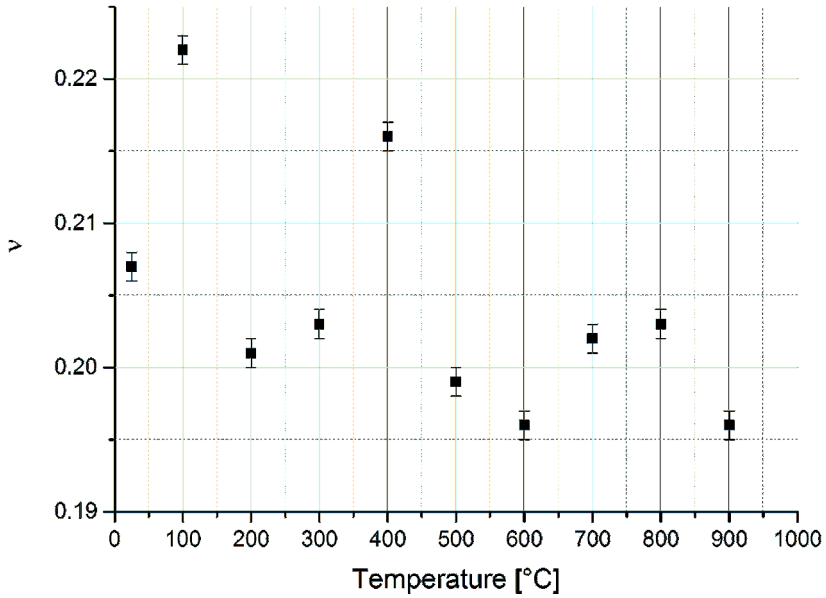


Figure 6.26: Poisson's ratio vs temperature for Al_2O_3.

6.3 ZrO_2

The following RUS spectra were recorded:

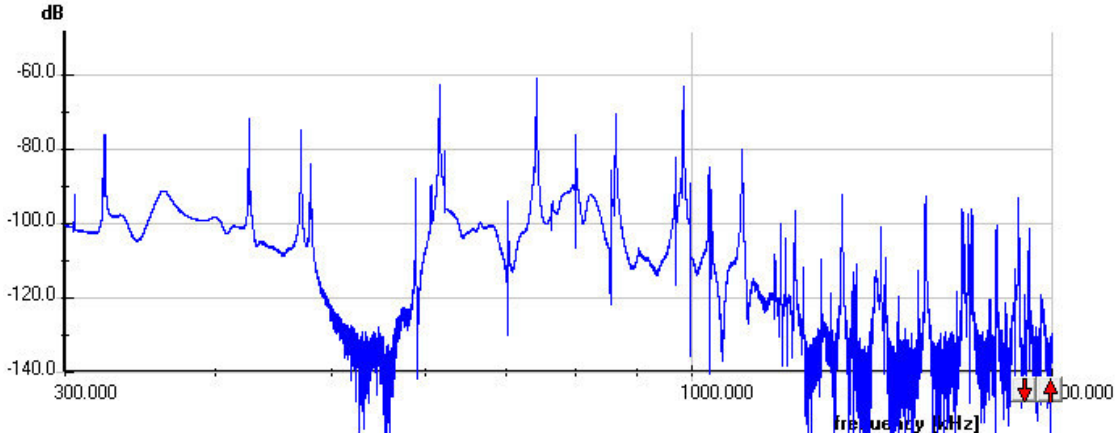


Figure 6.27: ZrO_2 sample measured at 25 °C. Frequency interval 260-2000 kHz.

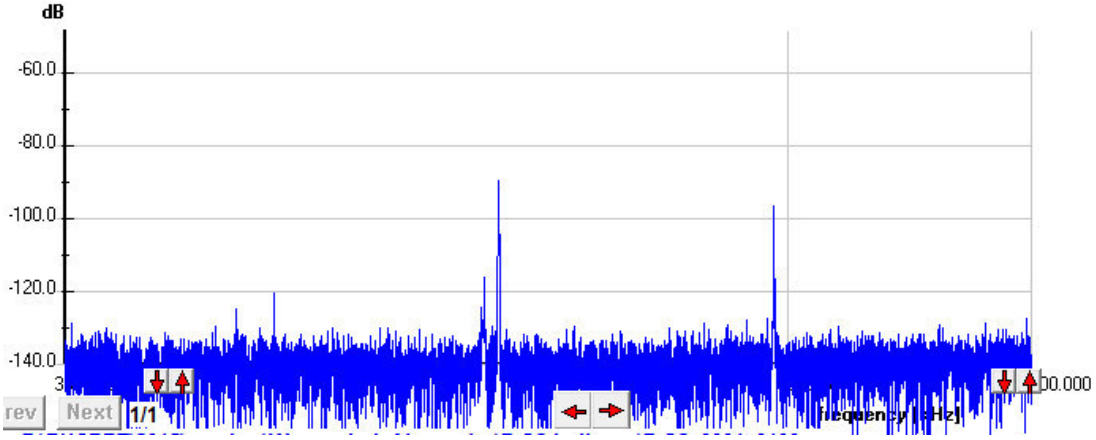


Figure 6.28: ZrO_2 sample measured at 100 °C. Frequency interval 300-1500 kHz.

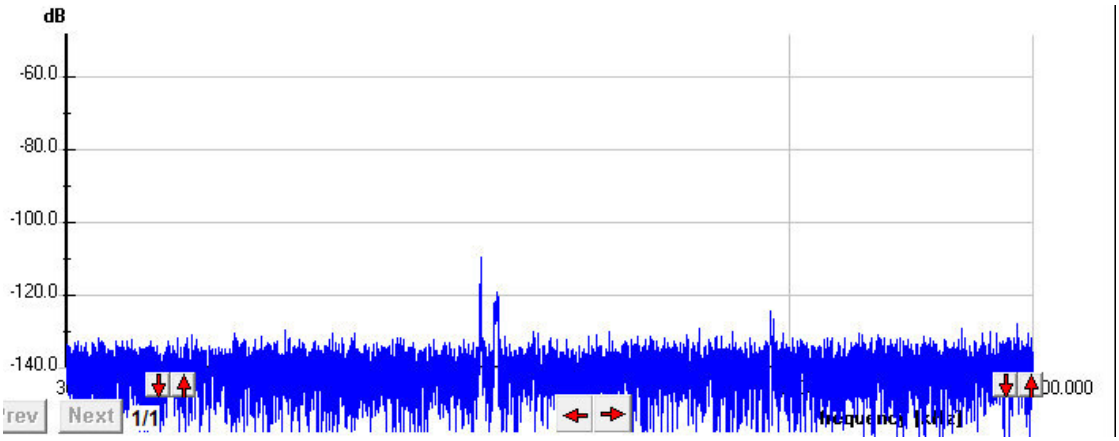


Figure 6.29: ZrO_2 sample measured at 200 °C. Frequency interval 300-1500 kHz.

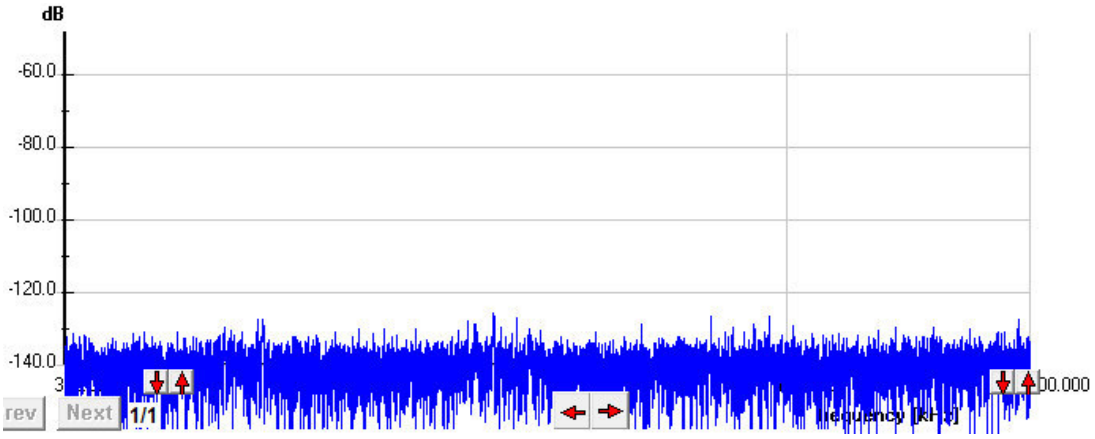


Figure 6.30: ZrO_2 sample measured at 300 °C. Frequency interval 300-1500 kHz.

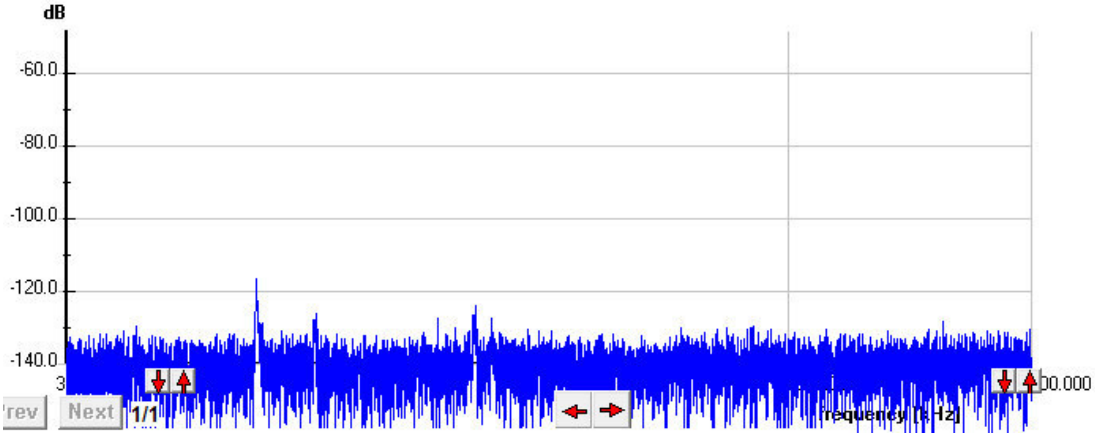


Figure 6.31: ZrO_2 sample measured at 400 °C. Frequency interval 300-1500 kHz.

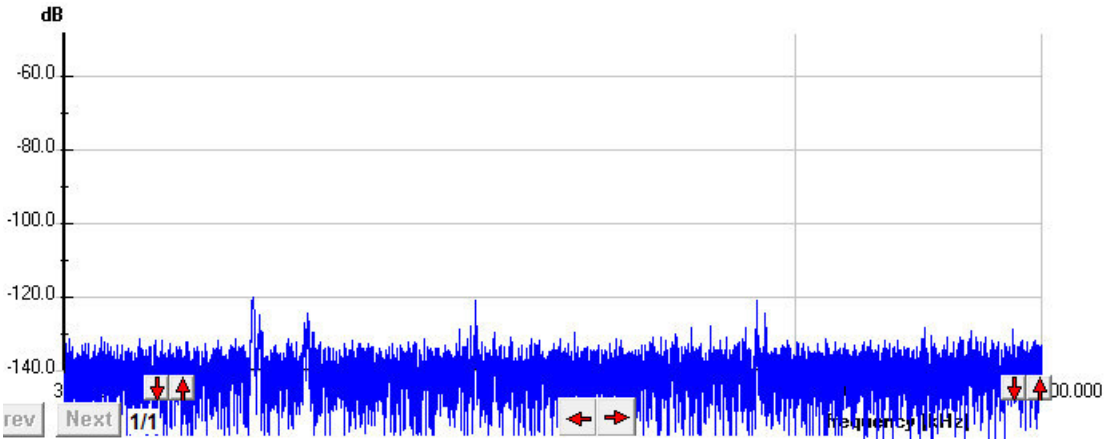


Figure 6.32: ZrO_2 sample measured at 500 °C. Frequency interval 300-1500 kHz.

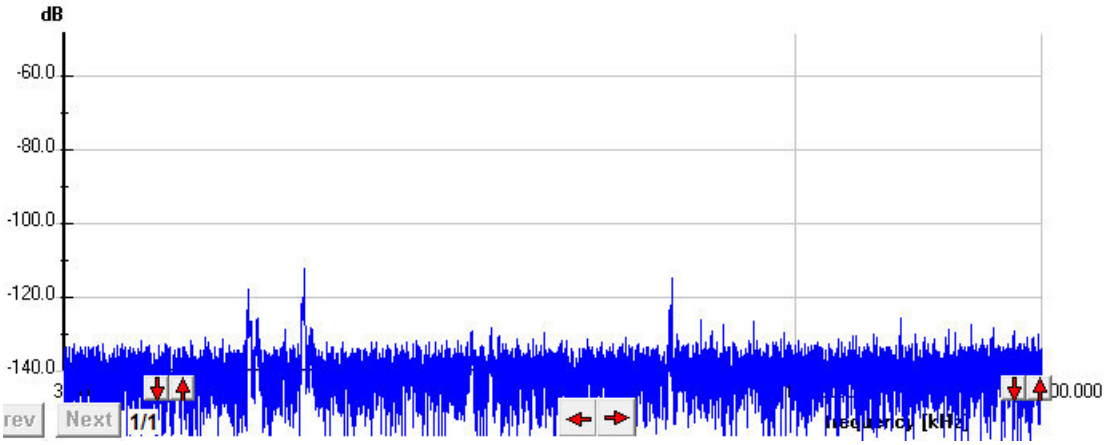


Figure 6.33: ZrO_2 sample measured at 600 °C. Frequency interval 300-1500 kHz.

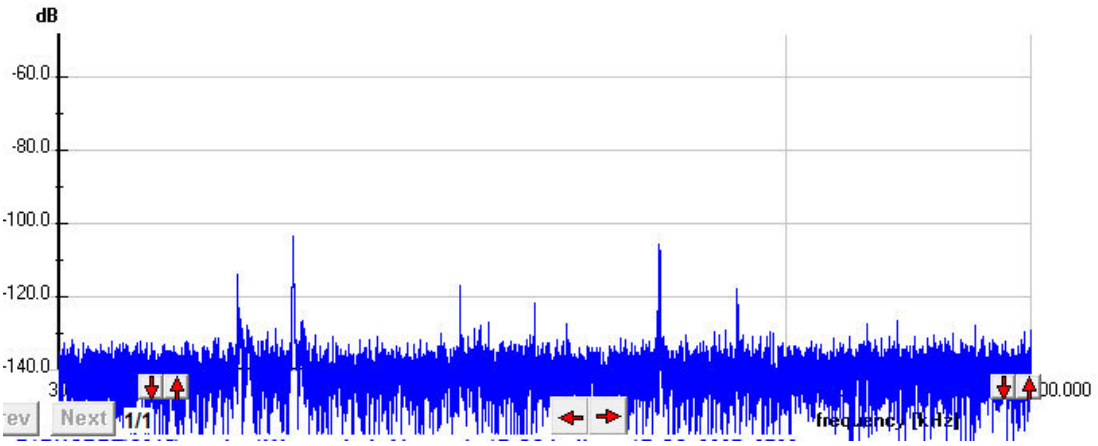


Figure 6.34: ZrO_2 sample measured at 700 °C. Frequency interval 300-1500 kHz.

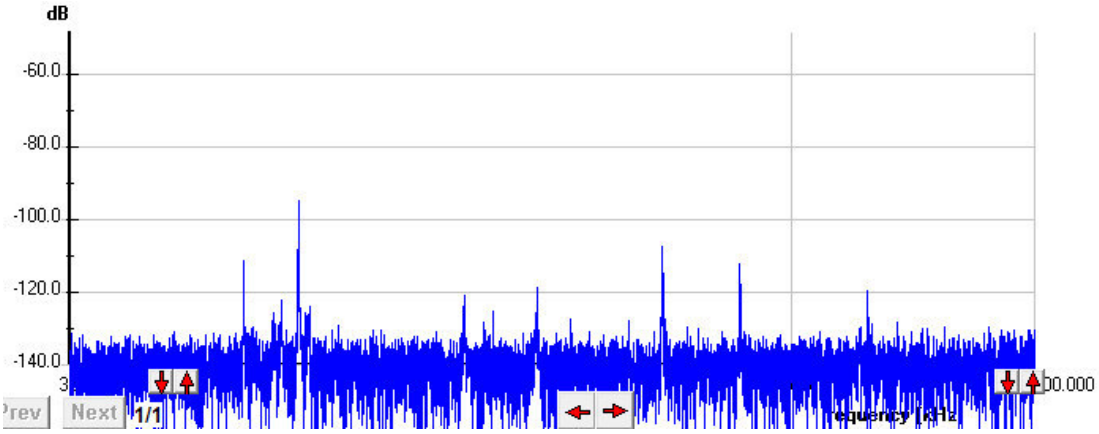


Figure 6.35: ZrO_2 sample measured at 800 °C. Frequency interval 300-1500 kHz.

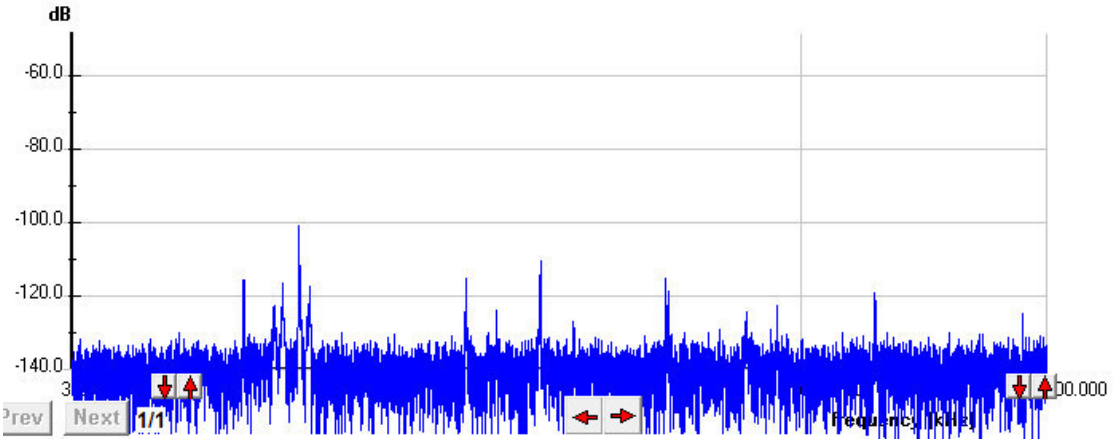


Figure 6.36: ZrO_2 sample measured at 900 °C. Frequency interval 300-1500 kHz.

Table 6.5: Resonant frequencies in [Hz] for the ZrO_2 sample.

25 °C	100 °C	200 °C	300 °C	400 °C	500 °C	600 °C	700 °C	800 °C	900 °C
305834	315789	314081	310127	305523	409525	405785	403227	400722	398196
323992	424795	397123	418355	411631	448228	445188	442144	439201	436289
427315	602763	421824	455979	448115	451254	450395	448293	447615	444606
472198	610777	458854	463016	455882	582112	474695	582951	578910	575004
481385	617837	597797	593094	582449	585418	573038	585258	654561	650068
588482	854698	600809	595561	585879	590635	581770	659007	691219	686797
606448	966261	683077	600078	704569	597088	585796	695971	753689	799916
616474	976580	842010	605035	726160	695276	587533	808521	805249	803028
622044		961214	678821		723388	661843	810743	807044	
703175		974168				813078			
742718						815760			
801270									
856837									
865178									
969655									
984951									
997263									

Table 6.6: ZrO_2: E, G and ν from 25 to 900 °C

T [°C]	E [GPa]	± [GPa]	ν	±	G [GPa]	± [GPa]
25	268.57	0.01	0.306	0.001	102.74	0.01
100	258.23	0.01	0.309	0.001	98.61	0.01
200	254.81	0.01	0.311	0.001	97.16	0.01
300	250.84	0.01	0.31	0.001	95.70	0.01
400	242.12	0.01	0.307	0.001	92.57	0.01
500	239.72	0.01	0.307	0.001	91.67	0.01
600	236.92	0.01	0.305	0.001	90.77	0.01
700	234.88	0.01	0.309	0.001	89.69	0.01
800	232.56	0.01	0.309	0.001	88.768	0.01
900	229.2	0.01	0.307	0.001	87.65	0.01

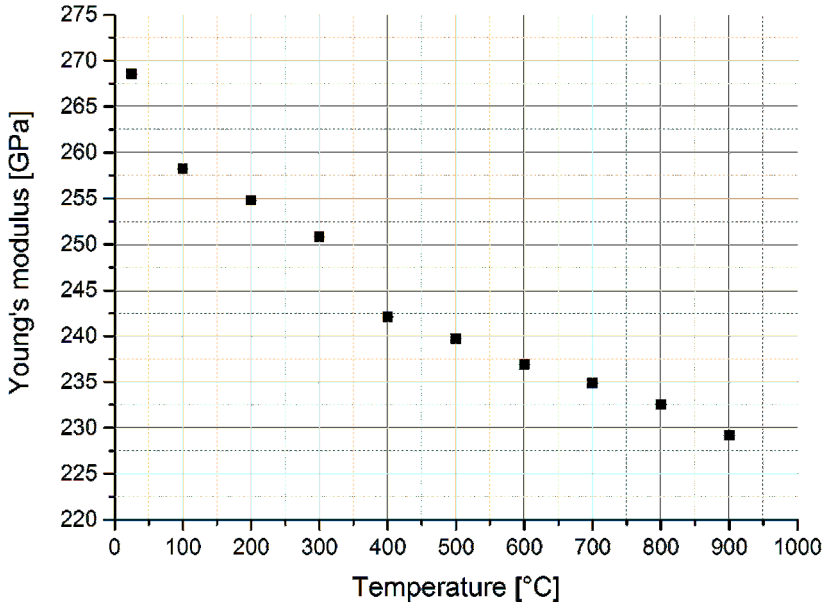


Figure 6.37: Young's modulus vs temperature for ZrO_2.

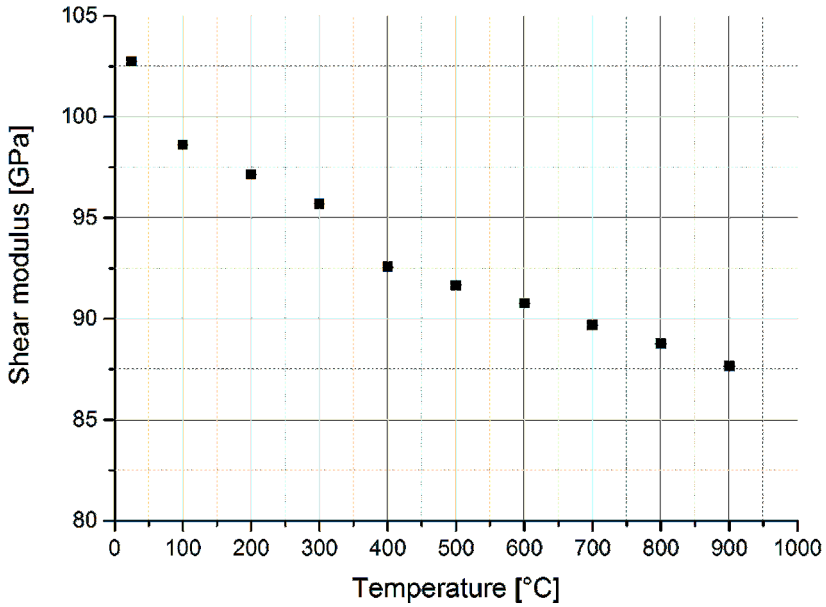


Figure 6.38: Shear modulus vs temperature for ZrO_2.

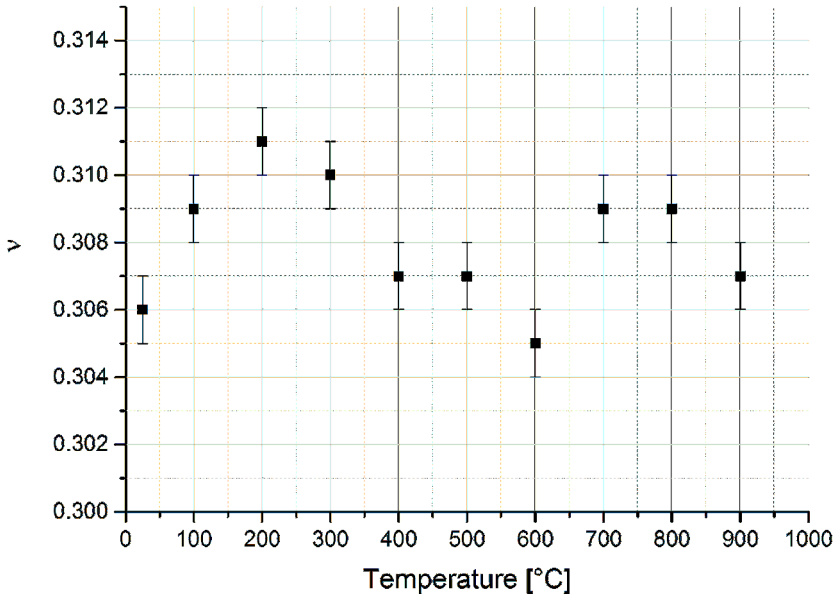


Figure 6.39: Poisson's ratio vs temperature for ZrO_2.

6.4 HfNiSn

The following RUS spectra were recorded:

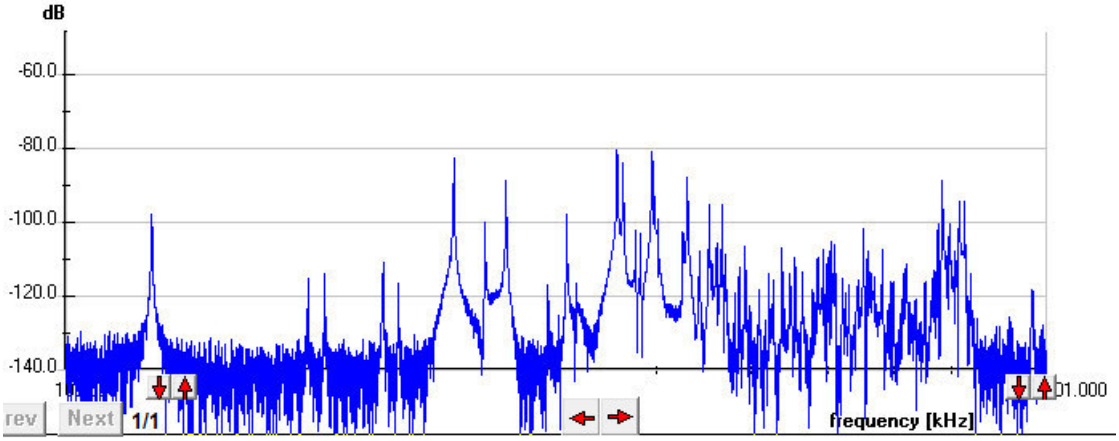


Figure 6.40: HfNiSn sample measured at 25 °C. Frequency interval 100-1001 kHz.

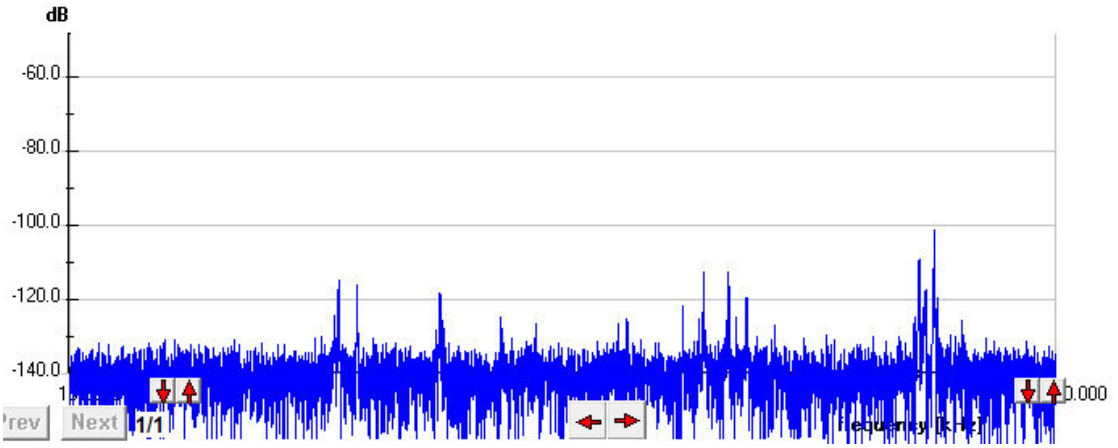


Figure 6.41: HfNiSn sample measured at 50 °C. Frequency interval 100-800 kHz.

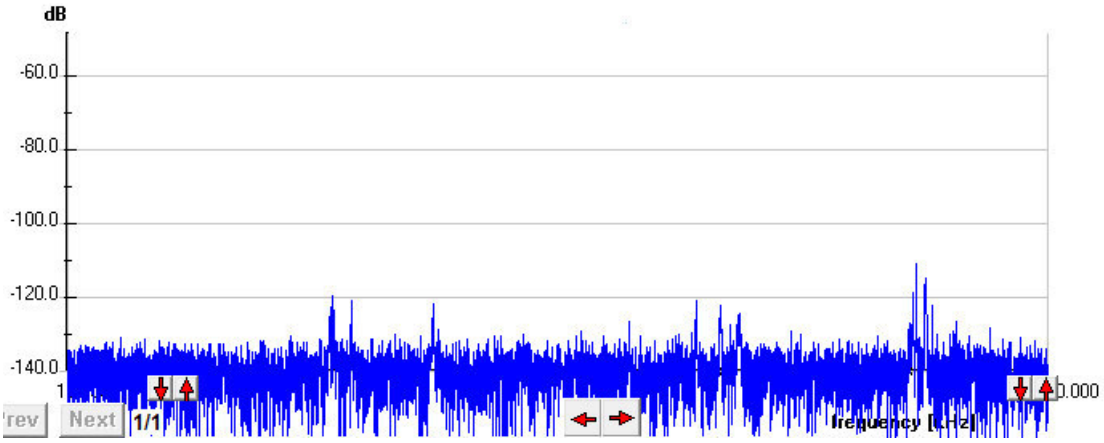


Figure 6.42: HfNiSn sample measured at 100 °C. Frequency interval 100-800 kHz.

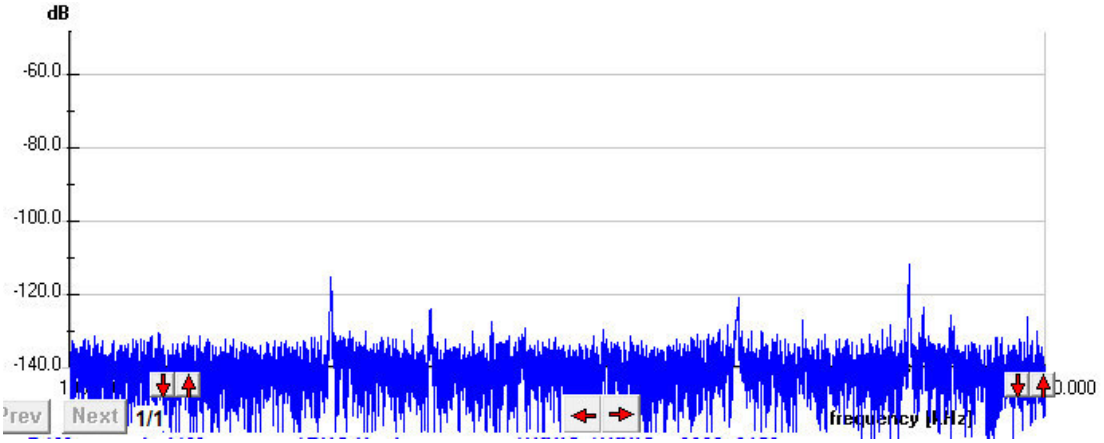


Figure 6.43: HfNiSn sample measured at 150 °C. Frequency interval 100-800 kHz.

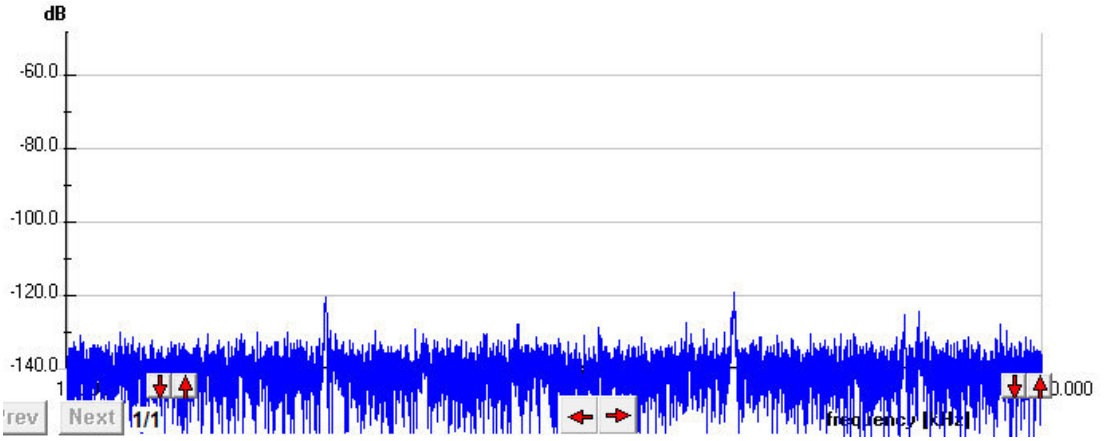


Figure 6.44: HfNiSn sample measured at 200 °C. Frequency interval 100-800 kHz.

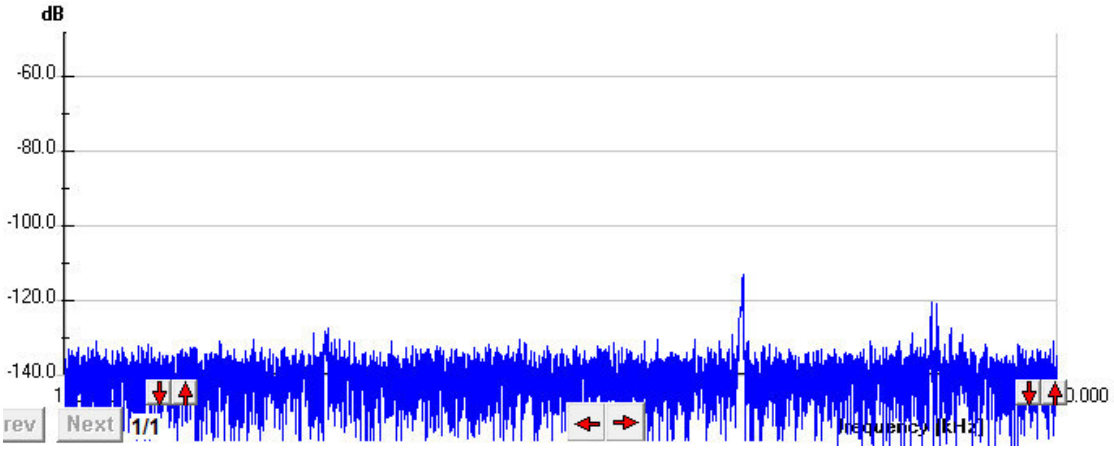


Figure 6.45: HfNiSn sample measured at 250 °C. Frequency interval 100-800 kHz.

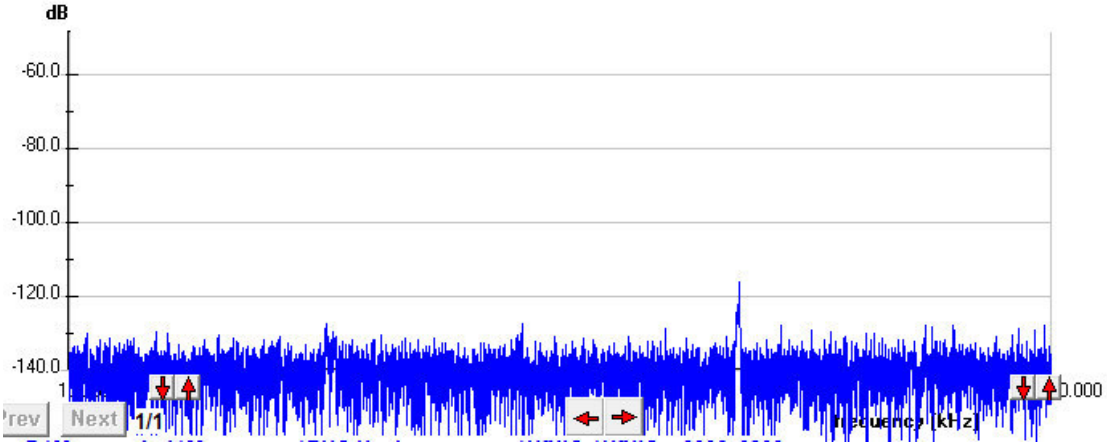


Figure 6.46: HfNiSn sample measured at 300 °C. Frequency interval 100-800 kHz.

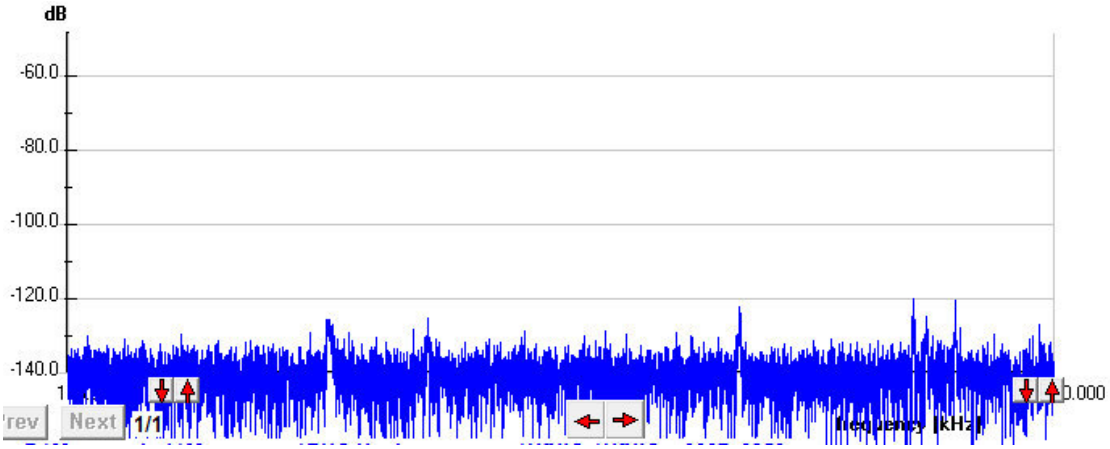


Figure 6.47: HfNiSn sample measured at 350 °C. Frequency interval 100-800 kHz.

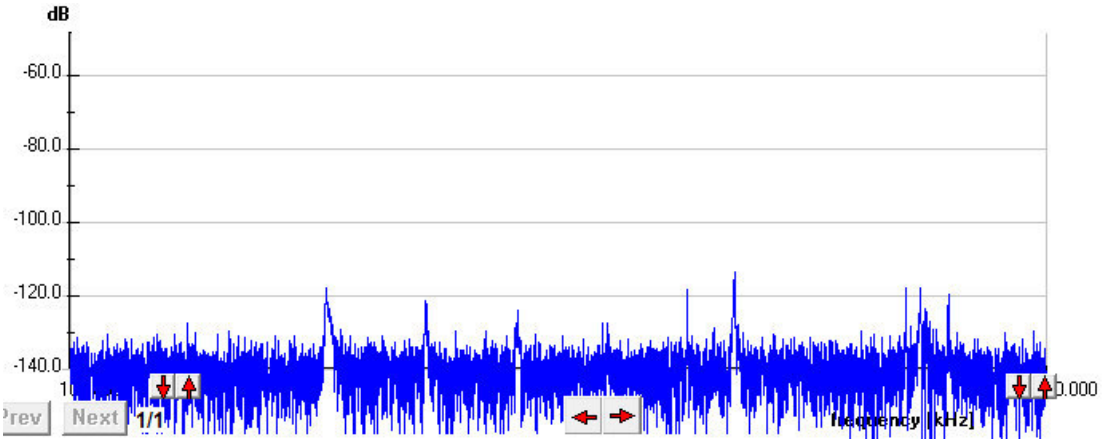


Figure 6.48: HfNiSn sample measured at 400 °C. Frequency interval 100-800 kHz.

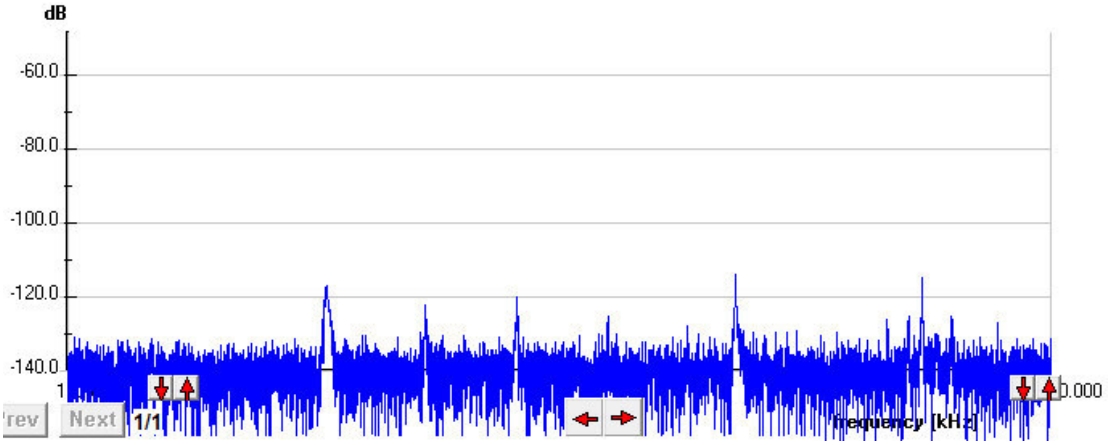


Figure 6.49: HfNiSn sample measured at 450 °C. Frequency interval 100-800 kHz.

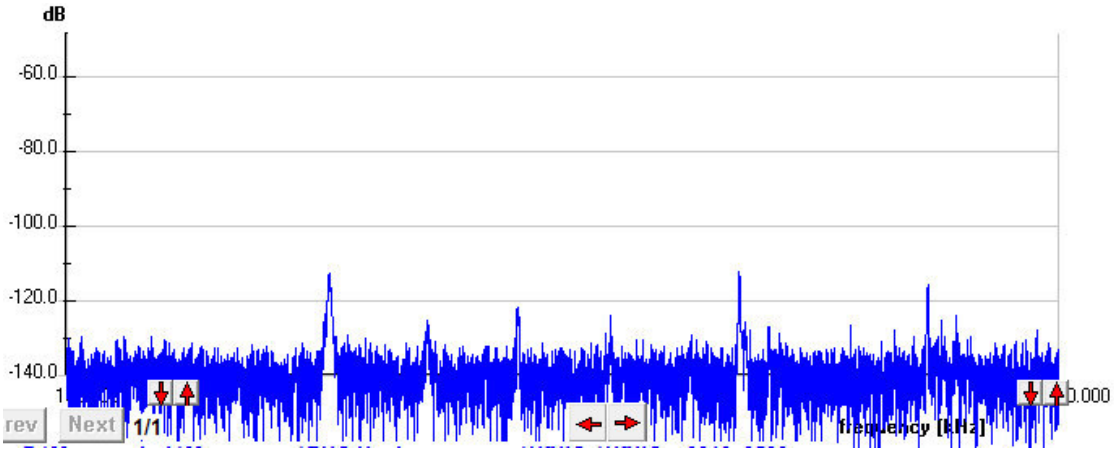


Figure 6.50: HfNiSn sample measured at 500 °C. Frequency interval 100-800 kHz.

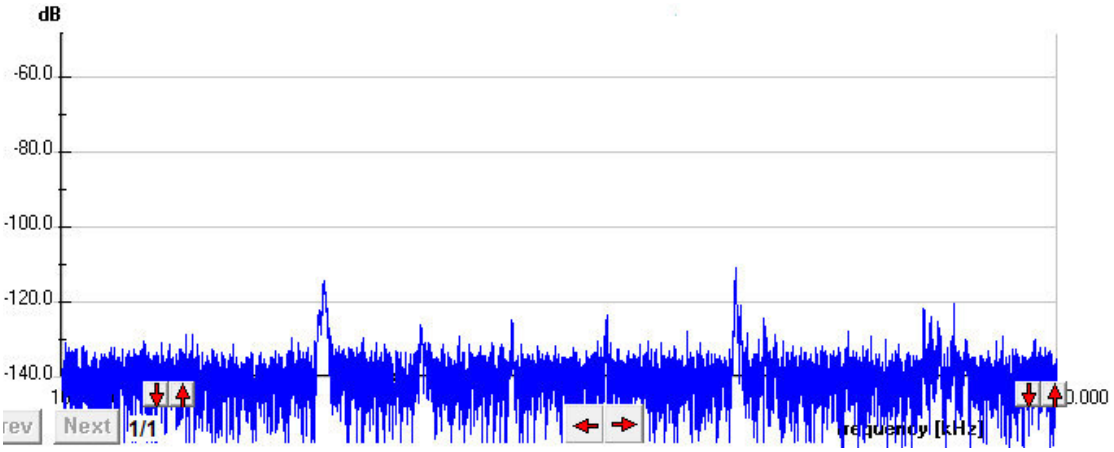


Figure 6.51: HfNiSn sample measured at 550 °C. Frequency interval 100-800 kHz.

Table 6.7: Resonant frequencies in [Hz] for the HfNiSn sample.

25 °C	50 °C	100 °C	150 °C	200 °C	250 °C
122285	176304	175542	168336	169929	168071
176530	183361	182474	170675	175379	174983
183554	218332	217159	174244	197982	198105
210511	248374	233738	207392	209966	204580
218279	317825	250965	236091	231620	227152
248695	324026	311822	245880	234346	235856
267696	364548	329095	305191	244689	243825
281232	373733	357634	311719	267484	263141
310273	376817	360666	375469	291141	290185
324309	381040	363491	399261	296484	305179
365182	392906	365728	415682	301748	337091
370210	401352	376096		310707	341838
381566	416994	379290		340728	344948
385919		399315			346203

Table 6.8: Resonant frequencies in [Hz] for the HfNiSn sample.

300 °C	350 °C	400 °C	450 °C	500 °C	550 °C
120319	112614	112266	116350	112481	172781
169760	166540	166498	158905	173308	211764
172515	170327	172346	172615	194671	229659
193331	195702	194151	191240	213092	256224
209296	207054	203711	201082	227801	310469
228258	231215	227071	221095	257304	312228
234622	241875	241993	230794	282014	349814
240983	261788	261536	258586	290571	369191
261032	285007	284944	280224	294485	369450
289909	296645	298197	290850	309162	408845
297079	304742	301643	295114	330254	413047
302941	334308	327711	336647	334580	418563
339946	339195	335788	343413		
343854	340991	338617	359964		
345524		344398			
349561		354041			
		357284			

Table 6.9: HfNiSn: E, G and ν from 25 to 550 °C

T [°C]	E [GPa]	± [GPa]	ν	±	G [GPa]	± [GPa]
25	137.36	0.18	0.221	0.005	56.23	0.27
50	134.74	0.40	0.212	0.009	55.55	0.48
100	131.18	0.11	0.195	0.002	54.85	0.14
150	127.18	0.11	0.238	0.002	51.36	0.11
200	125.34	0.32	0.237	0.001	50.65	0.13
250	123.90	0.15	0.251	0.003	49.51	0.14
300	121.14	0.10	0.220	0.003	49.62	0.14
350	120.83	0.18	0.240	0.003	48.68	0.14
400	119.80	0.12	0.242	0.004	48.20	0.18
450	117.47	0.08	0.228	0.004	47.81	0.17
500	116.19	0.08	0.224	0.005	47.43	0.20
550	115.74	0.15	0.238	0.006	46.74	0.25

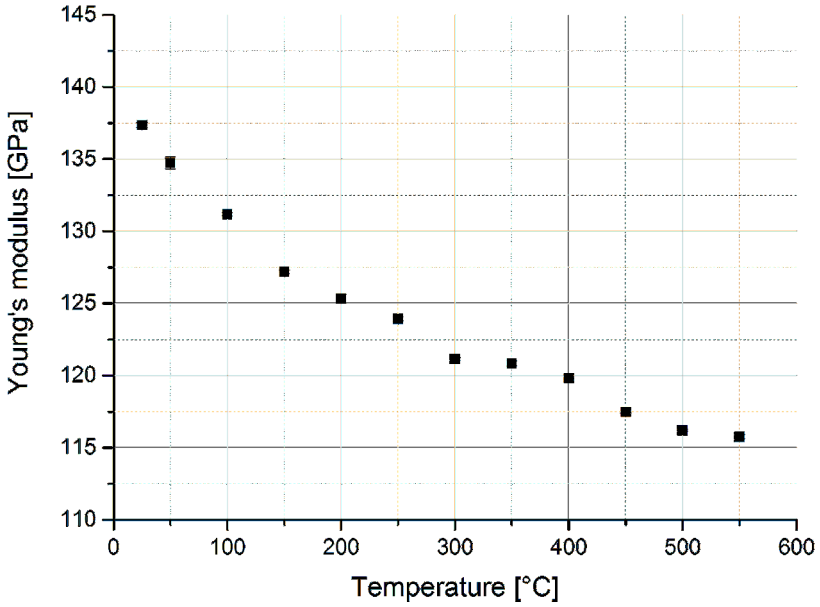


Figure 6.52: Young's modulus vs temperature for HfNiSn.

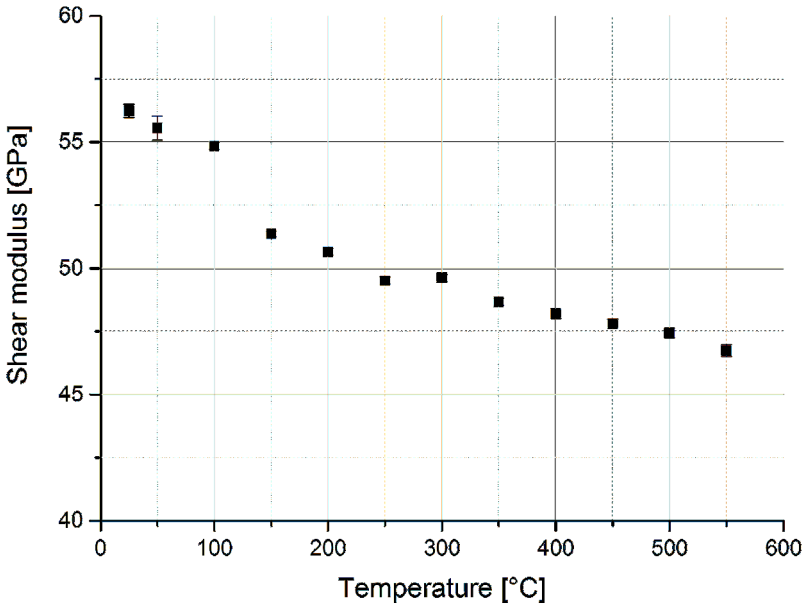


Figure 6.53: Shear modulus vs temperature for HfNiSn.

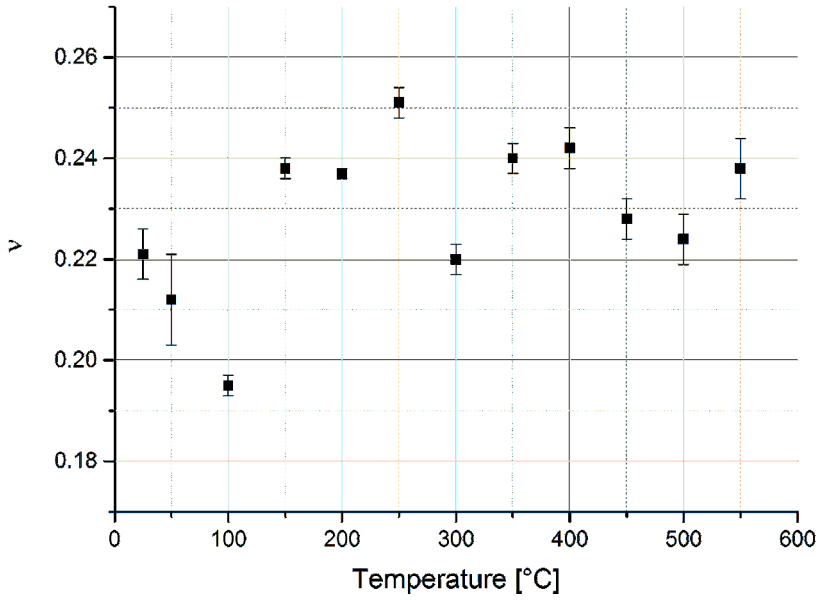


Figure 6.54: Poisson's ratio vs temperature for HfNiSn.

6.5 TiNiSn

The following RUS spectra were recorded:

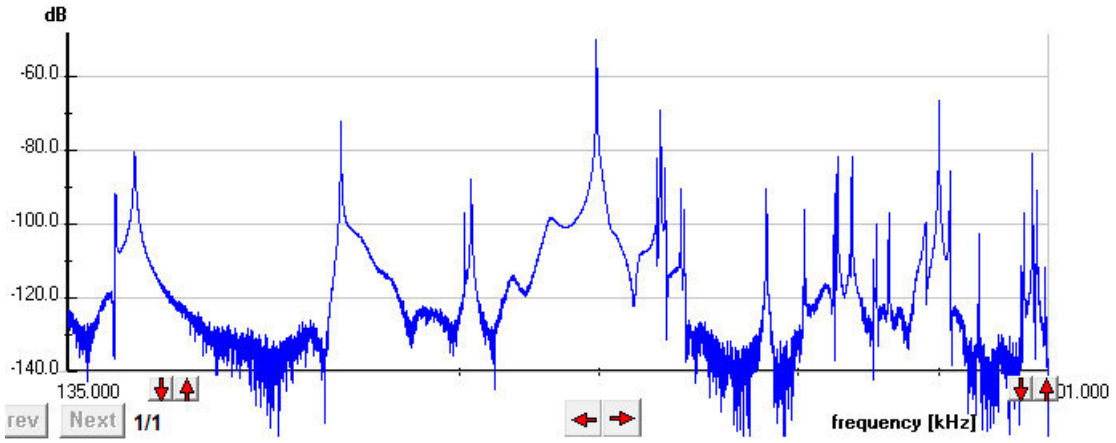


Figure 6.55: TiNiSn sample measured at 25 °C. Frequency interval 135-1001 kHz.

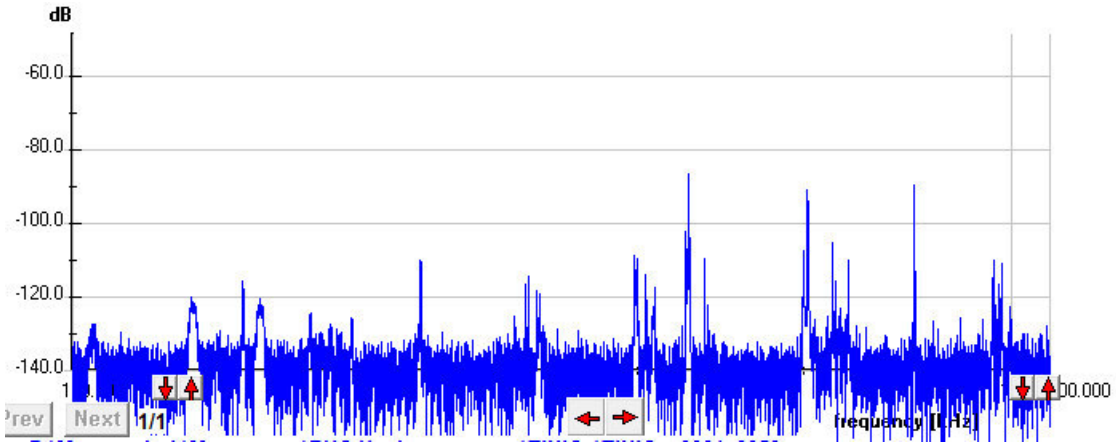


Figure 6.56: TiNiSn sample measured at 50 °C. Frequency interval 100-1100 kHz.

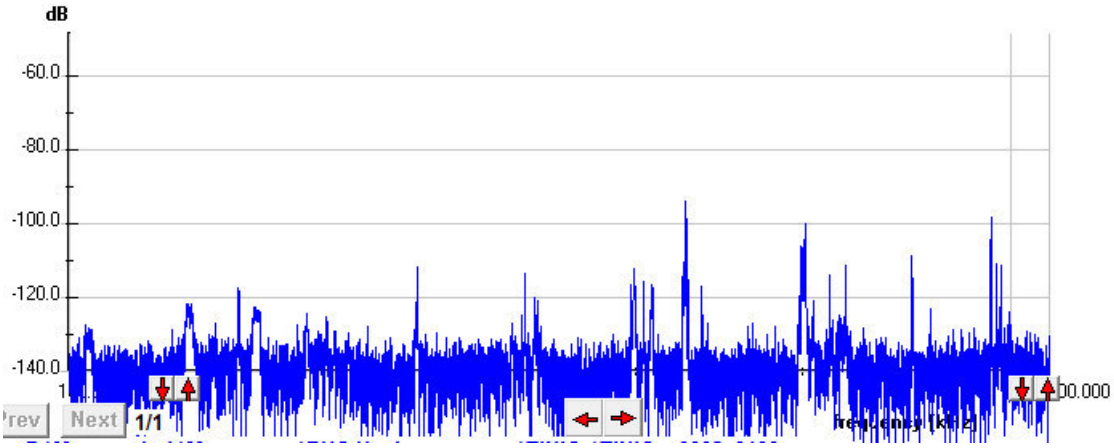


Figure 6.57: TiNiSn sample measured at 100 °C. Frequency interval 100-1100 kHz.

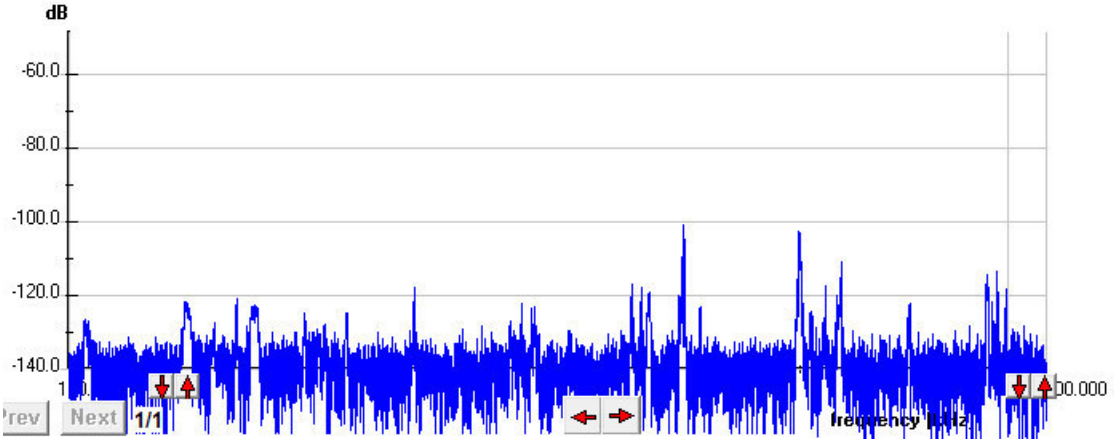


Figure 6.58: TiNiSn sample measured at 150 °C. Frequency interval 100-1100 kHz.

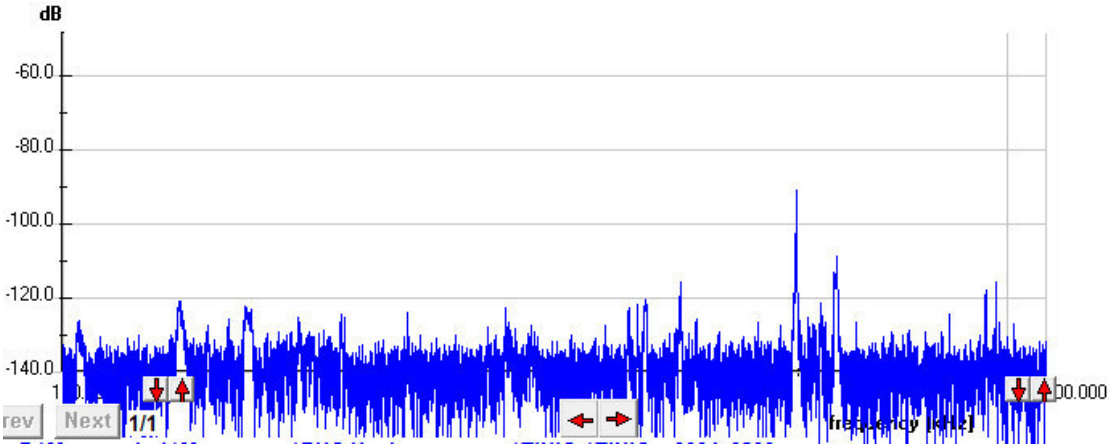


Figure 6.59: TiNiSn sample measured at 200 °C. Frequency interval 100-1100 kHz.

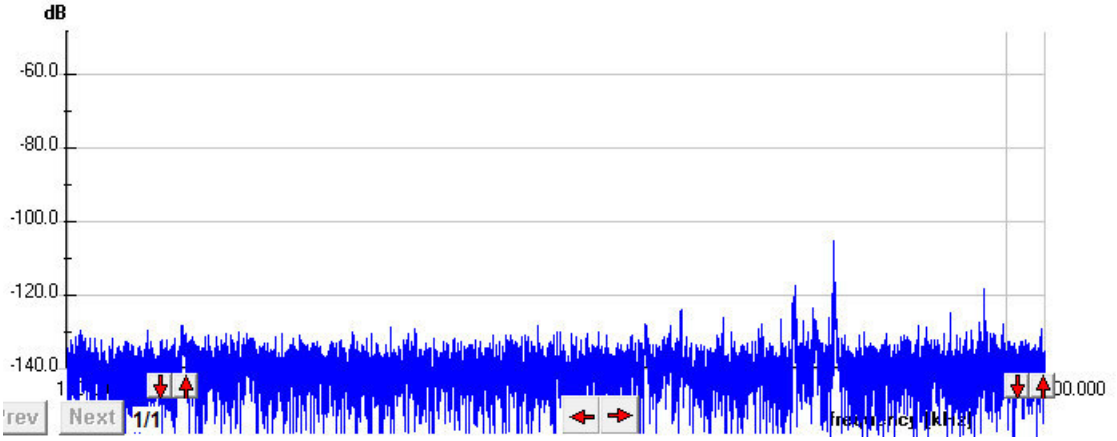


Figure 6.60: TiNiSn sample measured at 250 °C. Frequency interval 100-1100 kHz.

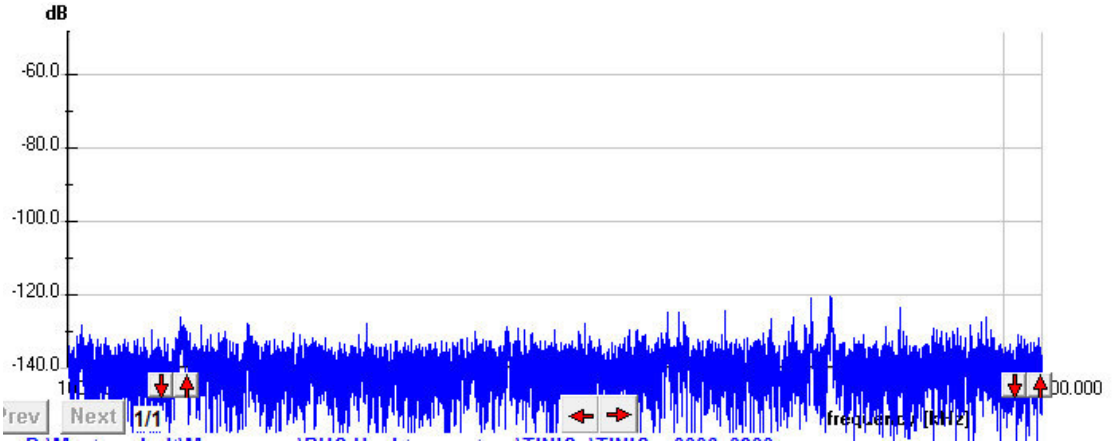


Figure 6.61: TiNiSn sample measured at 300 °C. Frequency interval 100-1100 kHz.

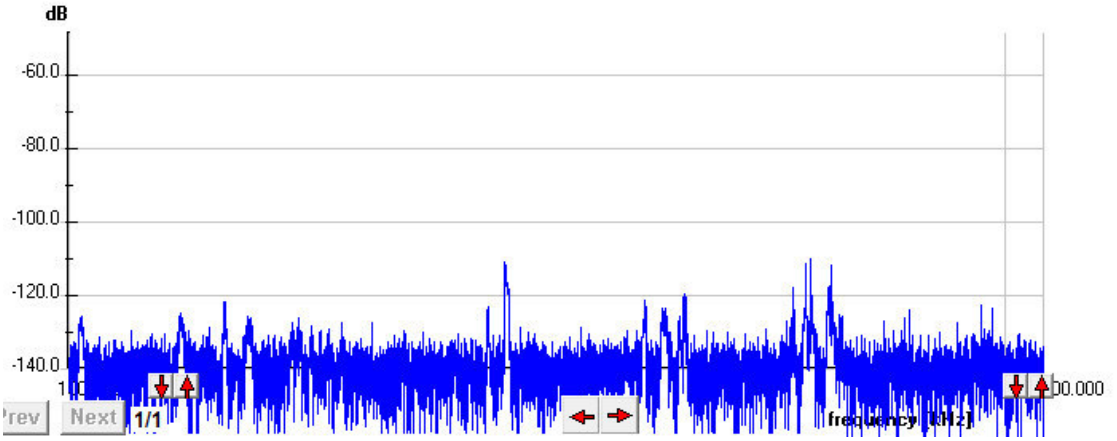


Figure 6.62: TiNiSn sample measured at 350 °C. Frequency interval 100-1100 kHz.

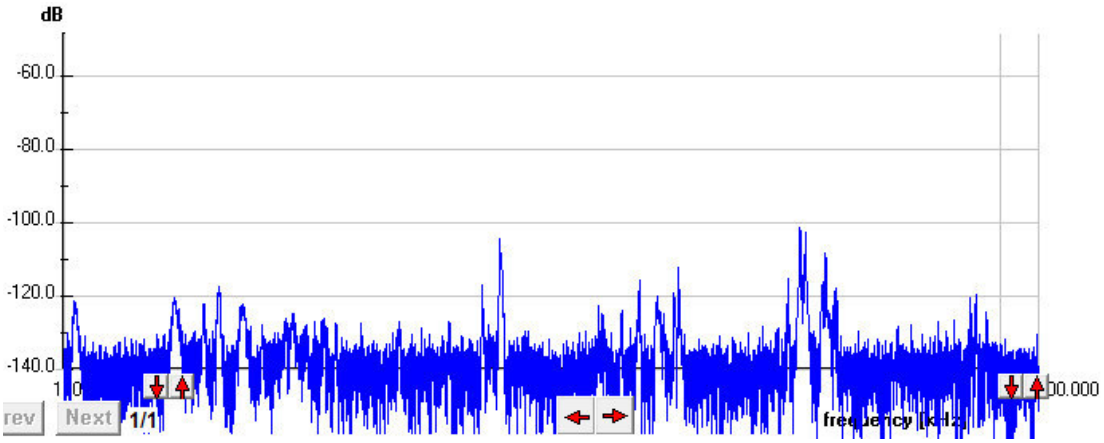


Figure 6.63: TiNiSn sample measured at 400 °C. Frequency interval 100-1100 kHz.

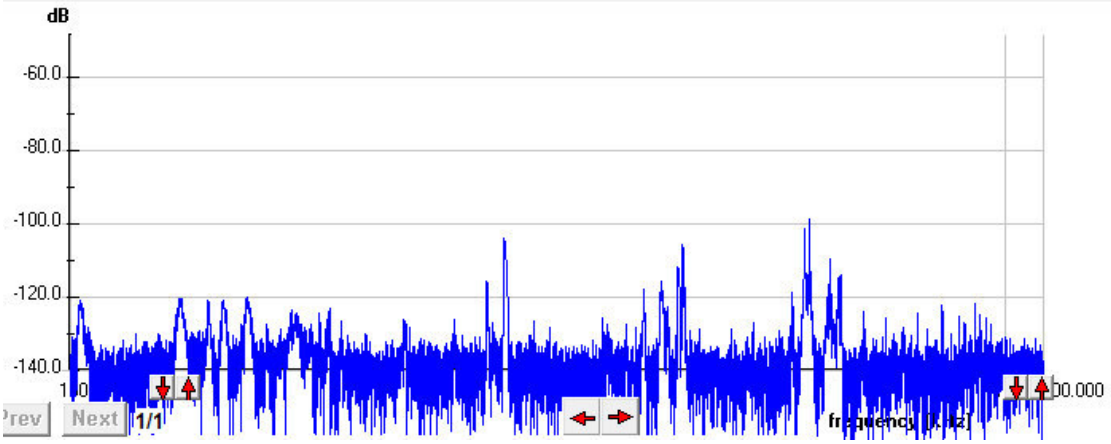


Figure 6.64: TiNiSn sample measured at 450 °C. Frequency interval 100-1100 kHz.

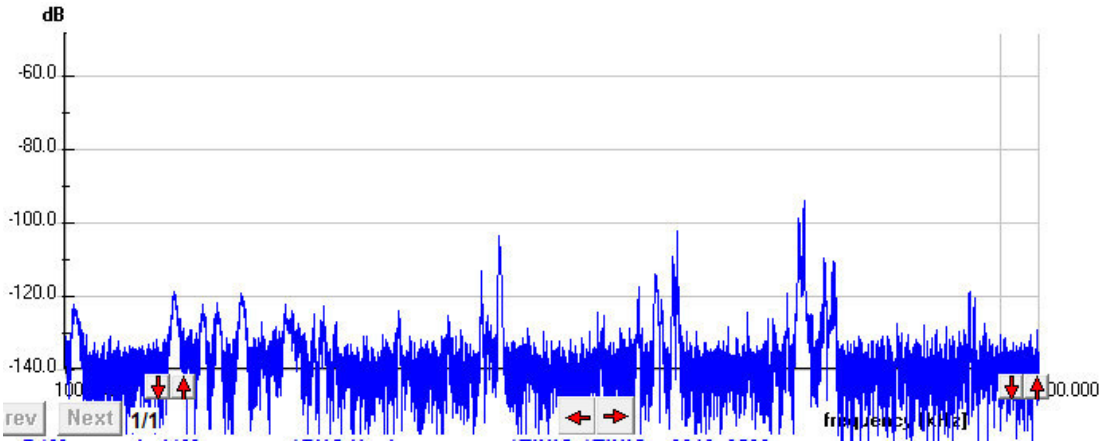


Figure 6.65: TiNiSn sample measured at 500 °C. Frequency interval 100-1100 kHz.

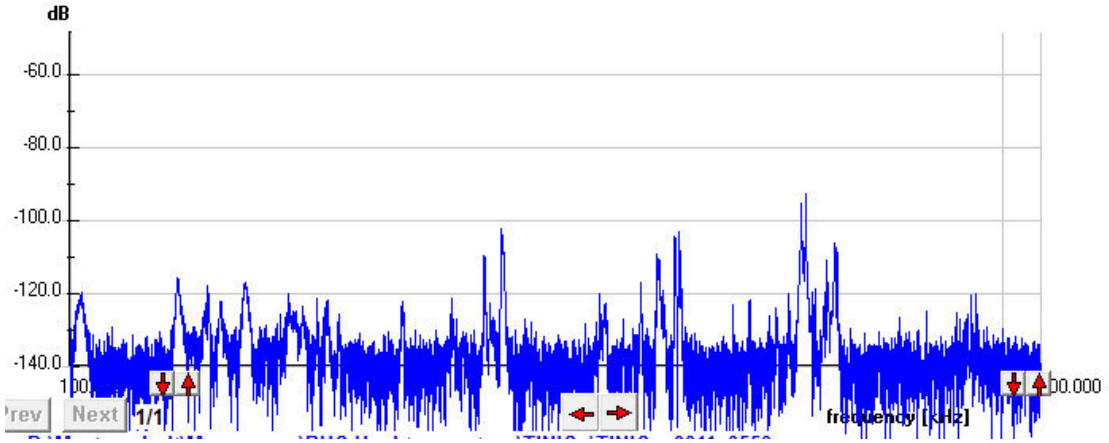


Figure 6.66: TiNiSn sample measured at 550 °C. Frequency interval 100-1100 kHz.

Table 6.10: Resonant frequencies in [Hz] for the TiNiSn sample.

25 °C	50 °C	100 °C	150 °C	200 °C	250 °C
148729	151874	151280	150760	149875	229544
154596	234796	234027	233114	231828	450356
235724	305760	304638	303172	301478	499446
303606	396380	394920	406878	389246	596862
307727	450412	448879	452097	451206	647599
397555	453662	452112	470289	467878	655430
450128	606880	604992	604095	544665	948274
452827	645561	667614	657813	598026	
453511	669877	787736	664567	656557	
457546	788737	953864	717217	660878	
472551	826695	967027	956893	692094	
562752	957077		963247	868597	
608307	961300		965031	956196	
646410	970488			966748	
650456	977842				
668850					
669892					
700874					
705380					
722568					

Table 6.11: Resonant frequencies in [Hz] for the TiNiSn sample.

300 °C	350 °C	400 °C	450 °C	500 °C	550 °C
146907	146592	146149	145632	225982	142900
229016	292485	224330	218495	297784	219363
306855	434654	298770	301344	446077	300071
437398	448947	437025	435925	465059	375488
449632	594675	538403	444093	536290	427877
595941	647961	593561	461013	591213	436177
652212	650868	649528	537624	640425	457508
654168	944368	700132	592403	644291	590054
946152		859143	645351	930334	629109
948545		934371	806007	932728	642849
958913		937193	855296	938580	687301
		942402	929149		809027
			935697		828419
			940293		916756
					917545
					925719
					926780

Table 6.12: TiNiSn: E, G and ν from 25 to 550 °C

T [°C]	E [GPa]	± [GPa]	ν	±	G [GPa]	± [GPa]
25	171.6	2.3	0.271	0.003	67.54	0.89
50	171.6	2.21	0.266	0.004	67.57	0.90
100	170.57	2.3	0.256	0.007	67.92	0.99
150	170.24	1.6	0.247	0.007	68.28	0.74
200	168.06	1.96	0.265	0.001	67.84	0.79
250	166.8	2.12	0.248	0.002	66.82	0.85
300	165.26	2.00	0.241	0.013	66.56	0.83
350	162.73	2.24	0.23	0.003	66.12	0.92
400	162	1.89	0.243	0.002	65.14	0.76
450	160.59	2.01	0.25	0.002	64.25	0.80
500	157.91	1.99	0.26	0.002	62.60	0.79
550	154.87	2.11	0.227	0.002	61.81	1.03

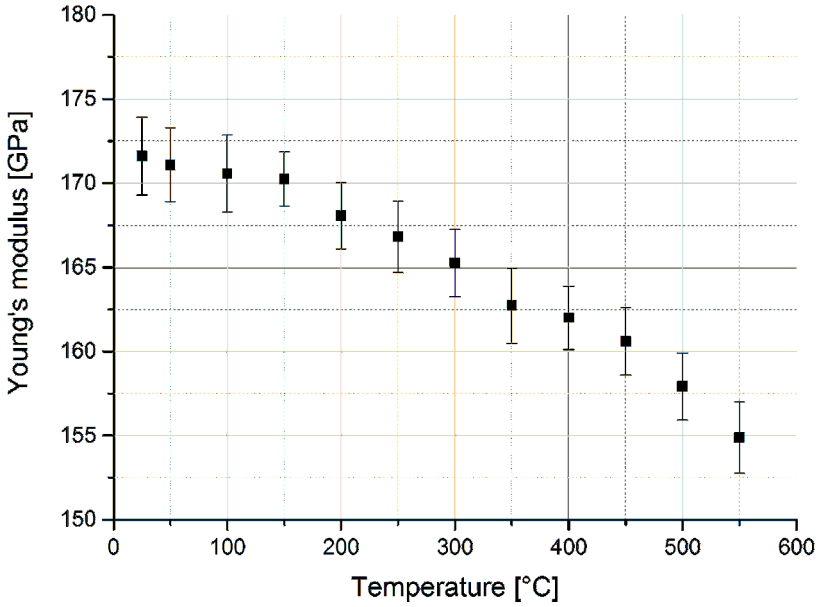


Figure 6.67: Young's modulus vs temperature for TiNiSn.

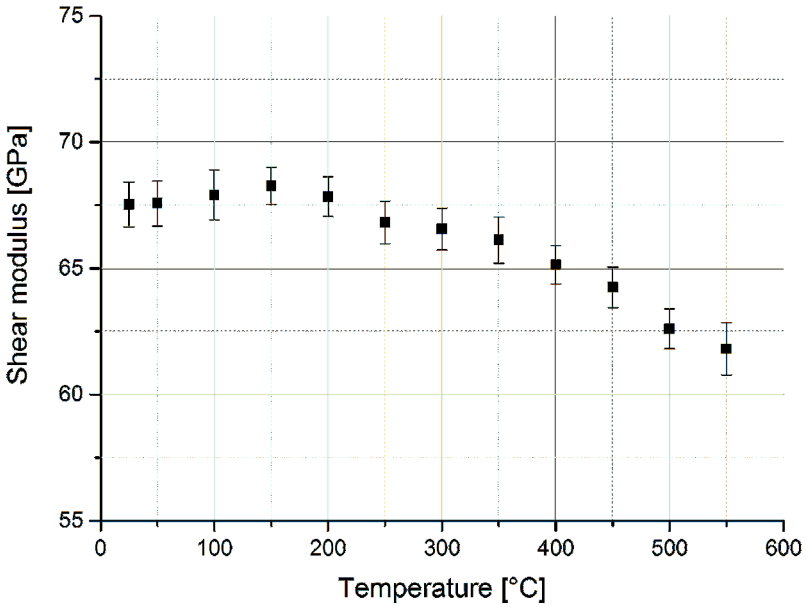


Figure 6.68: Shear modulus vs temperature for TiNiSn.

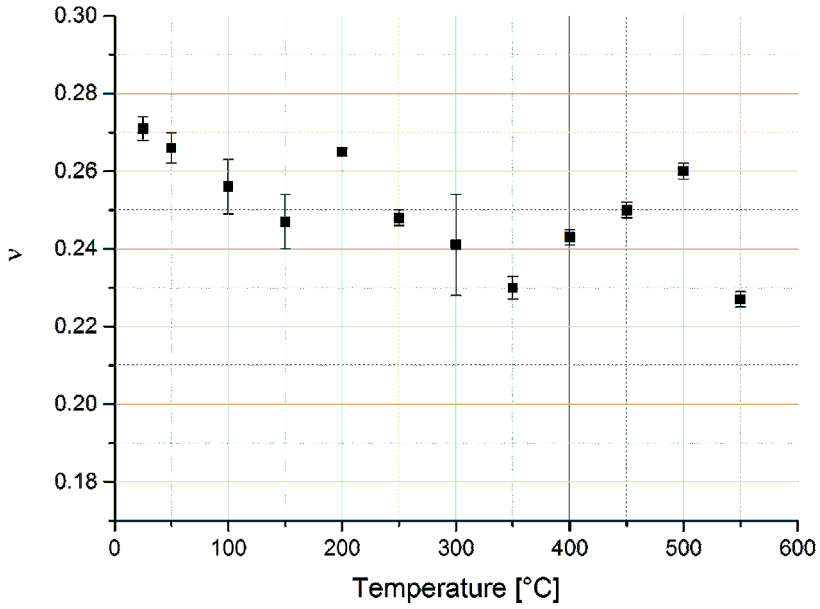


Figure 6.69: Poisson's ratio vs temperature for TiNiSn.

6.6 ZrNiSn

The following RUS spectra were recorded:

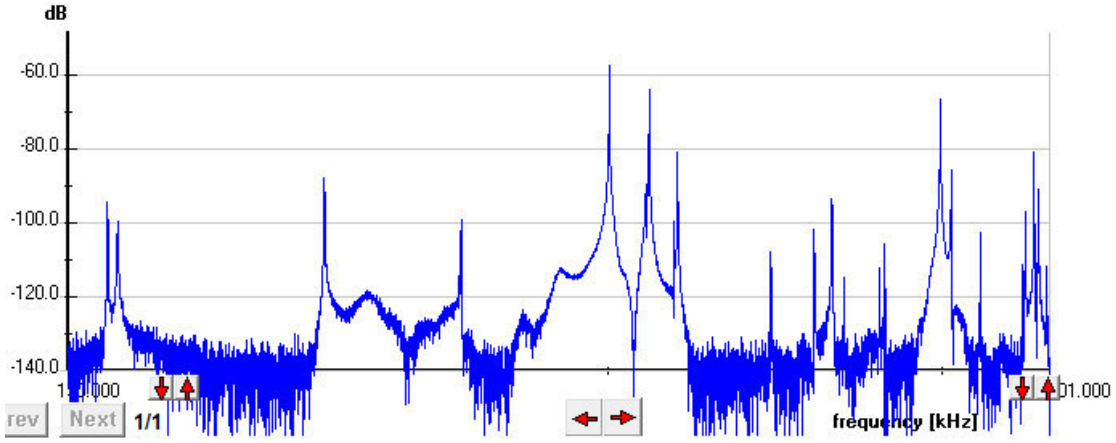


Figure 6.70: ZrNiSn sample measured at 25 °C. Frequency interval 130-1001 kHz.

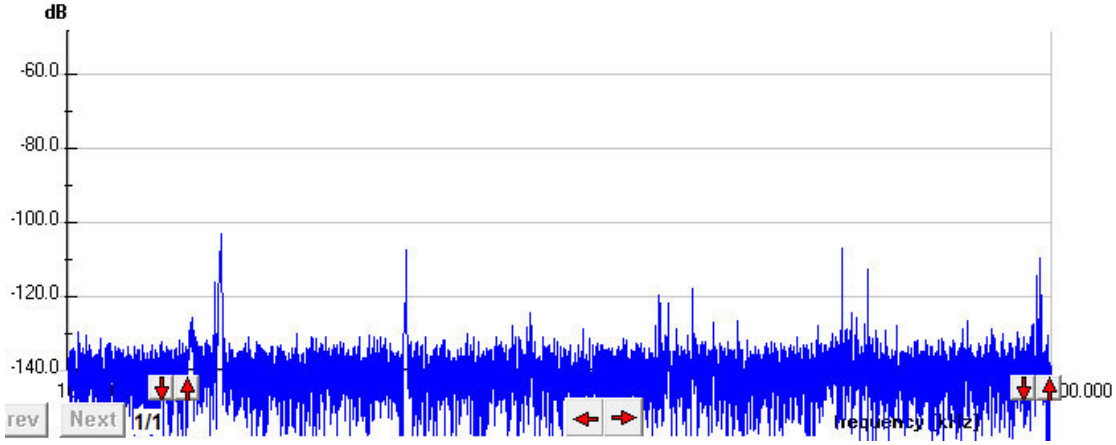


Figure 6.71: ZrNiSn sample measured at 50 °C. Frequency interval 100-1000 kHz.

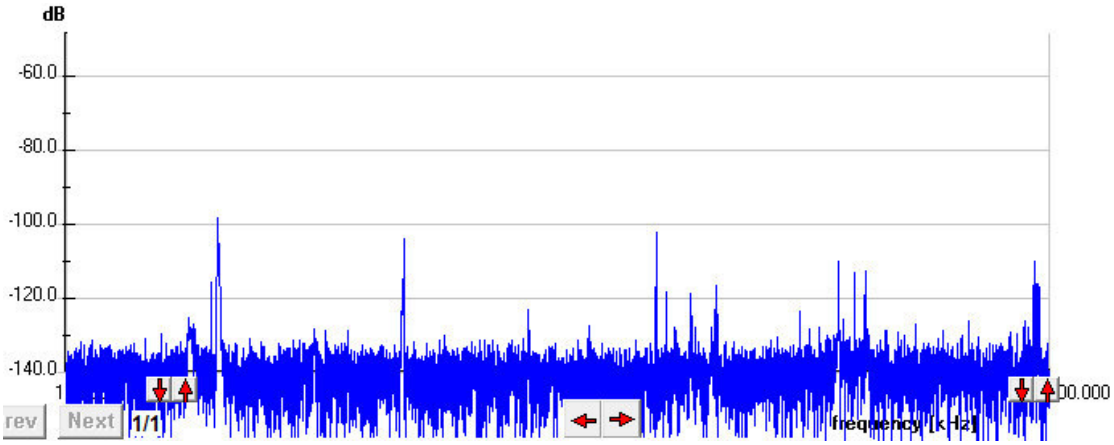


Figure 6.72: ZrNiSn sample measured at 100 °C. Frequency interval 100-1001 kHz.

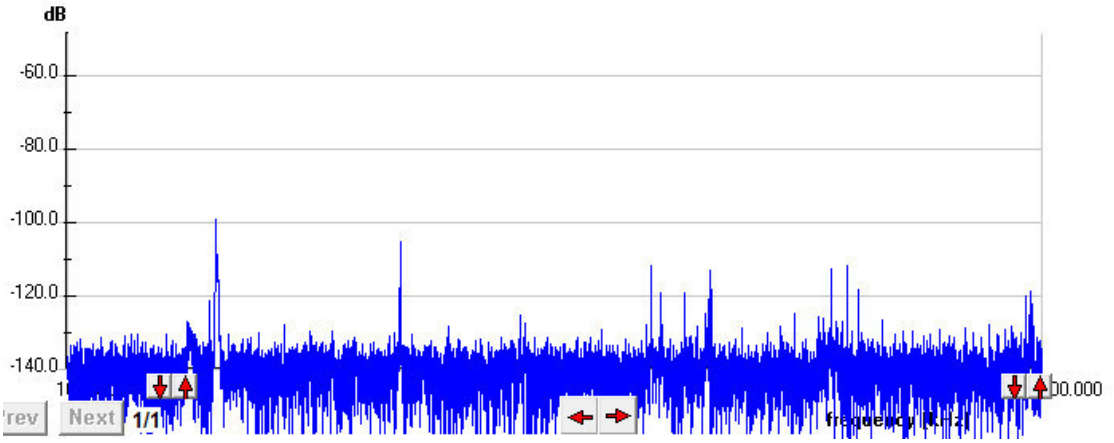


Figure 6.73: ZrNiSn sample measured at 150 °C. Frequency interval 100-1001 kHz.

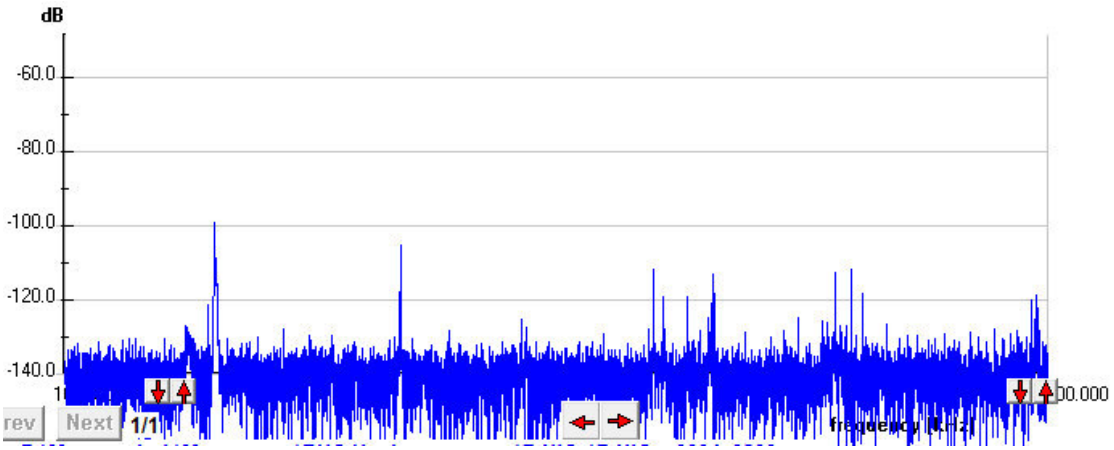


Figure 6.74: ZrNiSn sample measured at 200 °C. Frequency interval 100-1001 kHz.

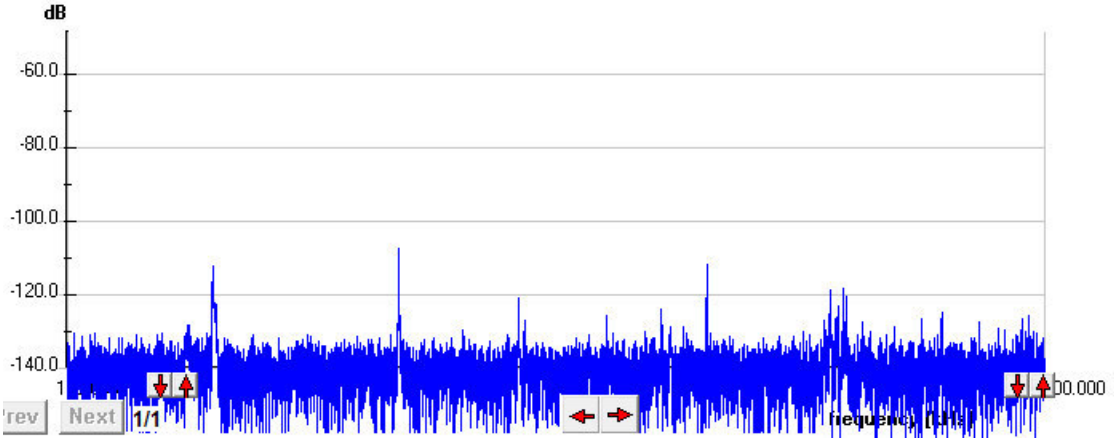


Figure 6.75: ZrNiSn sample measured at 250 °C. Frequency interval 100-1001 kHz.

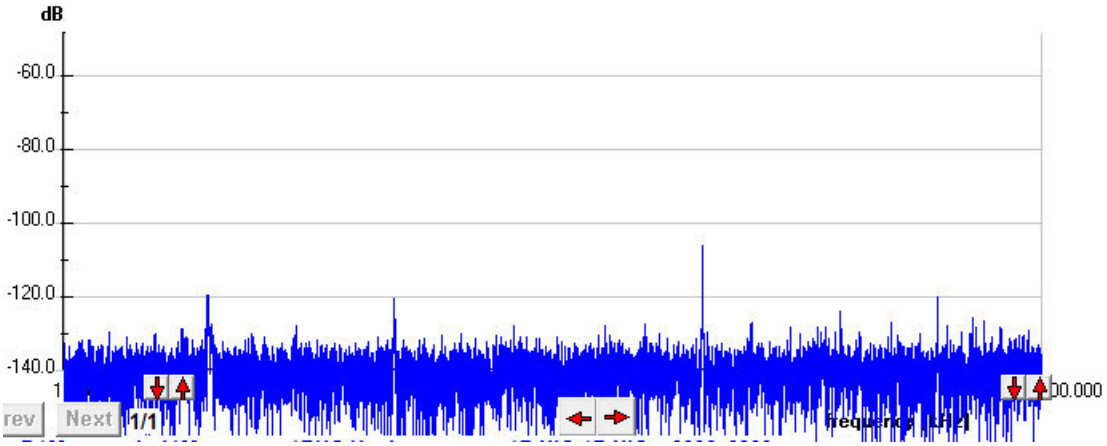


Figure 6.76: ZrNiSn sample measured at 300 °C. Frequency interval 100-1001 kHz.

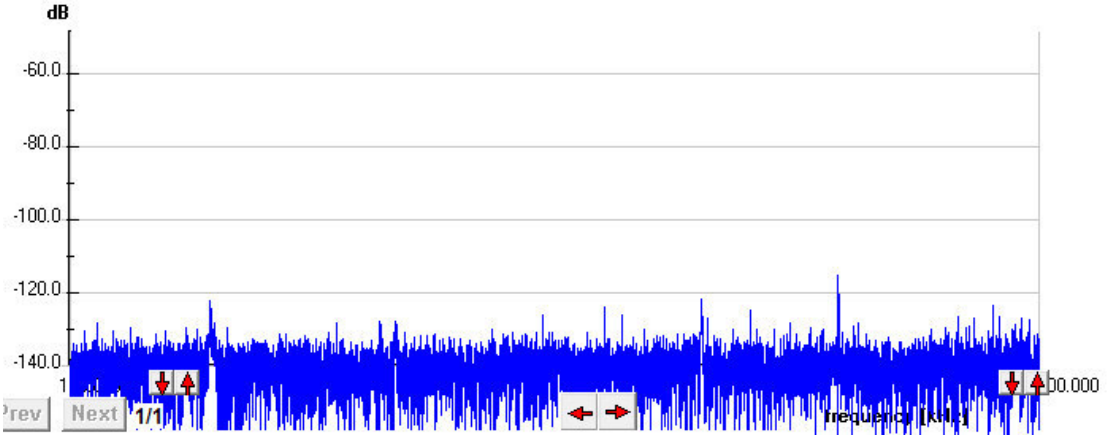


Figure 6.77: ZrNiSn sample measured at 350 °C. Frequency interval 100-1001 kHz.

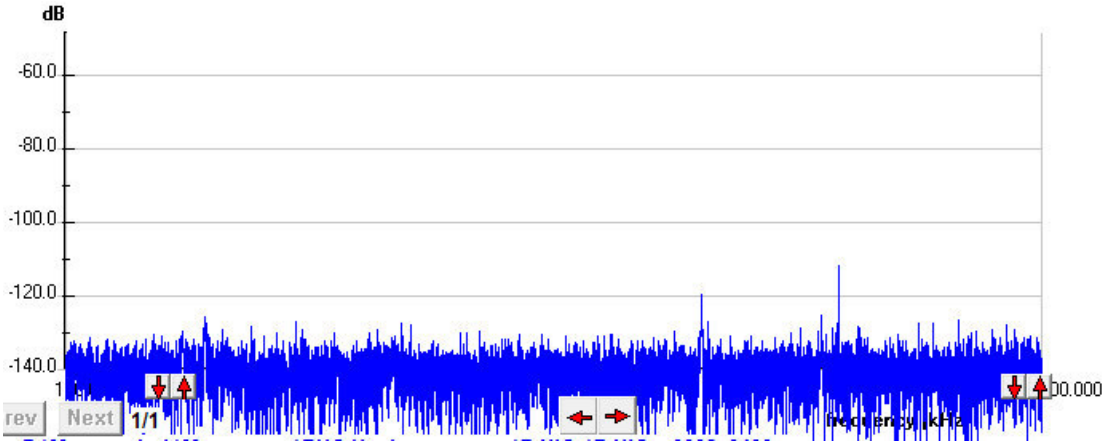


Figure 6.78: ZrNiSn sample measured at 400 °C. Frequency interval 100-1001 kHz.

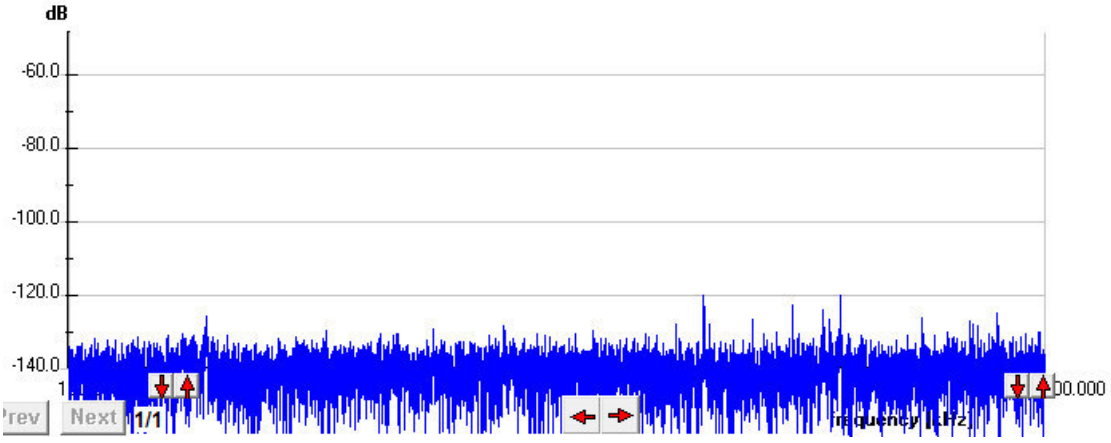


Figure 6.79: ZrNiSn sample measured at 450 °C. Frequency interval 100-1001 kHz.

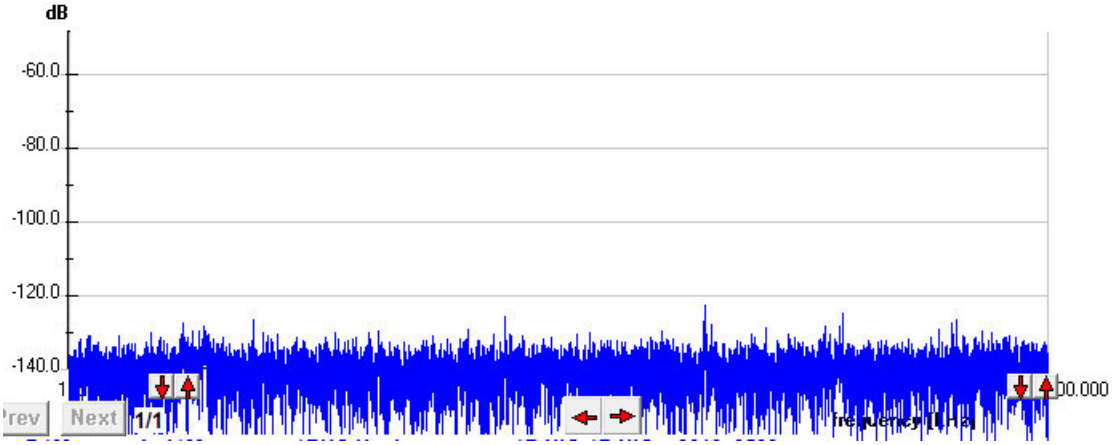


Figure 6.80: ZrNiSn sample measured at 500 °C. Frequency interval 100-1001 kHz.

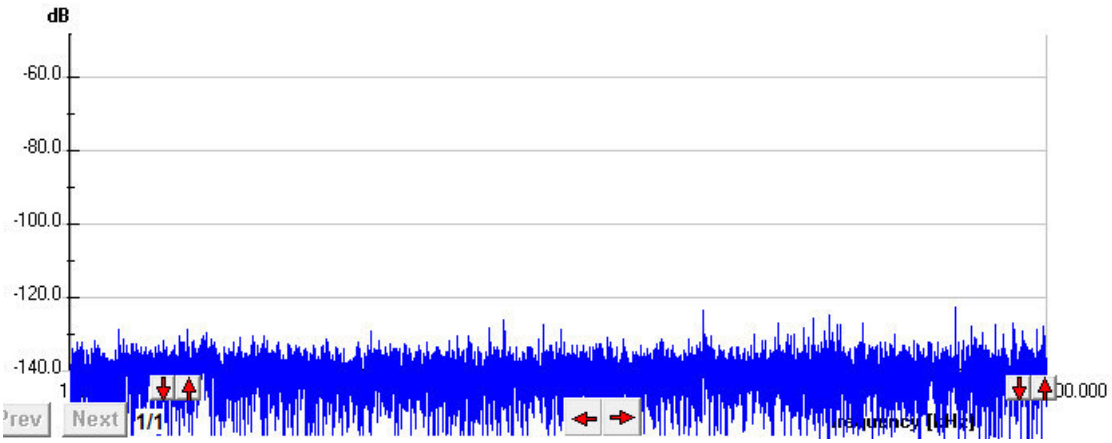


Figure 6.81: ZrNiSn sample measured at 550 °C. Frequency interval 100-1001 kHz.

Table 6.13: Resonant frequencies in [Hz] for the ZrNiSn sample.

25 °C	50 °C	100 °C	150 °C	200 °C	250 °C
141062	140725	140400	139903	139886	140686
144022	220745	220327	219639	219654	218143
221412	295352	295033	291602	291631	289378
292706	431927	397872	396571	393440	390507
294318	444382	429568	429737	429658	414211
399615	453311	452787	442479	442516	443000
400550	626794	456133	454704	452138	454585
432105	634589	779861	596783	539650	529000
435159		945278	624913	593254	594908
457635		953542	637681	624809	624101
461286			932485	631157	626529
461749			940386	687270	679000
560572			948700	769129	686000
613521				850129	775813
636486				940425	800000
652207					841000
702421					856287
709551					935073
712321					938271
797302					
815468					
866082					
946620					
951118					
969273					
976997					
977857					
995354					

Table 6.14: Resonant frequencies in [Hz] for the ZrNiSn sample.

300 °C	350 °C	400 °C	450 °C	500 °C	550 °C
140106	139377	138799	138189	137270	137720
217376	208901	282412	279230	206660	206675
288246	286170	430164	419331	278533	277980
393446	390839	447880	447022	389388	429341
413404	431492	610780	588832	403279	445042
443740	448181	619284	609529	446034	615541
449719	581625	663353	618032	514500	838773
594411	619644	749390	752836	586313	924145
623720	620524	823431	838849	613222	925251
799776	790906	830712	920787	616811	
844799	839945	905613	924076	822421	
856767	909722	921807		904339	
926542	924498			909344	
935666	938277			923926	
939206				924735	

Table 6.15: ZrNiSn: E, G and ν from 25 to 550 °C

T [°C]	E [GPa]	± [GPa]	ν	±	G [GPa]	± [GPa]
25	184.34	1.95	0.244	0.007	74.06	0.88
50	183.58	3.1	0.252	0.001	74.11	1.27
100	181.1	1.51	0.248	0.013	72.54	0.95
150	178.41	2.59	0.245	0.005	71.64	1.08
200	176.76	2.1	0.243	0.001	71.13	0.84
250	174.54	2.19	0.215	0.002	71.79	0.90
300	172.24	2.51	0.222	0.001	71.31	1.04
350	170.19	1.71	0.218	0.01	69.87	0.90
400	167.64	2.44	0.233	0.004	67.97	1.01
450	165.1	2.6	0.234	0.003	67.29	1.09
500	163.36	2.8	0.208	0.001	67.57	2.02
550	159.21	2.36	0.224	0.006	65.02	0.96

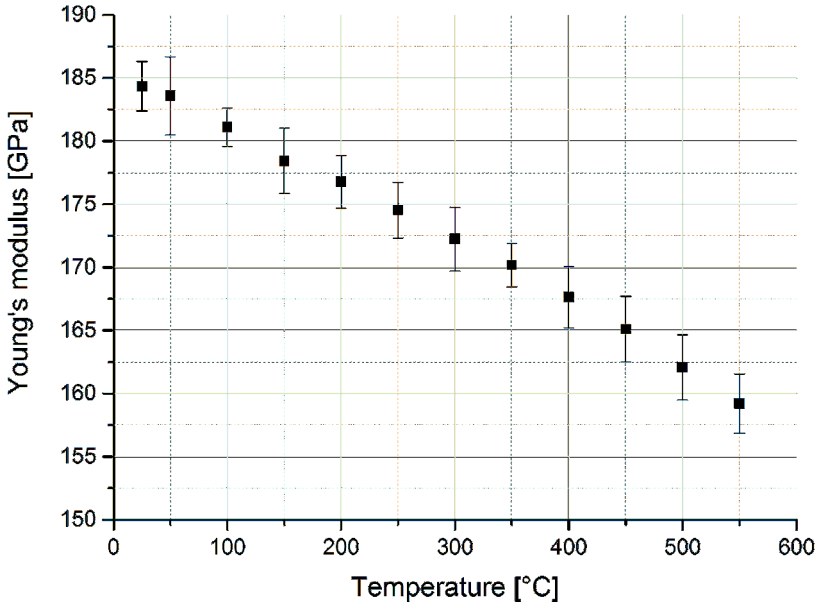


Figure 6.82: Young's modulus vs temperature for ZrNiSn.

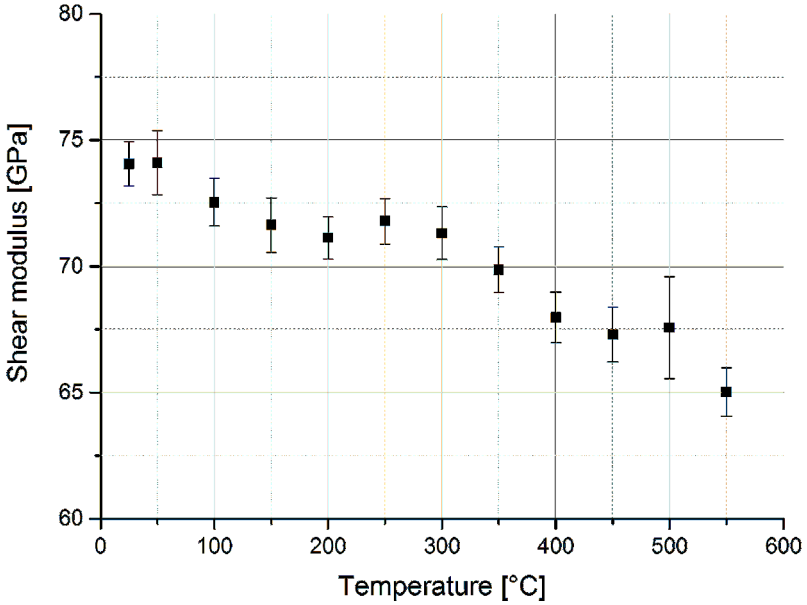


Figure 6.83: Shear modulus vs temperature for ZrNiSn.

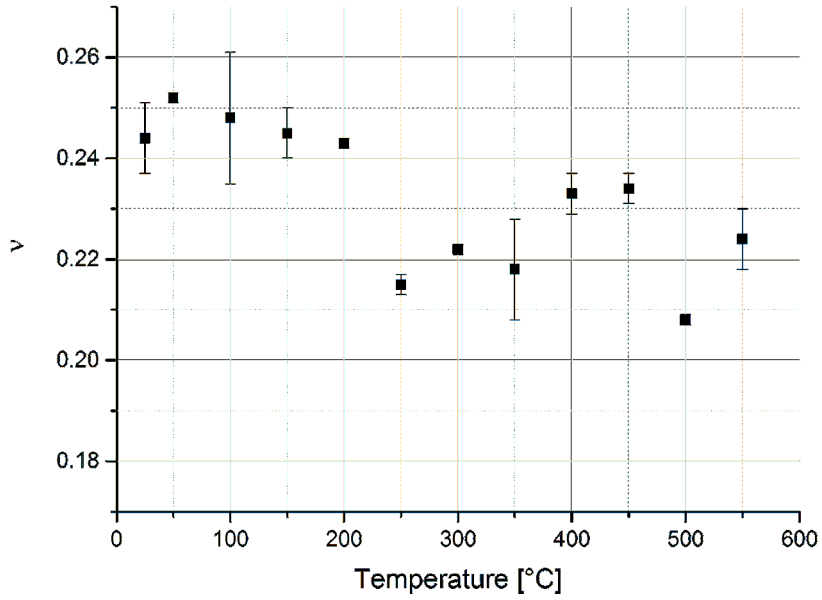


Figure 6.84: Poisson's ratio vs temperature for ZrNiSn.

6.7 Vycor 7930

The following RUS spectrum was recorded:

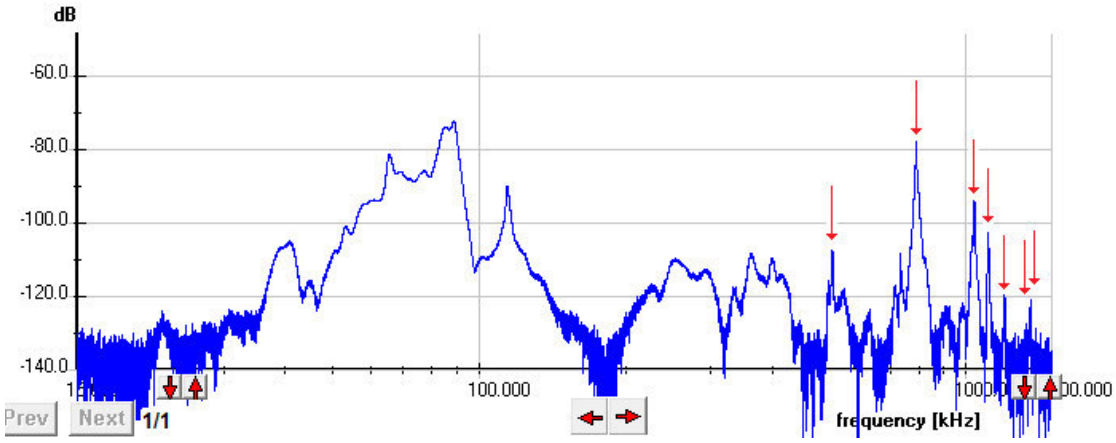


Figure 6.85: Vycor 7930 sample measured at 25 °C. Frequency interval 15-1500 kHz. Red arrows indicate RUS peaks.

Table 6.16: Resonant frequencies in [Hz] for the Vycor 7930 sample.

25 °C
532209
790158
1040424
1111401
1200216
1338143
1357035

Table 6.17: Vycor 7930: E, G and ν at 25 °C.

E [GPa]	± [GPa]	nu	±	G [GPa]	± [GPa]
17.37	0.36	0.33	0.001	6.52	0.13

6.8 Discussion

Ceramics: Our samples made of Si_3N_4, Al_2O_3 and ZrO_2 were perfectly suited for RUS. As ceramics, the damping of the samples was rather low, the samples dimensions were very precise and resonant frequencies could be detected easily. As seen in the RUS spectra, a large number of resonant peaks could be measured at room temperature. From the set of frequencies, the materials were identified as isotropic. At high temperatures, using the newly developed RUS equipment, the number of resonant peaks decreased, but the number of identified peaks was still sufficient to determine elastic constants. Due to the detrimental effect of a high temperature to the piezoelectric transducers, there was no direct contact between sample and transducers, which reduced the signal to noise ratio. The Young's modulus and shear modulus decreased with temperature for alumina and silicon nitride, which is consistent with literature values for alumina [37], [38] and silicon nitride [40]. The Poisson ratio was nearly constant for the whole temperature range measured, which was also observed for silicon nitride [41]. However, as for alumina, literature values for the Poisson ratio increase slightly from 350 °C onwards, and more rapidly from 1200 °C onwards [39]. The slight increase could not be observed for our alumina sample and the strong increase shown in [39] could not be verified due to the furnace maximum temperature of 900 °C. The situation was different for zirconia. In the literature [42], for Yttria stabilized zirconia, a Young's modulus vs temperature curve showing 2 distinct regions was observed. A rapid decrease of the Young's modulus up to 400 °C and a slow decrease above this temperature. Our results (see figure 6.37) are consistent with these findings and the Young's modulus vs temperature curve appears to be very similar. There are various explanations for the strong decrease, such as elastic anisotropy [42] or relaxation of oxygen vacancies [43]. However, this is still a matter of discussion and further experiments are required. As for the Poisson ratio, a complicated behavior was found for different temperatures. Due to a weak statistical correlation further experiments are necessary.

Thermoelectric alloys: XNiSn (X=Hf, Ti, Zr) samples were considerably more challenging to analyze. Starting with low temperature measurements, there was no noteworthy increase in complexity, despite the fact that shape and composition of the thermoelectric materials were less favorable compared to the ceramic samples. However, as for the high temperature RUS (HT-RUS), the signal to noise ratio was reduced significantly, resulting in resonant peaks that could no longer be identified in some cases. To increase the signal to noise ratio in order to improve the applicability of HT-RUS for such difficult samples, piezoelectric transducers that are able to operate at higher temperatures are a potential solution [46]. A possible explanation for the poor performance of HT-RUS could be that due to the relatively low melting point of Sn (231 °C) the material became softer, which resulted in more damped resonances. As a consequence of this damping effects, some resonant frequencies might not be detected. Other factors which could have influenced HT-RUS are phase transitions or phase segregations and the potential change in viscosity of the new phase. Temperature dependence of viscoelastic properties of the Sn component could have an influence on the alloys elastic behavior, which is not negligible. For all samples the Young's modulus and shear modulus decreased at higher temperatures. The Poisson ratio showed a complicated behavior for all 3 alloys and no quantifiable temperature dependence could be determined. A comparison with literature values for the temperature dependence of Young's modulus, shear modulus and Poisson ratio for XNiSn (X=Hf, Ti, Zr) is currently not available because most literature focuses on thermoelectric properties rather than mechanical properties (which was the main reason for our measurements, that are part of [45]). It is worth mentioning that the curvature of the HfNiSn Young's modulus vs temperature graph is convex. That is different from the usual $E(T)$ graph, which is mostly described by a concave function. This behavior could be attributed to a phase transition but this is still a matter of discussion and further experiments are required.

Vycor 7930: The porous glass showed only a very limited number of resonant frequencies even at room temperature, which could be attributed to the materials porosity. In general, 7 measured frequencies are insufficient for a successful evaluation of elastic constants. However, the determined value of 17.37 ± 0.36 GPa for the Young's modulus was surprisingly similar to the value given in the product catalog of the sample, which is 17.23 GPa [57]. We can therefore conclude that a small number of resonant frequencies can be sufficient, as long as one is able to identify and allocate them correctly.

7 Conclusion

RUS at room temperature is a well established method to determine elastic constants. In the past 20 years measurable sample shapes and materials were extended continuously. Due to its high accuracy and the fact that the complete elastic tensor can be determined from one single measurement, RUS became a widely used method for measuring elastic constants. An essential part of RUS is the calculation of the samples eigenmodes, which can be achieved if shape, mass and elastic constants of the sample are known. The challenging part of this work was the evaluation of the temperature dependence of these constants. For a successful analysis of high temperature data, a preceding room temperature measurement is crucial, otherwise it is an exceedingly difficult task to identify resonant frequencies. Even if a complete set of room temperature frequencies is available, effects such as softening of the sample, or temperature induced phase transitions can reduce the number of detected resonant frequencies to such a degree that the data evaluation becomes very challenging. This is the case for the HT-RUS of the thermoelectric alloy samples. Since phase transitions or softening is difficult to counter for a predefined sample, a possible improvement lies in a better signal to noise ratio which can be achieved by using a direct-contact setup (based on the prerequisite that high temperature piezoelectric transducers are available) instead of a buffer-rod setup.

Appendices

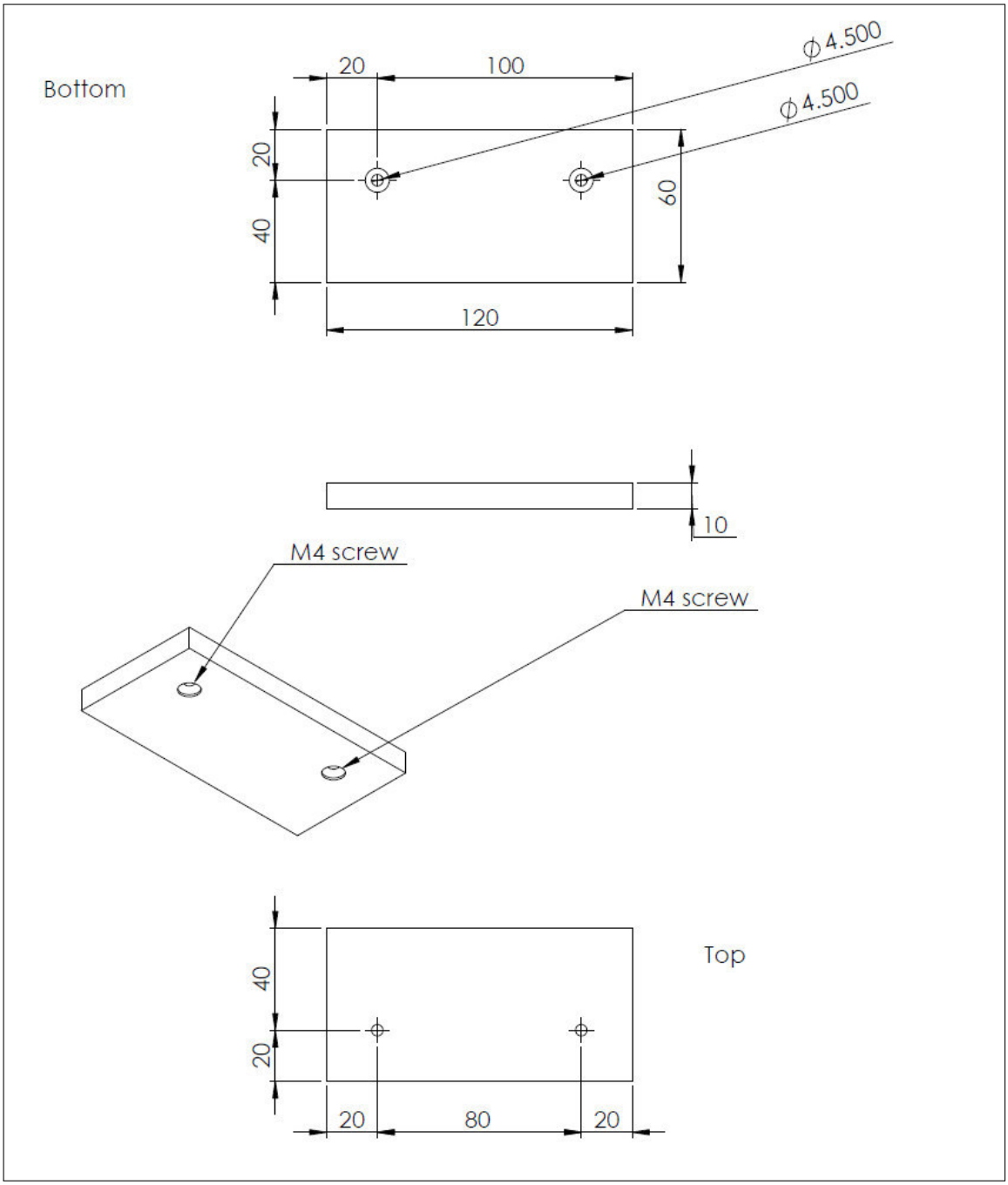


Figure A1: Base plate.

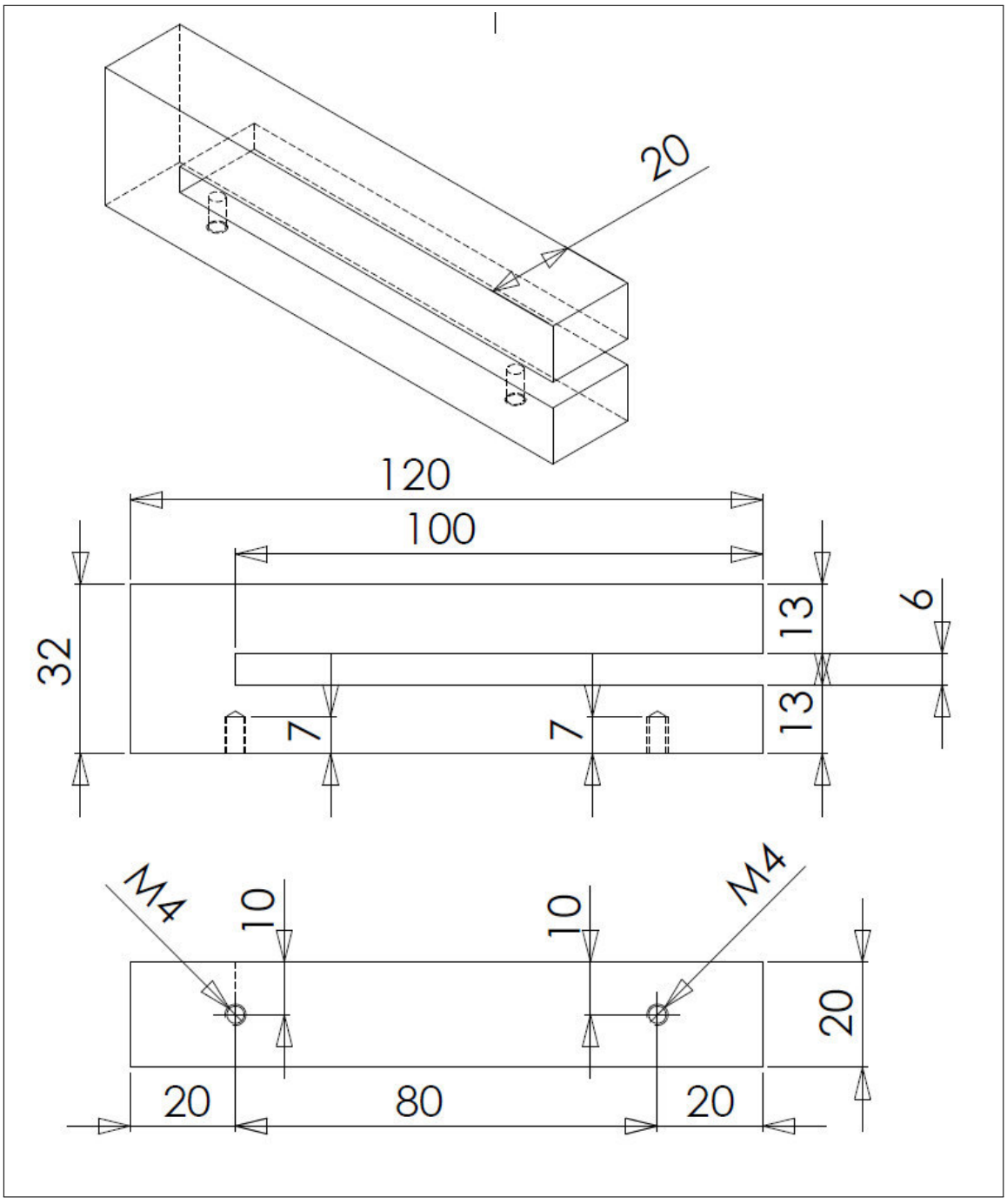


Figure A2: Guidance for the piezoelectric transducer mounting parts (figure A3 and A5).

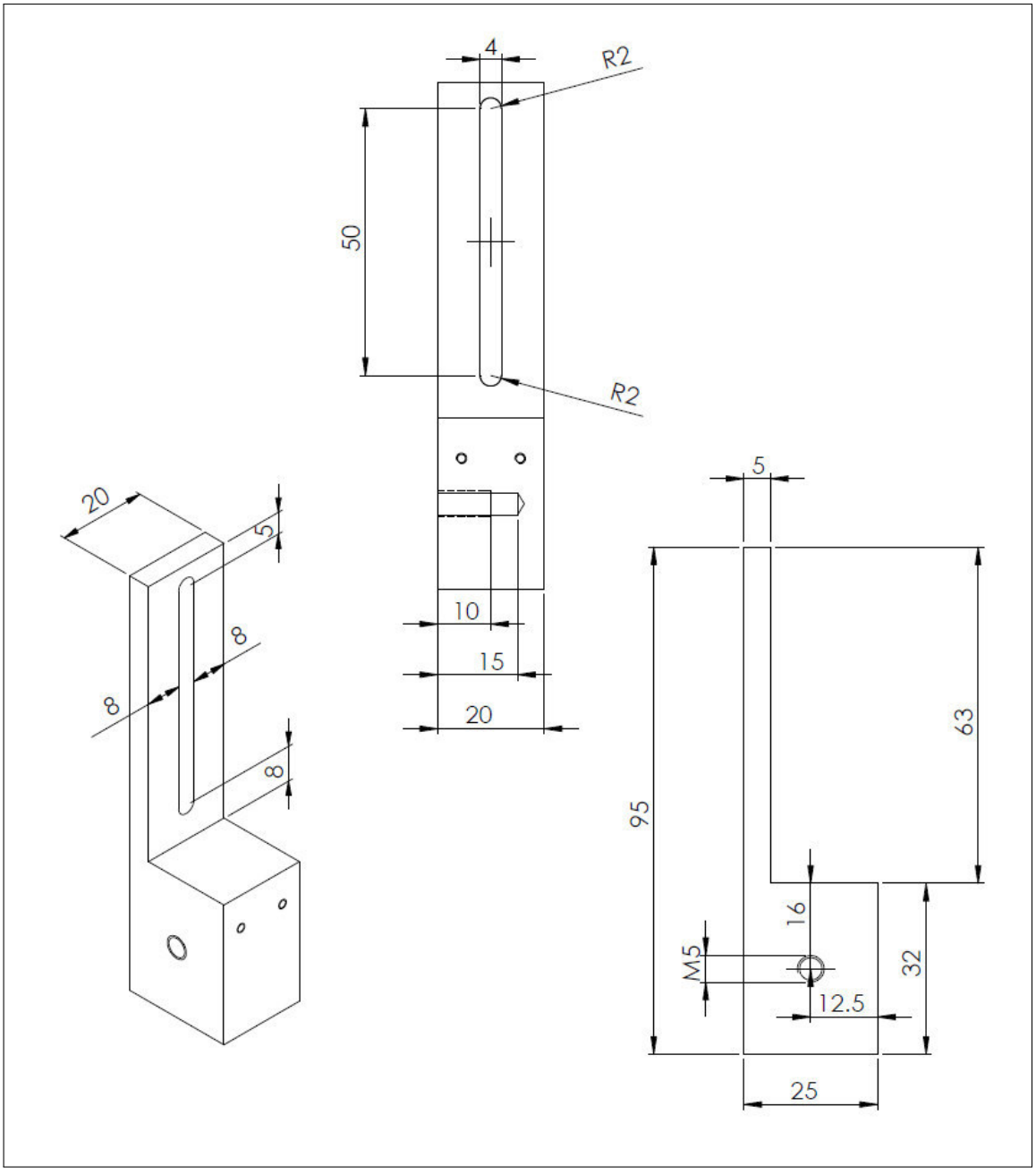


Figure A3: Mounting part for vertical and horizontal movement.

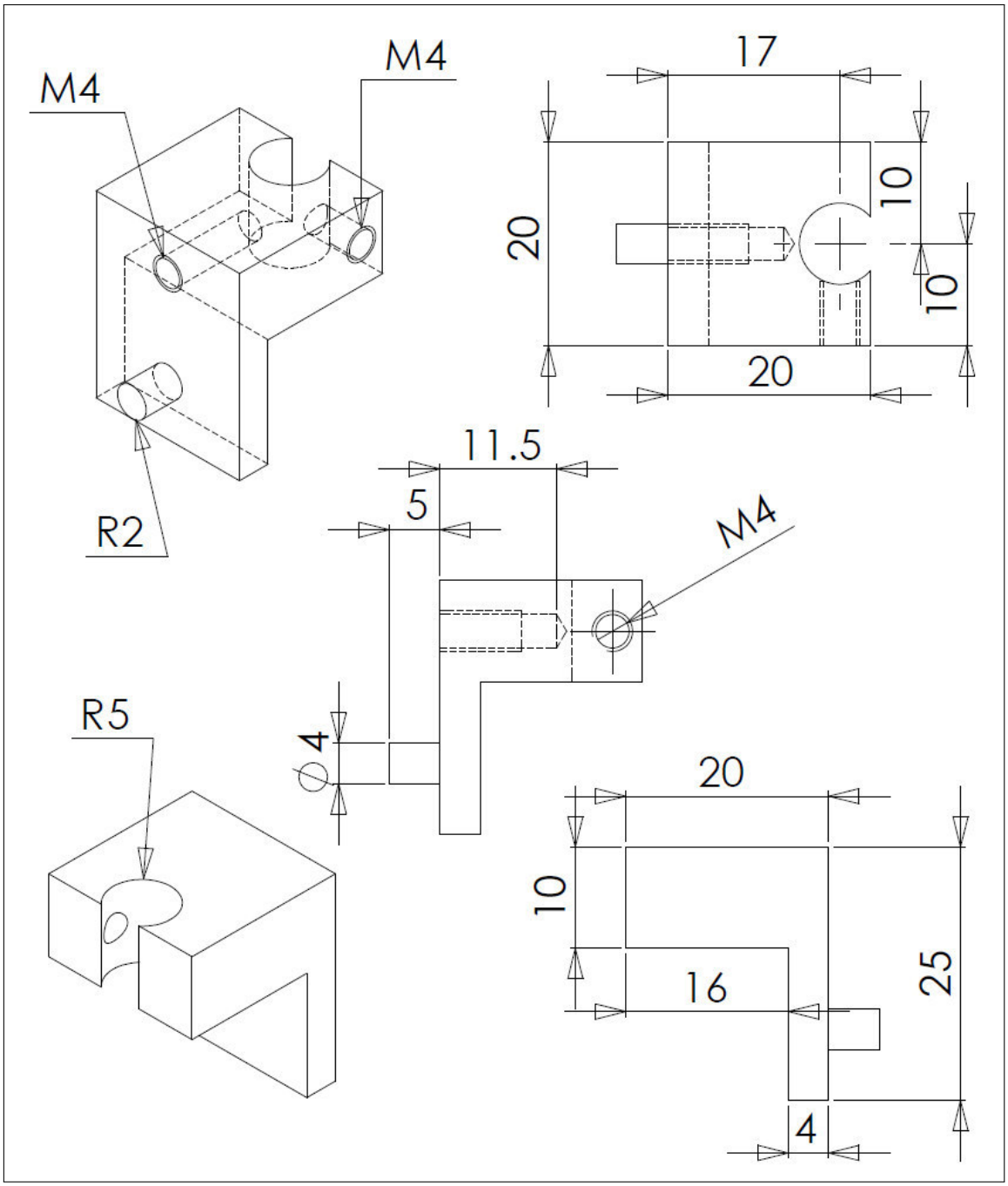


Figure A4: Mounting part for one of the piezoelectric transducers.

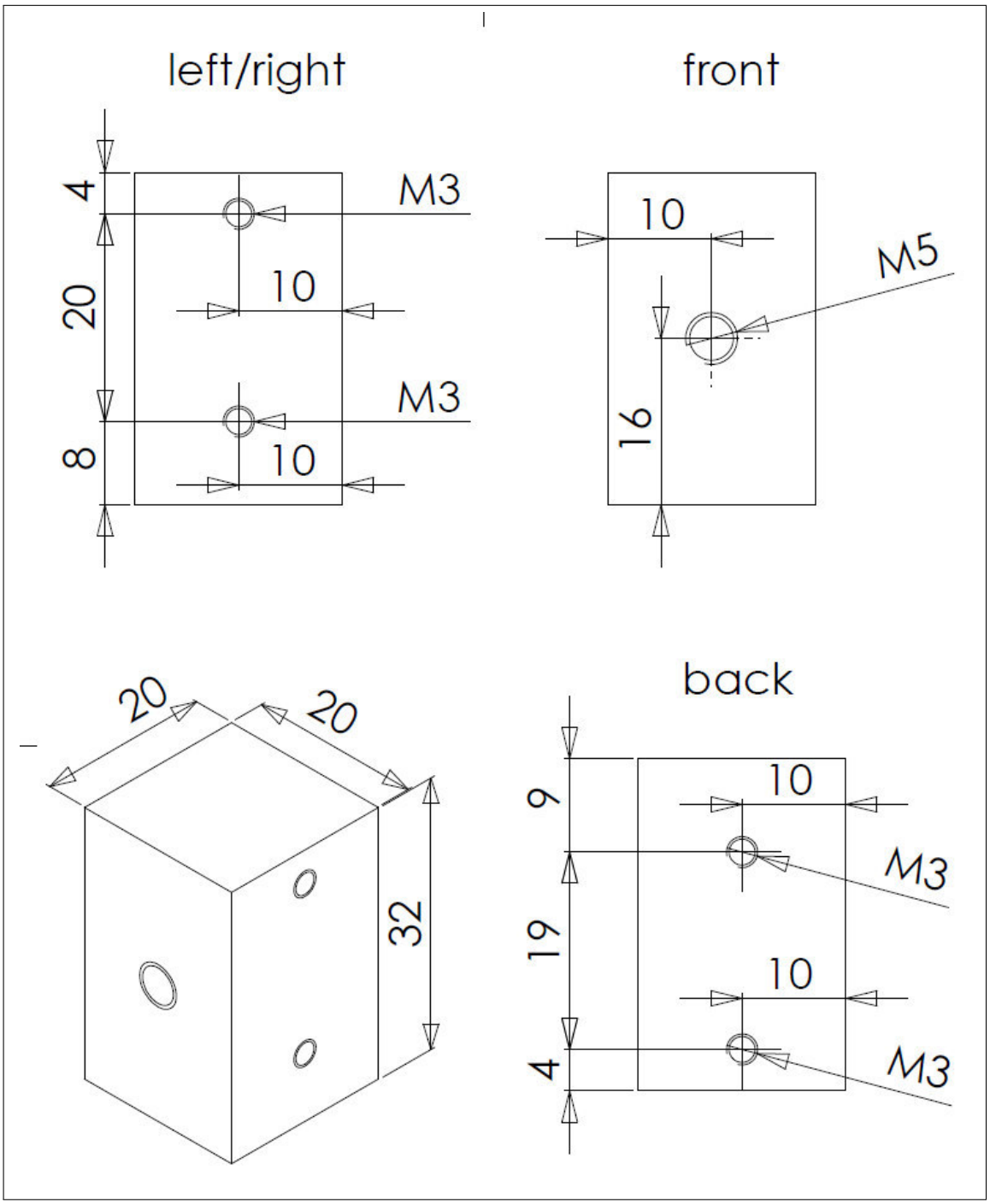


Figure A5: Mounting part for the 2 linear guides and the mounting part for the bearings.

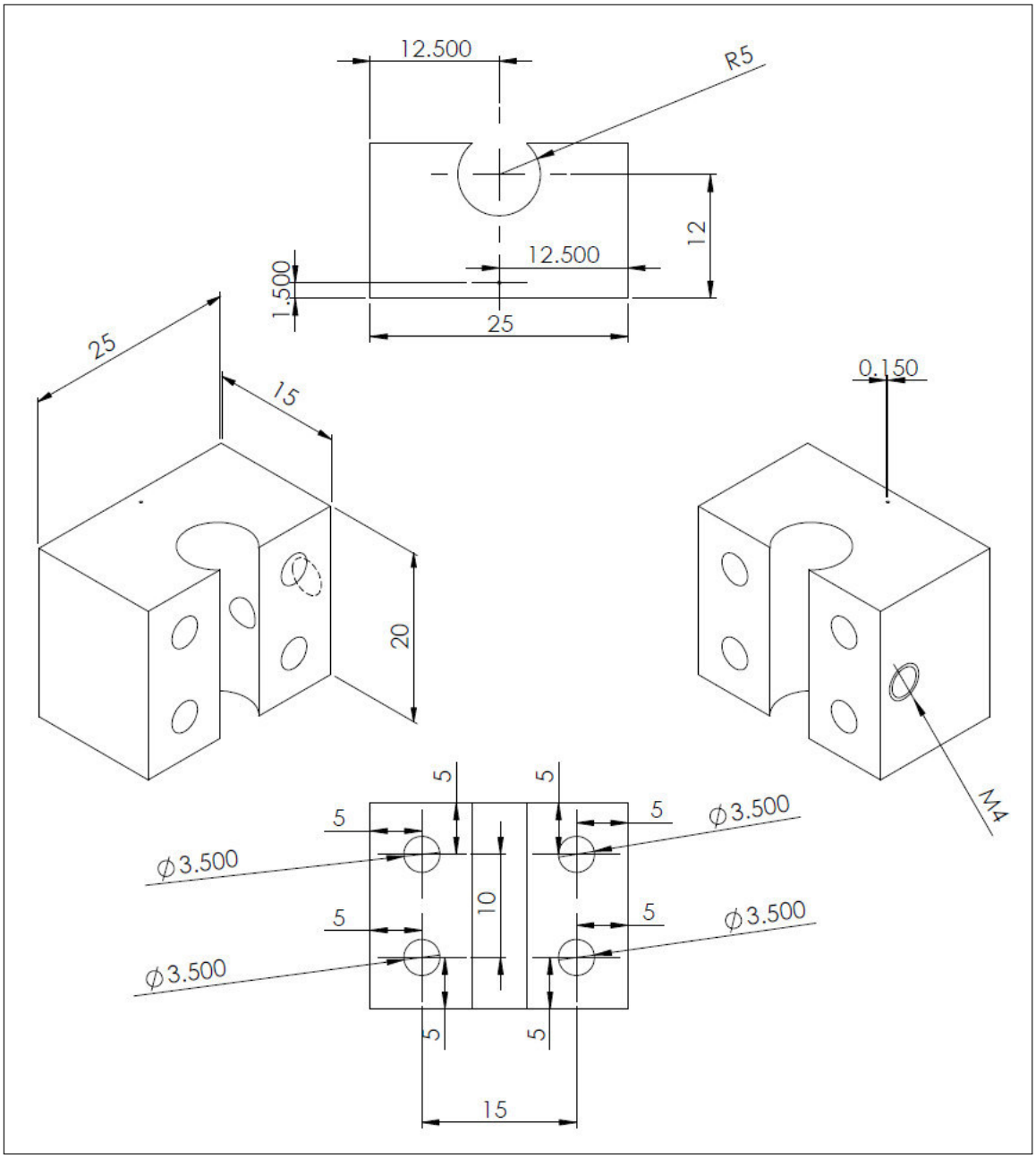


Figure A6: Mounting part for one of the piezoelectric transducers.

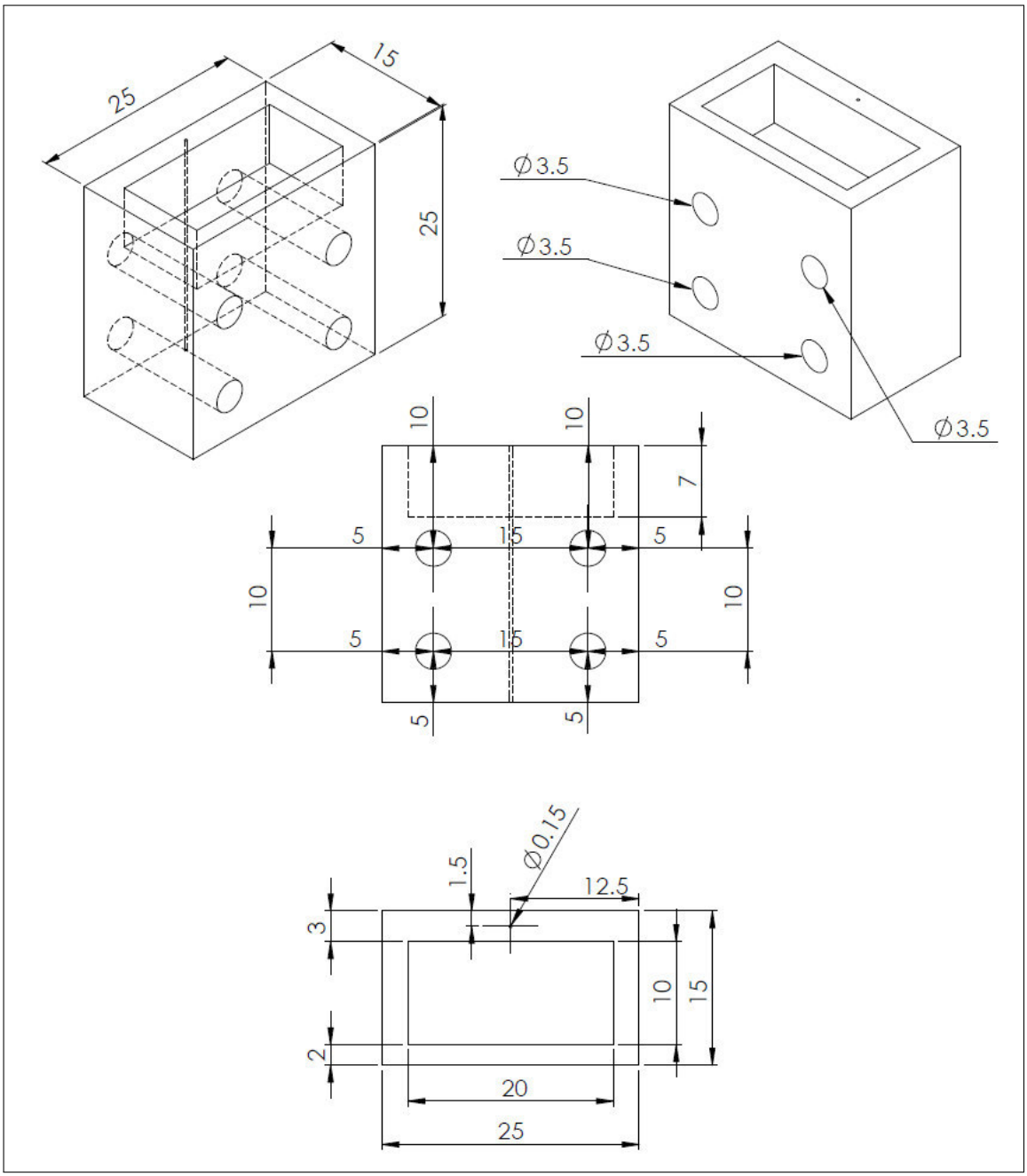


Figure A7: Counter weight to balance the weight of the piezoelectric transducer.

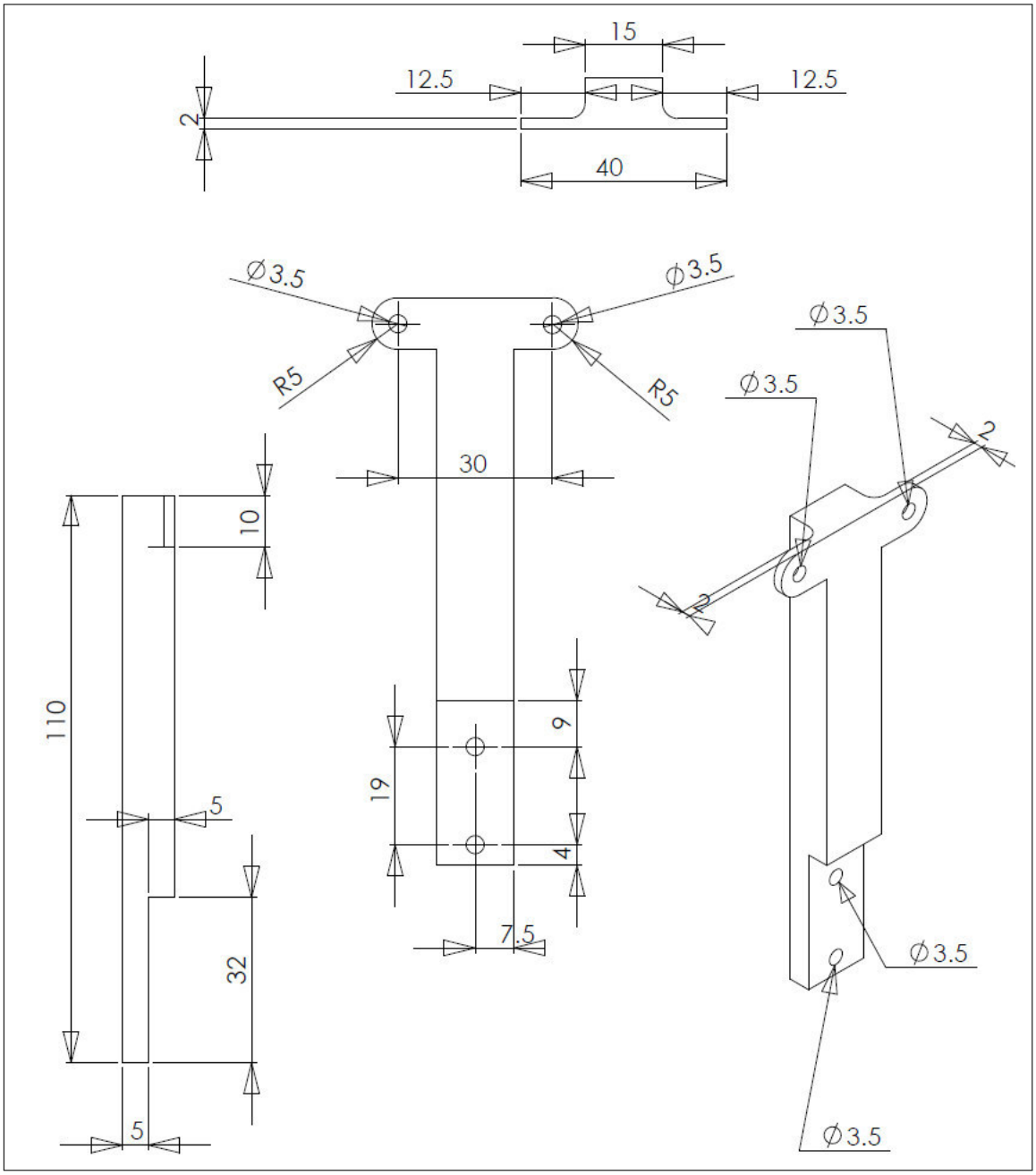


Figure A8: Mounting part for the bearings.

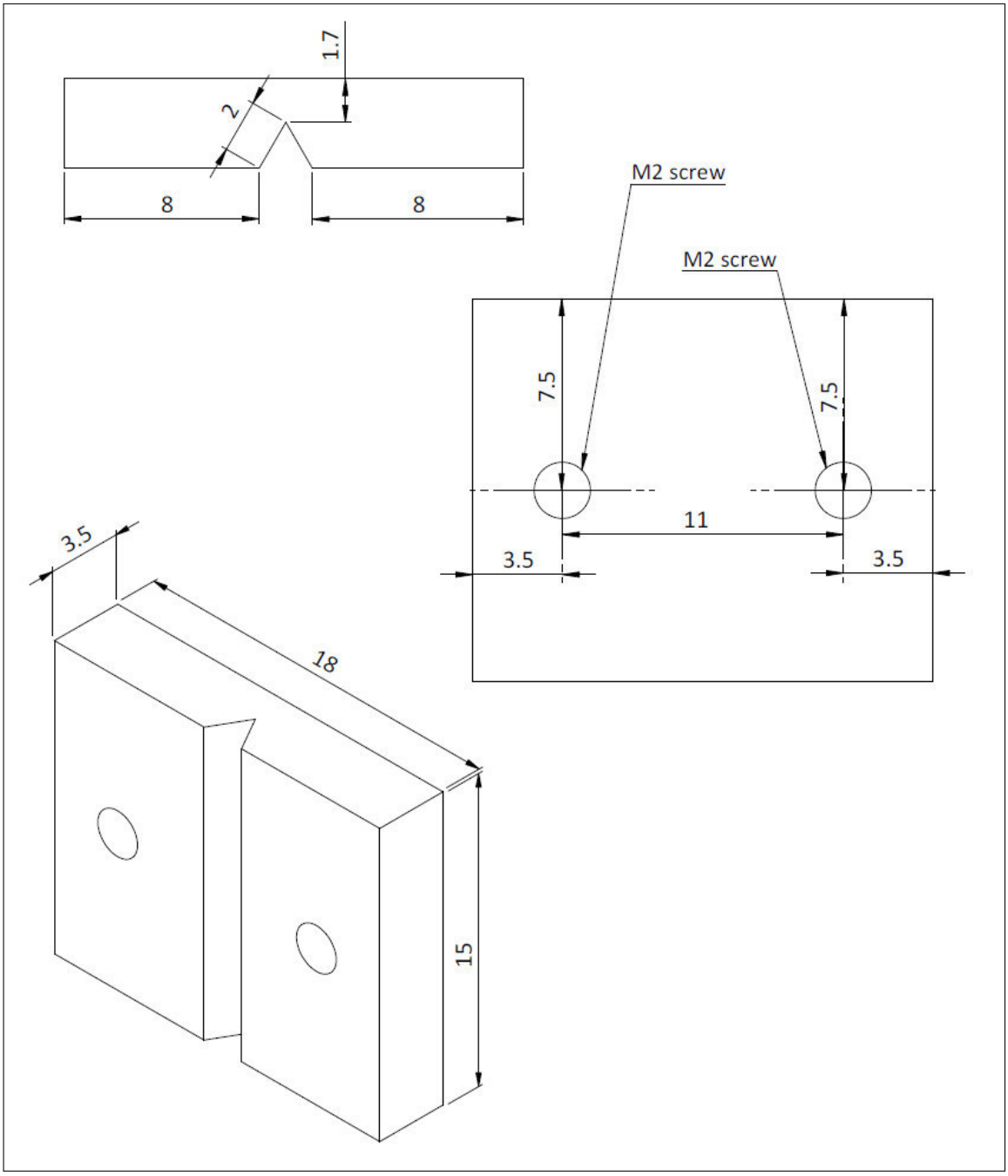


Figure A9: A part for holding the temperature sensor in place.

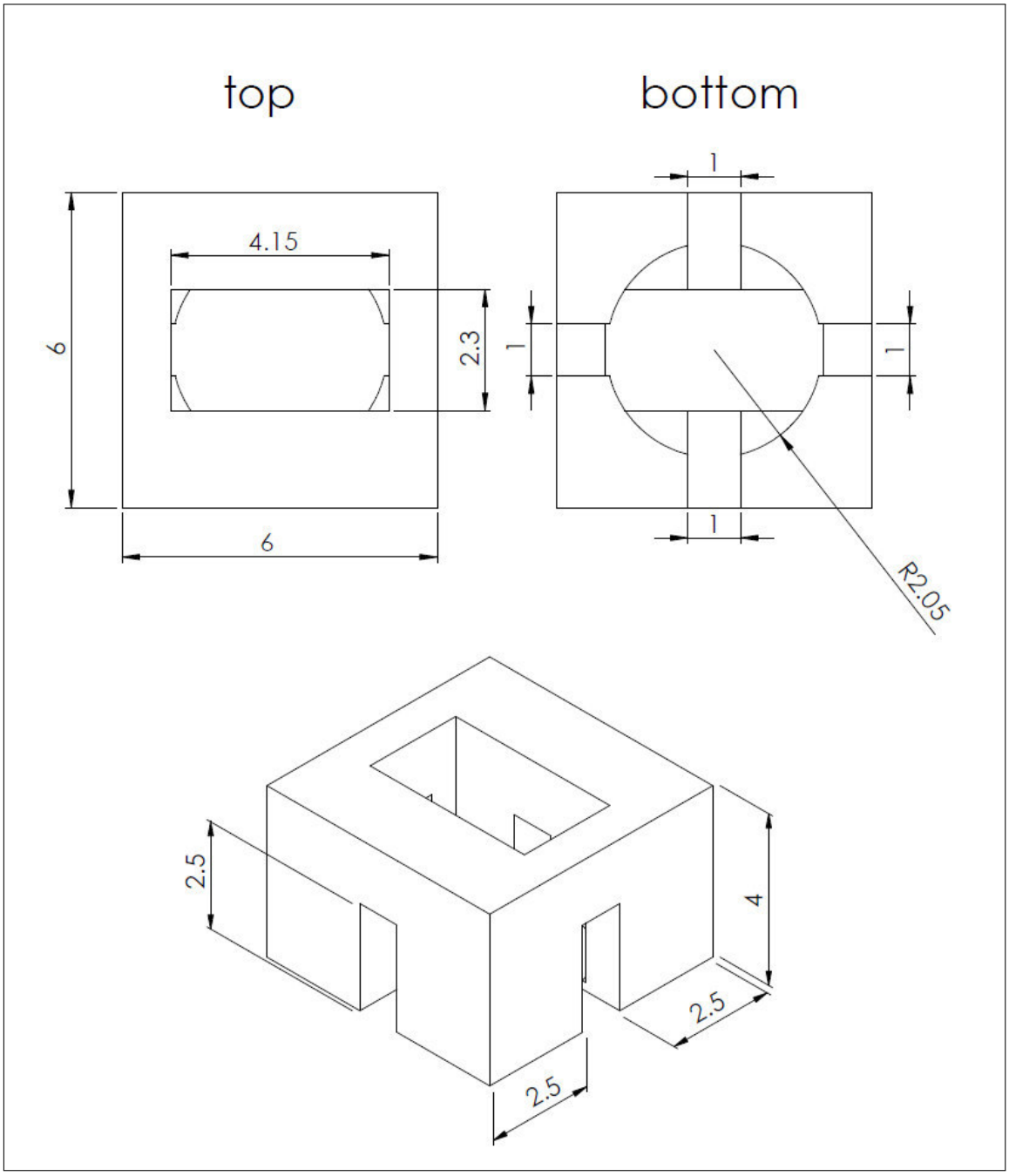


Figure A10: A clamp that connects the piezoelectric transducer to the buffer rod.

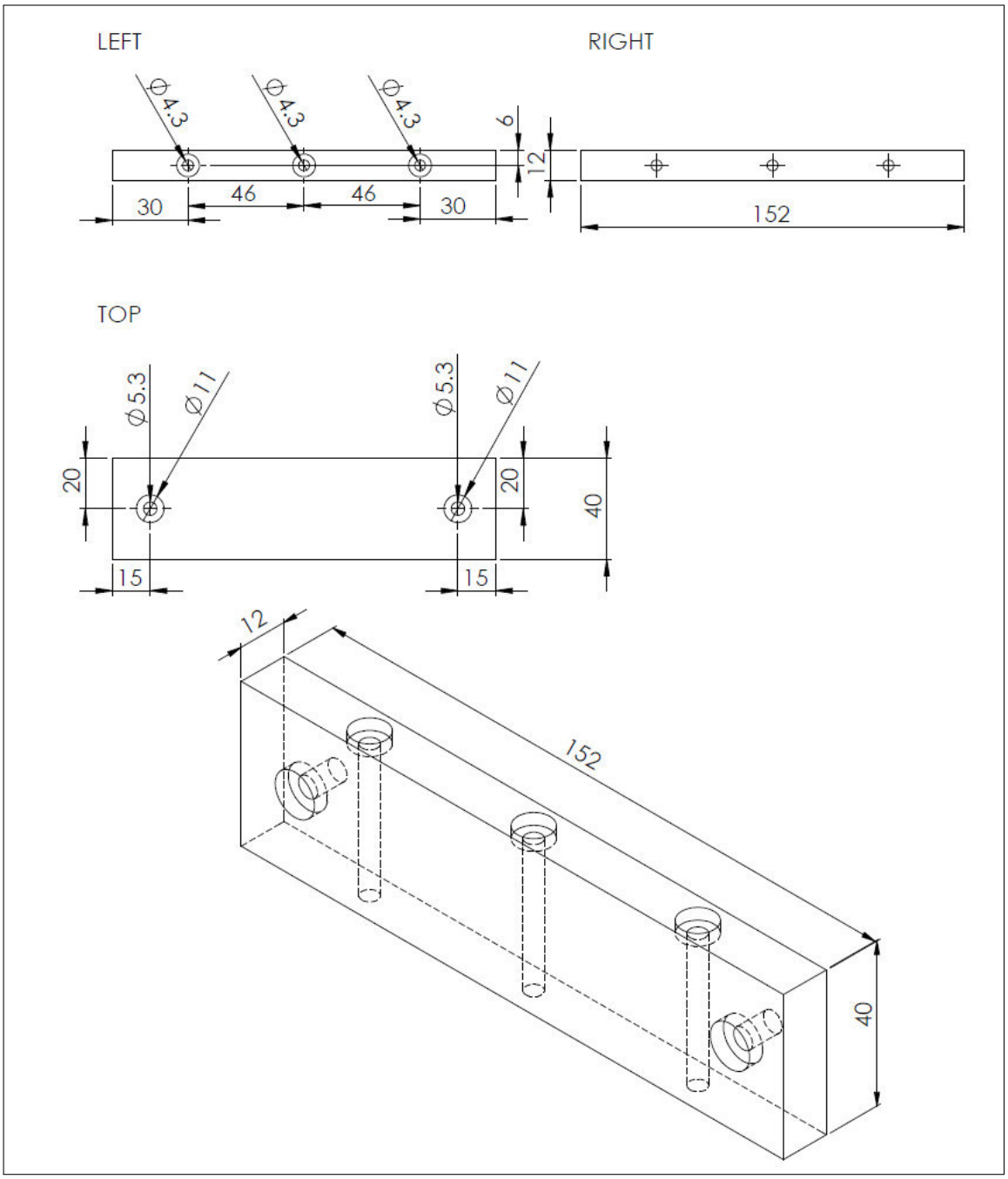


Figure A11: Cooling plate extension.

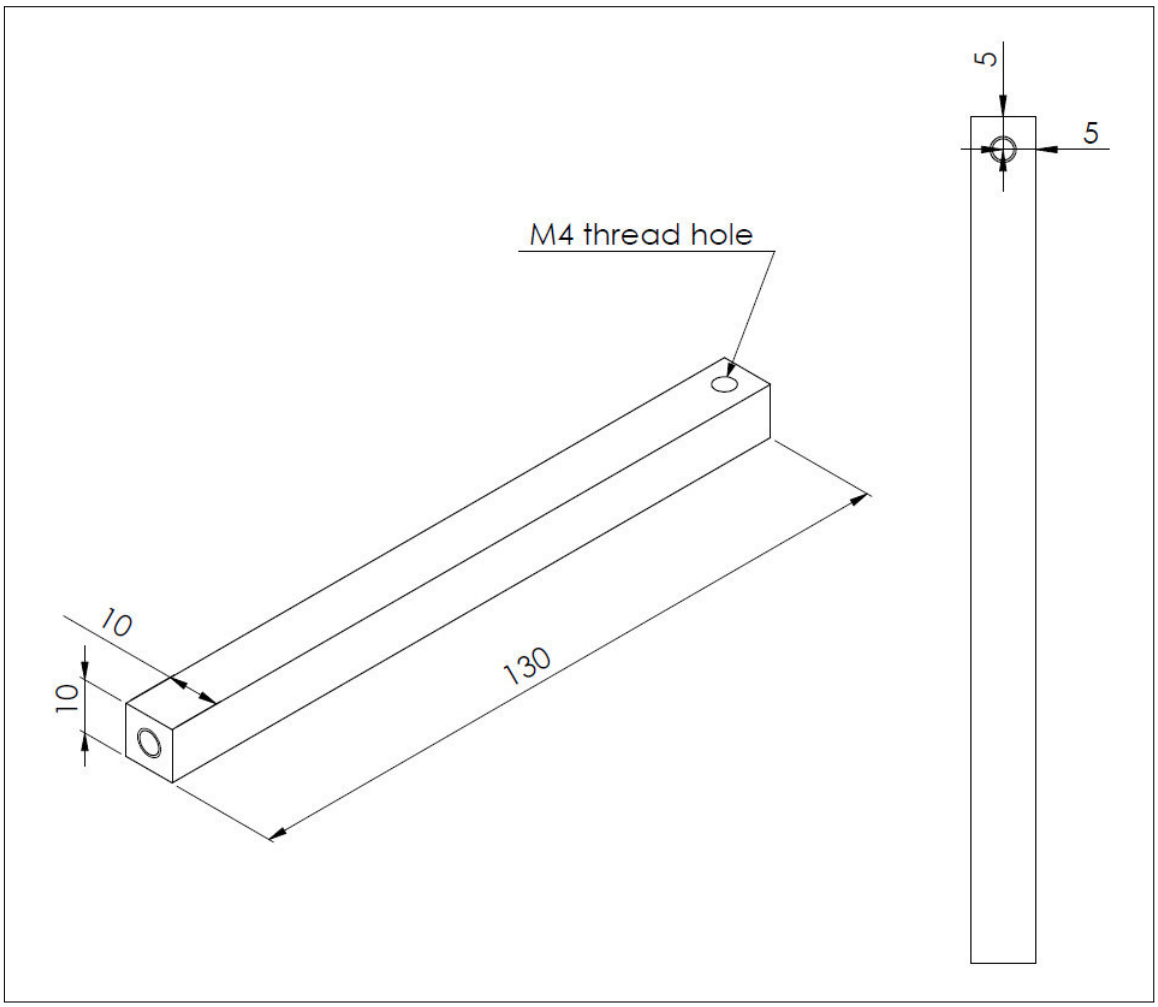


Figure A12: Cooling plate pedestals.

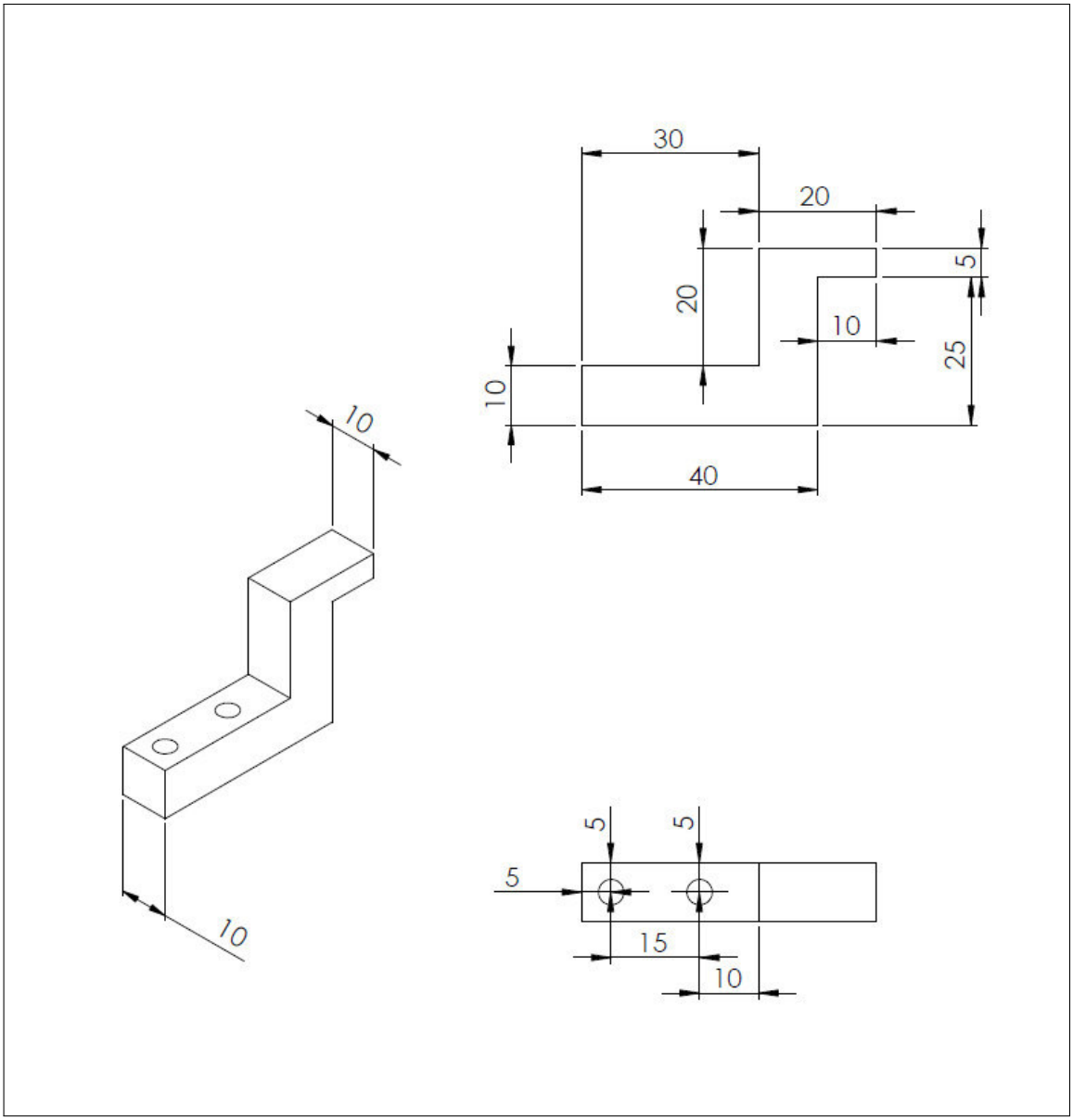


Figure A13: A part to add more stability to the furnace while attached to the linear guide.

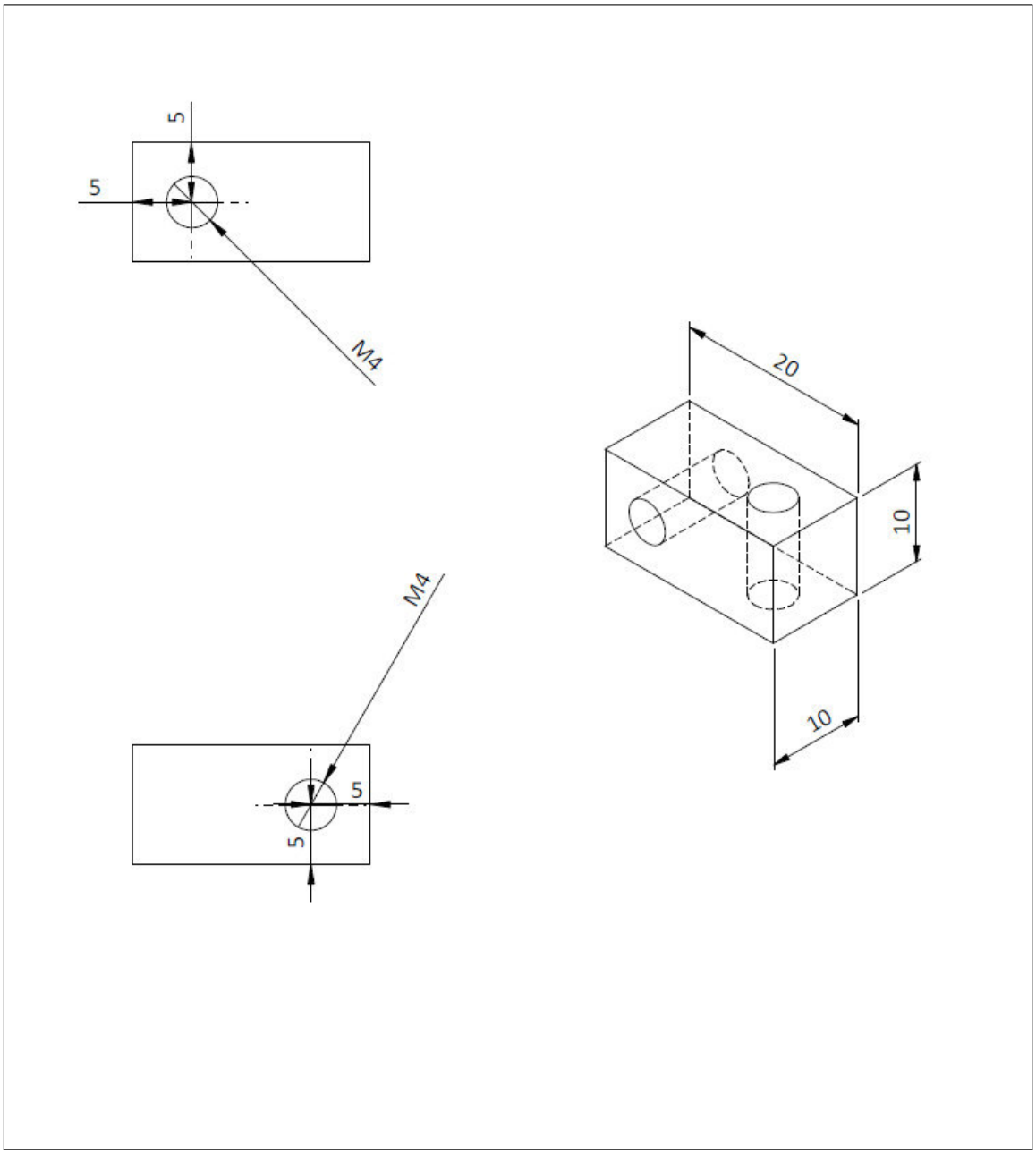


Figure A14: 4 of these parts mounted the cooling plate to the ground plate.

Bibliography

[1] Resonant Ultrasound Spectroscopy, J. Maynard, Physics Today 49(1), 26 (1996)

[2] Resonant ultrasound spectroscopy, R.G. Leisure and F.A. Willis, J. Phys.: Condens. Matter 9 (1997) 6001–6029

[3] Ein neues Messverfahren zur Bestimmung des Elastizitätsmoduls und der Dämpfung, F. Förster, Zeitschrift für Metallkunde 29 (1937) 109–115

[4] Young's and shear moduli of laminated carbon/carbon composites by a resonant beam method, A. Wanner, K. Kromp, Brittle Matrix Composites, Vol. 2, 1988, pp. 280–289

[5] A novel resonant beam technique to determine the elastic moduli in dependence on orientation and temperature up to 2000 °C, W. Lins, G. Kaindl, H. Peterlik, K. Kromp, Review of Scientific Instruments 90 (7) (1999) 3052–3058

[6] Extension of the resonant beam technique to highly anisotropic materials, S. Puchegger, D. Loidl, K. Kromp, H. Peterlik, R. Weiß, Journal of Sound and Vibration 279 (2005) 1121–1129

[7] Treatise on the Mathematical Theory of Elasticity, A. E. H. Love, Cambridge U. P. (1927)

[8] Cube-resonance method to determine elastic constants of solids, H. H. Demarest Jr., J. Acoust. Soc. Am. 49, 768 (1971)

[9] Elastic constants and specific-heat measurements on single crystals of La_2CuO_4, A. Migliori et al., Phys. Rev. B 41, 2098 (1990)

[10] Festkörperphysik, chapter 4, R. Gross and A. Marx, Oldenbourg Wissenschaftsverlag (2012)

[11] Determination of Elastic Constants from Sound-Velocity Measurements in Crystals of General Symmetry, J. R. Neighbours, G. E. Schacher, Journal of Applied Physics 38, 5366 (1967)

[12] Migliori A, Sarrao J L, Visscher W M, Bell T M, Lei M, Fisk Z and Leisure R G 1993 Physica B 183 1

[13] Kuokkala V-T and Schwarz R B 1992 Rev. Sci. Instrum. 63 3136

[14] Holland R 1968 J. Acoust. Soc. Am. 43 988

[15] Ohno I 1976 J. Phys. Earth 24 355

[16] Ohno I, Yamamoto S, Anderson O L and Noda J 1986 J. Phys. C: Solid State Phys. 47 1103

[17] Visscher W M, Migliori A, Bell T M and Reinert R A 1991 J. Acoust. Soc. Am. 90 2154

[18] Characterization of thin films and novel materials by resonant ultrasound spectroscopy, J. R. Gladden, Ph.D. thesis, The Pennsylvania State University, USA (2003)

[19] Measurement of the elastic constants of a columnar SiC thin film, K. A. Pestka II, J. D. Maynard, D. Gao, and C. Carraro, Physical Review Letters, vol. 100, no. 5

[20] Rectangular parallelepiped resonance - a technique of resonance ultrasound and its applications to the determination of elasticity at high temperatures, O. L. Anderson, Journal of the Acoustical Society of America, vol. 91, no. 4, pp. 2245–2253, 1992

[21] Elastic constants of corundum up to 1825 K, T. Goto, O. L. Anderson, I. Ohno, and S. Yamamoto, Journal of Geophysical Research, vol. 94, no. 6, pp. 7588–7602, 1989

[22] Temperature variation of elastic constants of quartz across the α-β transition, I. Ohno, K.Harada, and C. Yoshitomi, Physics and Chemistry ofMinerals, vol. 33, no. 1, pp. 1-9, 2006

[23] Temperature variation of elastic constants of single crystal forsterite between 190 °C and 400 °C, Y. Sumino, O. Nishizawa, T. Goto, I. Ohno, and M. Ozima, Journal of Physics of the Earth, vol. 25, pp. 377–392, 1977

[24] Elastic properties of a single-crystal forsterite Mg_2SiO_4, up to 1200K, I. Suzuki, O. L. Anderson, and Y. Sumino, Physics and Chemistry of Minerals, vol. 10, no. 1, pp. 38–46, 1983

[25] Apparatus for measuring elastic constants of single crystals by a resonance technique up to 1825 K, T. Goto and O. L. Anderson, Review of Scientific Instruments, vol. 59, no. 8, pp. 1405–1408, 1988

[26] Complete elastic constants and giant softening of c66 in superconducting $La_{1.86}Sr_{0.14}CuO_4$, A. Migliori, W. M. Visscher, S. Wong, S. E. Brown, I. Tanaka, H. Kojima, P. B. Allen, Phys. Rev. Lett. 64, 2458 (1990)

[27] Elastic constants and specific-heat measurements on single crystals of La_2CuO_4, A. Migliori, W. M. Visscher, S. E. Brown et al., Physical Review B, vol. 41, no. 4, pp. 2098–2102, 1990

[28] Silicon Nitride and Related Materials, F. L. Riley, J. Am. Ceram. Soc., 83 [2] 245–65 (2000)

[29] Silicon Nitrides: Some Physico-Chemical Properties, E. T. Turkdogan, P. M. Bills, and V. A. Tippett, J. Appl. Chem. 8, 296–302 (1958)

[30] Synthesis of cubic silicon nitride, A. Zerr, G. Miehe, G. Serghiou, et al., Nature, vol. 400, issue 6742, pp. 340-342 (1999)

[31] Wikipedia, 'Silicon nitride', 2016, `https://en.wikipedia.org/w/index.php?title=Silicon_nitride&oldid=706082658`", online; accessed 10-January-2016

[32] `http://www.iycr2014.org/`, Crystallography365, J. Auckett, `http://www.iycr2014.org/learn/crystallography365/articles/20140701`

[33] Advances in Ceramics - Electric and Magnetic Ceramics, Bioceramics, Ceramics and Environment, chapter 17, C. Sikalidis, InTech (2011)

[34] Structural and thermoelectric properties of HfNiSn half-Heusler thin films, S.-H. Wang, H.-M. Cheng, R.-J. Wu, W.-H. Chao, Thin Solid Films, vol. 518, issue 21, pp. 5901–5904 (2010)

[35] Werkstoffe, chapter 8, E. Hornbogen, G. Eggeler, E. Werner, 10th edition, Springer (2012)

[36] P. S. Spoor, J. D. Maynard, AR. Kortan, Phys. Rev. Lett. 75,3462 (1995)

[37] Pressure and Temperature Dependences of the Isotropic Elastic Moduli of Polycrystalline Alumina, D.H. Chung, G. Simmons, J. Appl. Phys. 39, 5316 (1968)

[38] Ultrasonic Measurements of Young's Modulus of Al_2O_3-based Refractories at High Temperatures, C. Gault, F. Platon, D. Le Bras, Materials Science and Engineering, 74, 105-111 (1985)

[39] Temperature dependence of the elastic moduli, dilational and shear internal frictions and acoustic wave velocity for alumina, (Y)TZP and β'-sialon ceramics, M. Fukuhara, I. Yamauchi, Journal of Materials Science 28, issue 17, 4681-4688 (1993)

[40] Hightemperature elastic moduli of polycrystalline silicon nitride, W.A. Fate, J. Appl. Phys. 46, 2375 (1975)

[41] A review of the processing, composition, and temperature-dependent mechanical and thermal properties of dielectric technical ceramics, D. de Faoite et al., J. Mater. Sci. 47, 4211-4235 (2012)

[42] Young's Modulus, Flexural Strength, and Fracture of Yttria-Stabilized Zirconia versus Temperature, J. Adams et al., J. Am. Ceram. Soc. 80 [4] 903–908 (1997)

[43] Young's modulus of some SOFCs materials as a function of temperature, S. Giraud, J. Canel, Journal of the European Ceramic Society 28, 77-83 (2008)

[44] M. Gürth, G. Rogl, V.V. Romaka, A. Grytsiv, E. Bauer, P. Rogl, Thermoelectric high ZT Half-Heusler alloys $Ti_{1-x-y}Zr_xHf_yNiSn$ ($0 \leq x \leq 1$; $0 \leq y \leq 1$), Acta Mater. 104 (2016) 210-222.

[45] Mechanical Properties of half-Heusler alloys, G. Rogl et al., Acta Materialia 107, 178-195 (2016)

[46] Piezoelectric Materials for High Temperature Sensors, S. Zhang, F. Yu, J. Am. Ceram. Soc. 94, 3153-3170 (2011)

[47] Porous vycor glass: The microstructure as probed by electron microscopy, direct energy transfer, small-angle scattering, and molecular adsorption, P.

Levitz, G. Ehret, S. K. Sinha, J. M. Drake, The Journal of Chemical Physics 95, 6151 (1991)

[48] Ultra small angle neutron scattering study of the nanometer to micrometer structure of porous Vycor, M.-H. Kim, C. J. Glinka, Microporous and Mesoporous Materials 91, pp. 305–311 (2006)

[49] Product catalog, NSK linear guides miniature PU/PE series, http://www.nskamericas.com/cps/rde/xbcr/na_en/e3327c_Miniature_PU_PE.pdf

[50] Product catalog Hepco Motion, GV3 Standard Bearing, http://www.hepcomotion.com/de/ansicht-pg-21-view-477

[51] Amphenol Connex, SMA adapter (product number 132172), product website http://www.amphenolconnex.com/132172.html

[52] RS-online product catalog http://at.rs-online.com/web/p/abstandshalter-rund/2508937411/

[53] RS-online product catalog http://at.rs-online.com/web/p/keramik-heizelemente/2462517/

[54] RS-online product catalog http://at.rs-online.com/web/p/klemmblocke-ohne-sicherung/7033858/

[55] Rose+Krieger product catalog http://www.rk-rose-krieger.com/fileadmin/catalogue/lineartechnik/lt_e_d.pdf

[56] USGS 2010 Minerals Yearbook, Graphite Statistics and Information http://minerals.usgs.gov/minerals/pubs/commodity/graphite/myb1-2010-graph.pdf

[57] Product catalog from Corning Incorporated http://www.new.corning.com/lightingmaterials/images/Vycor_7930.pdf